

NORTHWESTERN UNIVERSITY

Synthesis and Characterization of Silver Vanadium Oxide Fluorides

A DISSERTATION

SUBMITTED TO THE GRADUATE SCHOOL
IN PARTIAL FULFILLMENT OF THE REQUIREMENTS

for the degree

DOCTOR OF PHILOSOPHY

Field of Chemistry

By

Thomas Allen Albrecht

EVANSTON, ILLINOIS

December 2008

© Copyright by Thomas Allen Albrecht 2008

All Rights Reserved

Abstract

Synthesis and Characterization of Silver Vanadium Oxide Fluorides

Thomas A. Albrecht

The utilization of hydrofluoric acid for the preparation of silver vanadium oxide fluorides has been advanced for the synthesis of $\text{Ag}_4\text{V}_2\text{O}_6\text{F}_2$ and $\text{Ag}_3\text{VO}_2\text{F}_4$. Silver-rich metal oxide fluorides are important battery cathode materials due to the high reduction potential of silver vs. Li, which is made even higher by the incorporation of the more electronegative fluoride. Methods were invented and developed to synthesize these phases under hydrothermal conditions and at room temperature (a first for any cathode material for primary Li batteries), to grow single crystals, and to optimize electrochemical activity.

The Ag_2O - V_2O_5 system in hydrofluoric acid was explored under low temperature ($T \leq 200\text{ }^\circ\text{C}$) and pressure ($P < 20\text{ atm}$) hydrothermal conditions. The well-known silver vanadates $\alpha\text{-Ag}_3\text{VO}_4$, $\text{Ag}_4\text{V}_2\text{O}_7$, $\beta\text{-AgVO}_3$, and $\text{Ag}_2\text{V}_4\text{O}_{11}$ were synthesized as well as the recently discovered $\text{Ag}_4\text{V}_2\text{O}_6\text{F}_2$. Owing to the high temperature solution synthesis, single crystals of $\alpha\text{-Ag}_3\text{VO}_4$ were collected and studied by X-ray diffraction to solve the crystal structure. In $\alpha\text{-Ag}_3\text{VO}_4$, silver and vanadium have a close-packed arrangement with oxide in tetrahedral positions. While vanadium is also tetrahedrally coordinated, silver adopts see-saw and square-planar orientations. In addition, a novel reaction scheme under hydrothermal conditions led to the discovery of a new silver vanadium oxide fluoride, $\text{Ag}_3\text{VO}_2\text{F}_4$. The crystal structure was determined to be cryolite-type with corner sharing Ag^+ - and V^{5+} -centered $\text{MO}_2\text{F}_4^{n-}$ octahedra and silver in the 10-coordinate A-site. $\text{Ag}_3\text{VO}_2\text{F}_4$ has a negative temperature coefficient of solubility;

therefore, growth of single crystals was achieved by slowly heating the completely dissolved reaction solution from room temperature to 100 °C.

Room temperature synthesis of silver vanadium oxide fluorides arose from hydrolysis studies in the hydrothermal system, literature-inspired solution synthesis of silver vanadates, and a desire to reduce particle size of the electrode material $\text{Ag}_4\text{V}_2\text{O}_6\text{F}_2$. Ag_2O and V_2O_5 combined in 7% (by wt.) hydrofluoric acid solution at room temperature yield $\text{Ag}_4\text{V}_2\text{O}_6\text{F}_2$ particles that are an order of magnitude smaller than manually ground particles from hydrothermal conditions. As a cathode material, the smaller particles exhibited less polarization due to the reduction of silver and therefore provide a higher potential over the course of reaction with the first four equivalents of lithium. This solution synthesis could be further adapted to yield smaller particle morphology via templating.

Professor Kenneth R. Poeppelmeier
Thesis Advisor

Acknowledgments

These past four years at Northwestern University have been quite rewarding. First, I would like to recognize and thank my advisor Professor Kenneth Poeppelmeier for his enduring support and guidance. He has allowed me to explore synthetic chemistry that truly could not have been predicted to exist when I began.

I am also indebted to many others who taught me the basics as well as the complexities of the science I researched. Dr. Erin Sorensen gave me a great electrochemistry background and helped me learn the ins and outs of life in the lab. She was a wonderful mentor during the short time we overlapped. In addition Dr. John Vaughey (Argonne National Lab) provided great insight on solid state electrochemistry and was helpful in evaluating the characteristics of a newly discovery phase. Dr. Chris Sheets provided great scientific conversations about hydrothermal chemistry and was also a great mentor, whether he knew it or not. Dr. Frédéric Sauvage also contributed greatly to my understanding of electrochemistry and the vast array of experiments available to study batteries. He inspired the creative thinking that rounded out this dissertation. And Julia Chamberlain was a great help with her closely related research. She has been a wonderful constant friend and provided inspiration and fruitful discussion that furthered both our research. And the rest of the Poeppelmeier group over the years, I thank you for providing a wonderful lab environment: Dr. Janet Kirsch, Dr. Jared Smit, Dr. Ian Saratovsky, Dr. Mariana Bertoni, Dr. Courtney Lanier, Dr. Michael Marvel, Dr. Julien Lesage, Dr. Shilie Pan, Evan Stampler, Jake Haag, Federico Rabuffetti, Jim Enterkin, Rachelle Pinlac, Cathleen Hoel, and Adam Raw.

I am also indebted to a long list of collaborators at Northwestern University (unless noted) who have added their expertise to my project through these past four years. Professor Jean-Marie Tarascon (Université de Picardie Jules Verne), Vincent Bodenez (Université de Picardie Jules Verne) and Dr. Hervé Vezin (LCOM, CNRS) helped evaluate the electrochemical discharge mechanism of $\text{Ag}_4\text{V}_2\text{O}_6\text{F}_2$ via different discharge tests, in situ X-ray diffraction and EPR. Crystallography data was collected by Dr. Charlotte Stern, and solutions were achieved with the assistance of Dr. Stern and Dr. Julien Lesage. And finally, the brief NMR study was supported by Dr. Yuyang Wu.

I would be remiss to not acknowledge those who helped me enjoy my time outside of the lab. Mariana was a great friend in introducing me to the soccer team she played on almost every weekend throughout the year. In addition, Matt Russell and Alex Haines did a wonderful job arranging impromptu summer soccer and leading a winter indoor team. Raj Vatassery and Daniel Wells were great friends to hang out with and to watch football. And Julia was always up for anything and inviting me over. I had a great time living at the Madison house with all roommates and guests who stayed over.

And then there is my family who has always encouraged and supported me to pursue whatever I wanted. It was wonderful having my brother Dan here in Chicago for two years, who found my first apartment before I got here, and made me feel like home was so close. And I'm sure the fact that he was here helped my parents feel better about having both their sons out of California. My parents, who are so loving and supportive were always there to listen to me and always excited whenever we talked. Thank you.

And finally, the last year and a half was the greatest because I became reacquainted with Jennifer, my future wife. She has always been so supportive and encouraging and I couldn't be happier than spending the rest of my life with her. While it was difficult to date long distance, the frequent trips to California or having her here were the greatest highlights for over a year. I love you.

Dedication

For Mom and Dad

Table of Contents

Abstract	3
Acknowledgments	5
Dedication	8
Table of Contents	9
List of Tables	12
List of Figures	13
Chapter 1: Introduction and Background	19
1.1 Introduction.....	20
1.2 Synthetic Technique	22
1.3 Chapter Summaries.....	24
Chapter 2: The Ag_2O–V_2O_5–$\text{HF}_{(\text{aq})}$ System and Crystal Structure of $\alpha\text{-Ag}_3\text{VO}_4$	27
2.1 Introduction.....	28
2.2 Synthesis and Characterization.....	30
2.2.1 Materials	30
2.2.2 Synthesis	30
2.2.3 Characterization	31
2.3 Results	33
2.3.1 Synthesis	33
2.3.2 Structural Description	34
2.4 Discussion.....	38
2.5 Conclusions	43
Chapter 3: In-Depth Electrochemical Characterization of $\text{Ag}_4\text{V}_2\text{O}_6\text{F}_2$	44
3.1 Introduction.....	45
3.2 Synthesis and Characterization.....	47
3.2.1 Materials	47
3.2.2 Synthesis	47
3.2.3 Characterization	48
3.3 Results	50
3.3.1 Synthesis	50
3.3.2 Electrochemical Properties	52
3.4 Discussion.....	57
3.5 Conclusions	66

Chapter 4: Ag₃VO₂F₄: Discovery and Characterization	67
4.1 Introduction	68
4.2 Synthesis and Characterization	70
4.2.1 Materials	70
4.2.2 Synthesis	71
4.2.3 Characterization	72
4.3 Results	74
4.3.1 Synthesis	74
4.3.2 Structural Description	76
4.4 Discussion	79
4.4.1 Multiple Pouch Reactions	79
4.4.2 Electrochemistry	81
4.5 Conclusions	83
Chapter 5: Reversibility of Ag₃VO₂F₄ Formation	85
5.1 Introduction	86
5.2 Synthesis and Characterization	87
5.2.1 Materials	87
5.2.2 Synthesis	87
5.3 Results	87
5.4 Discussion	89
5.4.1 Temperature and Dissociation of HF	89
5.4.2 Temperature and Waters of Hydration	92
5.5 Future Directions	99
5.6 Conclusions	101
Chapter 6: Room Temperature Synthesis of Ag₄V₂O₆F₂	103
6.1 Introduction	104
6.2 Synthesis and Characterization	107
6.2.1 Materials	107
6.2.2 Synthesis	107
6.2.3 Characterization	108
6.3 Results and Discussion	109
6.3.1 Synthesis	109
6.3.2 ⁵¹ V NMR	111
6.3.3 Electrochemistry	114
6.4 Conclusions	119
Chapter 7: Formation of SVOF from 3DOM structure	120
7.1 Introduction	121
7.2 Synthesis and Characterization	124
7.2.1 Materials	124
7.2.2 Synthesis	124
7.2.3 Characterization	125

7.3 Discussion.....	125
7.3.1 Precursor Solution.....	126
7.3.2 Template infiltration.	127
7.3.3 $\text{Ag}_3\text{VO}_2\text{F}_4$ formation within the template	128
7.3.4 Template removal	128
7.3.5 $\text{Ag}_4\text{V}_2\text{O}_6\text{F}_2$ formation.....	129
7.3.6 Characterization	130
7.4 Conclusions	131
Chapter 8: Conclusions	133
8.1 Conclusions	134
8.1.1 Exploration of Ag_2O - V_2O_5 - $\text{HF}_{(\text{aq})}$ composition space	134
8.1.2 In-depth electrochemical study of $\text{Ag}_4\text{V}_2\text{O}_6\text{F}_2$	134
8.1.3 Discovery of $\text{Ag}_3\text{VO}_2\text{F}_4$	135
8.1.4 Negative temperature coefficient of solubility of $\text{Ag}_3\text{VO}_2\text{F}_4$	135
8.1.5 Room temperature synthesis of $\text{Ag}_4\text{V}_2\text{O}_6\text{F}_2$	136
8.1.6 Formation of 3DOM $\text{Ag}_4\text{V}_2\text{O}_6\text{F}_2$	136
8.2 Future Directions	137
8.2.1 Exploration of other mixed metal oxide fluorides	137
8.2.2 Development of templated SVOF synthesis	137
References	138
Chapter 1	138
Chapter 2	138
Chapter 3	141
Chapter 4	143
Chapter 5	144
Chapter 6	146
Chapter 7	148
Electronic Appendix	150
Vita	151

List of Tables

Chapter 2: The $\text{Ag}_2\text{O}-\text{V}_2\text{O}_5-\text{HF}_{(\text{aq})}$ System and Crystal Structure of $\alpha\text{-Ag}_3\text{VO}_4$

Table 2.1 Crystallographic Data for Ag_3VO_4	32
Table 2.2 Selected Atomic Coordinates for Ag_3VO_4	32
Table 2.3 Dependency of product on the molar concentration of $\text{HF}_{(\text{aq})}$ in the hydrothermal $\text{Ag}_2\text{O}-\text{V}_2\text{O}_5-\text{HF}_{(\text{aq})}$ system.	40

Chapter 4: $\text{Ag}_3\text{VO}_2\text{F}_4$: Discovery and Characterization

Table 4.1 Crystallographic Data for $\text{Ag}_3\text{VO}_2\text{F}_4$	74
Table 4.2 Selected Atomic Coordinates for $\text{Ag}_3\text{VO}_2\text{F}_4$	74

Chapter 6: Room Temperature Synthesis of $\text{Ag}_4\text{V}_2\text{O}_6\text{F}_2$

Table 6.1 Summary of experimental and literature values for ^{51}V NMR of V_2O_5 dissolved in $\text{HF}_{(\text{aq})}$	113
--	-----

List of Figures

Chapter 1: Introduction and Background

- Figure 1.1** Schematic showing the ICD battery circuit where parallel capacitors are charged and then discharged as a high energy shock to the heart. 21
- Figure 1.2** Schematic of the Teflon bag hydrothermal synthetic technique..... 23

Chapter 2: The $\text{Ag}_2\text{O}-\text{V}_2\text{O}_5-\text{HF}_{(\text{aq})}$ System and Crystal Structure of $\alpha\text{-Ag}_3\text{VO}_4$

- Figure 2.1** Thermal ellipsoid plot (showing 50% probability) of $\alpha\text{-Ag}_3\text{VO}_4$. Vanadium is tetrahedrally coordinated to four tetrahedrally-coordinated oxygen anions..... 33
- Figure 2.2** Primitive cells in $\alpha\text{-Ag}_3\text{VO}_4$ have a distorted “anti” sphalerite-type structure of face-centered Ag and V cations with O^{2-} anions in either T_+ or T_- holes. Blue = Ag, Orange = V, Red = O..... 35
- Figure 2.3** Perspective drawing of Ag_3VO_4 . The off-center purple atoms are the see-saw coordinated Ag1 and the central green atoms are Ag2 in the nearly square planer coordination. Blue = Ag, Orange = V, Red = O. 36
- Figure 2.4** Perspective drawing of Ag_3VO_4 . In the center are the see-saw Ag1. Blue = Ag, Orange = V, Red = O..... 37
- Figure 2.5** Coordination environment of silver atoms in $\alpha\text{-Ag}_3\text{VO}_4$. (a) Pseudo see-saw with bond angles of $\text{O1-Ag1-O1}' = 98.13(9)^\circ$, $\text{O1-Ag1-O2}' = 100.73(14)^\circ$, $\text{O1-Ag1-O2} = 176.47(15)^\circ$, $\text{O1}'\text{-Ag1-O2}' = 91.11(13)^\circ$, $\text{O1}'\text{-Ag1-O2} = 84.40(13)^\circ$, and $\text{O2}'\text{-Ag1-O2} = 81.54(14)^\circ$ and bond lengths $\text{Ag1-O1} = 2.164(4) \text{ \AA}$, $\text{Ag1-O1}' = 2.444(4) \text{ \AA}$, $\text{Ag1-O2} = 2.505(4) \text{ \AA}$, and $\text{Ag1-O2}' = 2.196(4) \text{ \AA}$. (b) Distorted square planer with linear $\text{O1-Ag2-O1}'$ and $\text{O2-Ag2-O2}'$ bond angles and $\text{O1-Ag2-O2} = 97.57(14)^\circ$ and bond lengths $\text{Ag2-O1/O1}' = 2.364(4) \text{ \AA}$ and $\text{Ag2-O2/O2}' = 2.374(4) \text{ \AA}$ 37
- Figure 2.6** A close packed layer in $\alpha\text{-Ag}_3\text{VO}_4$. Blue = Ag, Orange stripes = V..... 38

Figure 2.7	Composition space for the hydrothermal system of Ag_2O – V_2O_5 – $\text{HF}_{(\text{aq})}$. Formation regions for the silver vanadates and the silver vanadium oxide fluoride are outlined. Line A represents a constant $\text{HF}_{(\text{aq})}$ quantity while varying $\text{Ag}_2\text{O}:\text{V}_2\text{O}_5$ ratio, increasing toward a higher silver fraction. Line B represents a constant 4:1 $\text{Ag}_2\text{O}:\text{V}_2\text{O}_5$ ratio, increasing toward a higher $\text{HF}_{(\text{aq})}$ fraction.	39
Figure 2.8	SEM of (a) $\text{Ag}_2\text{V}_4\text{O}_{11}$ and (b) $\text{Ag}_4\text{V}_2\text{O}_6\text{F}_2$ particles from hydrothermal synthesis.....	42

Chapter 3: In-Depth Electrochemical Characterization of $\text{Ag}_4\text{V}_2\text{O}_6\text{F}_2$

Figure 3.1	Full-pattern matching refinement of the powder X-ray diffraction pattern of ground $\text{Ag}_4\text{V}_2\text{O}_6\text{F}_2$ (SVOF). Inset: Scanning electron microscopy picture of the composite SVOF/ C_{sp} electrode.....	50
Figure 3.2	Structural representation of SVOF in the (<i>bc</i>) and (<i>ac</i>) planes with the V^{5+} -centered polyhedron.....	51
Figure 3.3	1 st cycle galvanostatic curve recorded at C/10 rate of a composite SVOF/ C_{sp} electrode in 1M LiPF_6 EC/DMC 1:1 electrolyte (a) down to 0.01V cut-off potential (b) after two and four lithium inserted.....	53
Figure 3.4	(a) Comparison of a galvanostatic-driven discharge performed at D/50 between SVOF and SVO synthesized by a similar solvothermal route. (b) Evolution of the electrode capacity as a function of the discharge rate beyond 3 V and 2.5 V for SVOF and SVO. (c) Influence of the discharge rate on the electrochemical discharge curve of SVOF (D/50, D/10 and D).	55
Figure 3.5a	G.I.T.T. curve of SVOF/ C_{sp} composite electrode in 1M LiPF_6 EC/DMC 1:1 electrolyte by applying a D/10 discharge rate for 2 hours followed by 15 hours relaxation time.....	56
Figure 3.5b	G.I.T.T. curve of SVOF/ C_{sp} composite electrode in 1M LiPF_6 EC/DMC 1:1 electrolyte by applying a D/10 discharge rate for 2 hours followed by 15 hours relaxation time. A total of 3.7 Li (148 mAh/g) is inserted above a potential of 3 V.	57

Figure 3.6	<i>In situ</i> evolution of the XRD pattern recorded every 0.09 Li ⁺ inserted at a D/10 discharge rate between Li ₀ Ag ₄ V ₂ O ₆ F ₂ and Li ₁ Ag ₄ V ₂ O ₆ F ₂ in a 2θ range of (a) 15-50° (b) 26-31°.....	58
Figure 3.7	(a) <i>In situ</i> evolution of the XRD pattern recorded every 1 Li ⁺ inserted at a D/10 discharge rate between Li ₀ Ag ₄ V ₂ O ₆ F ₂ and Li ₇ Ag ₄ V ₂ O ₆ F ₂ in a 2θ range of 15-50° (b) Comparison of the XRD patterns for SVOF, Li ₇ Ag ₄ V ₂ O ₆ F ₂ and Li ₁₇ Ag ₄ V ₂ O ₆ F ₂	60
Figure 3.8	Evolution of the silver metal and SVOF XRD peak area as a function of x in Li _x Ag ₄ V ₂ O ₆ F ₂	61
Figure 3.9	CW EPR spectra for Li _x Ag ₄ V ₂ O ₆ F ₂ for x=0, 1, 2, 3, 3.5 and 6. The spectra were recorded at room temperature.	62
Figure 3.10	Three-pulse ESEEM spectra recorded at 4K for Li ₁ Ag ₄ V ₂ O ₆ F ₂ and Li _{3.5} Ag ₄ V ₂ O ₆ F ₂	63
Figure 3.11	Plot of EPR intensity signal * temperature product (IT) versus temperature for Li ₆ Ag ₄ V ₂ O ₆ F ₂ compound. The data was fitted according to the Bleaney-Bowers equation.....	64
Figure 3.12	High Resolution Transmission Electron Microscopy bright field image obtained on an electrochemically discharged SVOF showing (a) the particle exfoliation with silver dendrites (b) the silver nanoparticles embedded in the amorphous Li _x SVOF matrix.	65

Chapter 4: Ag₃VO₂F₄: Discovery and Characterization

Figure 4.1	Powder X-ray diffraction patterns showing the decomposition of Ag ₃ VO ₂ F ₄ into Ag ₃ VO ₄ and Ag ₄ V ₂ O ₆ F ₂ over 52 hours (from the sample labeled “boil fresh”). Also shown is the increased purity and stability of Ag ₃ VO ₂ F ₄ from a reaction at 100 °C for 24 hours.	76
Figure 4.2	Cryolite unit cell of Ag ₃ VO ₂ F ₄ , similar to a perovskite structure, consisting of infinite corner sharing octahedra. Smaller, orange octahedra are vanadium-centered [VO _{2/2} F _{4/2}] ⁺ , and larger blue octahedra are silver-centered [AgO _{2/2} F _{4/2}] ³⁻ . Silver also resides in the A-site (dark blue) and is 10 coordinate. Red circles represent disordered oxide/fluoride anions.	78

Figure 4.3	Examples of distortions of d^0 transition metals in an octahedral environment surrounded by oxide and fluoride ligands. Shorter, stronger metal-oxide bonds form and thus the central cation can distort toward a corner, edge, or face.	78
Figure 4.4	Depiction of the $\text{cis-VO}_2\text{F}_4^{3-}$ anion solved with a split-occupancy vanadium (orange) center. One vanadium position and the representative bonds are lighter in color to help differentiate between the two sets. V-O bonds are in red; V-F bonds are in green. The two defined fluoride positions are green, and the mixed oxide / fluoride positions are mixed red / green.	79
Figure 4.5	Plot of products recovered from reactions under hydrothermal conditions. Some reactions lead to phase pure product of $\text{Ag}_3\text{VO}_2\text{F}_4$, $\text{Ag}_4\text{V}_2\text{O}_6\text{F}_2$, or $\text{Ag}_4\text{V}_2\text{O}_7$ and others lead to a mixed product. Arrows next to the percentages point to the pure phase that belongs to that percent value.	80
Figure 4.6	Reaction setup showing the triple pouch. Dimensions of the outermost pouch were identical to those for “typical” single-pouch reactions (1.75 in. x 3 in.) and the inner two pouches were cut to fit snugly in their respective outer pouch. The horizontal and vertical lines along the edges represent the heat-sealed seal.	80
Figure 4.7	Voltage vs. capacity for $\text{Ag}_3\text{VO}_2\text{F}_4$ discharged in 5 mV steps followed by a relaxation time of 6 hours.	83
Figure 4.8	Voltage vs. capacity for $\text{Ag}_4\text{V}_2\text{O}_6\text{F}_2$ discharged in 5 mV steps followed by a relaxation time of 6 hours.	83

Chapter 5: Reversibility of $\text{Ag}_3\text{VO}_2\text{F}_4$ Formation

Figure 5.1	Solubility curves for NaCl and KCl in H_2O . Following the dashed line from the H_2O vertex would first precipitate NaCl and eventually coprecipitate NaCl and KCl.	93
Figure 5.2	Solubility curves for (a) Na_2SO_4 and NaCl in H_2O and (b) CaCl_2 and MgCl_2 in H_2O which show their respective hydrated precipitates of $\text{Na}_2\text{SO}_4 \cdot 10\text{H}_2\text{O}$, $\text{CaCl}_2 \cdot 6\text{H}_2\text{O}$, and $\text{MgCl}_2 \cdot 6\text{H}_2\text{O}$	94

Figure 5.3	Solubility curves for (a) NH_4NO_3 and AgNO_3 in H_2O , where the double salt $\text{NH}_4\cdot\text{AgNO}_3$ forms and (b) $\text{Al}_2(\text{SO}_4)_3$ and FeSO_4 in H_2O where $\text{Ag}_2(\text{SO}_4)_3\cdot\text{FeSO}_4\cdot 24\text{H}_2\text{O}$ can be recovered, along with the respective single salt hydrates.	94
Figure 5.4	Solubility curves for MgSO_4 and Na_2SO_4 in H_2O and their respective hydrates $\text{MgSO}_4\cdot 7\text{H}_2\text{O}$ and $\text{Na}_2\text{SO}_4\cdot 10\text{H}_2\text{O}$ at (a) low temperature and (b) high temperature showing the appearance of the double salt $\text{Na}_2\text{Mg}(\text{SO}_4)_2\cdot 4\text{H}_2\text{O}$, also represented by <i>D</i>	96
Figure 5.5	Solubility and precipitate diagram for AgF - HF - H_2O and V_2O_5 - HF - H_2O systems that show the precipitates recovered from saturated solutions. Notable are the vast number of phases with water and hydrofluoride of crystallization.	97
Figure 5.6	Theoretical solubility curves for AgF and VO_2F in $\text{H}_2\text{O}/\text{HF}$ and their respective hydrates $\text{AgF}\cdot 2\text{HF}$ and $3\text{VO}_3\cdot\text{HF}\cdot\text{H}_2\text{O}$ at high temperature. The magnitude and width of the curves were arbitrarily drawn, though placement of each salt is accurate.	99
Figure 5.7	Precipitation of metal oxides / oxide fluorides / fluorides from a variety of hydrofluoric acid solution concentrations. Dotted lines were drawn to separate elements by period.	100
Figure 5.8	Powder X-ray diffractogram of $\text{Ag}_3\text{VO}_2\text{F}_4$ and $\text{Ag}_3\text{MoO}_3\text{F}_3$ showing the peak shift to smaller angles for the larger lattice parameters of $\text{Ag}_3\text{MoO}_3\text{F}_3$ owing to different V^{5+} and Mo^{6+} radii.	101

Chapter 6: Room Temperature Synthesis of $\text{Ag}_4\text{V}_2\text{O}_6\text{F}_2$

Figure 6.1	Scanning Electron Microscopy micrographs of particles used as cathode in lithium batteries (a) $\text{Ag}_4\text{V}_2\text{O}_6\text{F}_2$ synthesized by hydrothermal method (SVOF-Hyd), (b) $\text{Ag}_4\text{V}_2\text{O}_6\text{F}_2$ precipitated at room temperature (SVOF-RT) and (c) $\text{Ag}_2\text{V}_4\text{O}_{11}$ synthesized under hydrothermal conditions (ϵ -SVO).	107
Figure 6.2	Full-pattern matching refinement of the powder X-ray diffraction pattern of ground $\text{Ag}_4\text{V}_2\text{O}_6\text{F}_2$ (SVOF). Scanning Electron Microscopy pictures of SVOF as prepared at room temperature in inset.	109

- Figure 6.3** A series of powder X-ray diffractograms from reactions with a decreasing $\text{HF}_{(\text{aq})}$ concentration (from the bottom up). $\text{Ag}_3\text{VO}_2\text{F}_4$ is formed with concentrated $\text{HF}_{(\text{aq})}$, and phase pure $\text{Ag}_4\text{V}_2\text{O}_6\text{F}_2$ at 7% $\text{HF}_{(\text{aq})}$ concentration. Diffractogram from a hydrothermal reaction, which yielded $\text{Ag}_4\text{V}_2\text{O}_6\text{F}_2$, is shown at the top for comparison. Two dotted lines highlight the disappearance of $\text{Ag}_3\text{VO}_2\text{F}_4$ peaks..... 111
- Figure 6.4** ^{51}V NMR of V_2O_5 dissolved in a) 48% and b) 7% hydrofluoric acid. 113
- Figure 6.5** Potential vs. gravimetric capacity curves comparing the discharge of $\text{Ag}_4\text{V}_2\text{O}_6\text{F}_2$ material tailored at room temperature (SVOF-RT) and hydrothermal conditions (SVOF-Hyd) and $\text{Ag}_2\text{V}_4\text{O}_{11}$ (SVO) from hydrothermal conditions discharged using (a) Galvanostatic Intermittent Titration Technique (GITT), (b) cathode polarization comparison determined from GITT experiments on SVOF-Hyd and SVOF-RT (c) a discharge rate of D/50, and (d) a discharge rate of 2D..... 116
- Figure 6.6** Plot comparing energy density vs. power density of cathodes consisting of $\text{Ag}_4\text{V}_2\text{O}_6\text{F}_2$ synthesized at room temperature (SVOF-RT) and at hydrothermal conditions (SVOF-Hyd) and $\text{Ag}_2\text{V}_4\text{O}_{11}$ at hydrothermal reactions, for potentials above 3 and 2.5 V..... 117
- Figure 6.7** TEM micrographs of lithiated $\text{Ag}_4\text{V}_2\text{O}_6\text{F}_2$ showing regions of $\text{Li}_5\text{Ag}_{0.1}\text{V}_4\text{O}_x\text{F}_y$ (light) and Ag metal (dark). Silver metal is on the order of 10 nm in diameter along the particle edges. 118

Chapter 7: Formation of SVOF from 3DOM structure

- Figure 7.1** Schematic diagram of the synthesis of a material from a 3DOM template. 123
- Figure 7.2** TEM micrographs of as recovered product from $\text{Ag}_3\text{VO}_2\text{F}_4$ formed in 3DOM template washed with water. 131

Chapter One

Introduction and Background

1.1 Introduction

High capacity and high rate primary lithium batteries are essential for the functionality and future invention of advanced devices. In an energy-driven world, the ability to store energy chemically and release it electrically is crucial for highly portable devices for use in difficult-to-access regions as remote as a battlefield or as close as a medical device implanted in the body. While secondary, or rechargeable, Li-ion batteries are very common in every-day use, the single use battery has its niche in a specialized field where it must have a long life time and be able to run power-hungry electronics in short bursts. For example, small sensor units commonly referred to as smart dust could be dropped from an airplane to study air pollution and toxins, or released from a satellite probe to study another planet's atmosphere. Each microelectromechanical sensor would not only need enough energy record its surroundings but also would need power to wirelessly transmit its findings. Implantable medical devices also use primary lithium batteries. Some applications require constant low power stimuli, but others such as cardiac defibrillation need high power in rapid bursts. In order to accomplish such tasks, a battery with a high energy density is necessary so as to minimize the volume of the battery pack, and thus the device, within the patient, while maximizing the lifetime of the battery (as the battery/device could only be replaced by the patient undergoing surgery). In addition, the battery needs to operate at a high potential to deliver the therapy most rapidly in times of tachycardia.

The cathode material of choice for implantable cardioverter defibrillators (ICDs) has been the silver vanadium oxide $\text{Ag}_2\text{V}_4\text{O}_{11}$ (SVO) since it was first suggested for this application in 1984 by Keister et al.¹ In SVO, the initial voltage plateau at 3.25 V corresponds to silver reduction. A secondary plateau, corresponding to vanadium reduction, occurs at roughly 2.5 V. While SVO has a high capacity (315 mAh/g), 71% of the capacity is a result of $\text{V}^{5+}/\text{V}^{4+}$

reduction. Further reduction of V^{4+} to V^{3+} occurs at voltages too low for use in an ICD.²⁻⁵ A silver vanadate with a greater Ag:V molar ratio would increase the high voltage component of the electrode; however, the silver vanadates with a Ag:V ratio greater than 1:2 tend to have very poor kinetics, low usable capacity or low conductivity.⁶ As the Li-SVO system was developed, it was shown to have a high capacity of 315 mAh/g, of which 100mAh/g is above 3 V, where ICDs work most efficiently (Figure 1.1).⁷ However, a long-term goal of the medical battery industry is to increase the capacity of the cathode above 3 V while maintaining high electrode stability. In order to achieve this, alternative compounds are constantly under evaluation. In 2004, the first silver vanadium oxide fluoride $Ag_4V_2O_6F_2$ (SVOF) was discovered and shown to have significant electrochemical activity.^{8,9} Owing to the high mole fraction of silver, SVOF has a greater capacity above 3 V of 148 mAh/g, in comparison to 100 mAh/g in SVO. In addition to the increased capacity, the silver reduction potential of SVOF is 3.52 V, 300 mV higher than that of SVO, which is due to fluoride incorporation. It was here that the current research was begun.

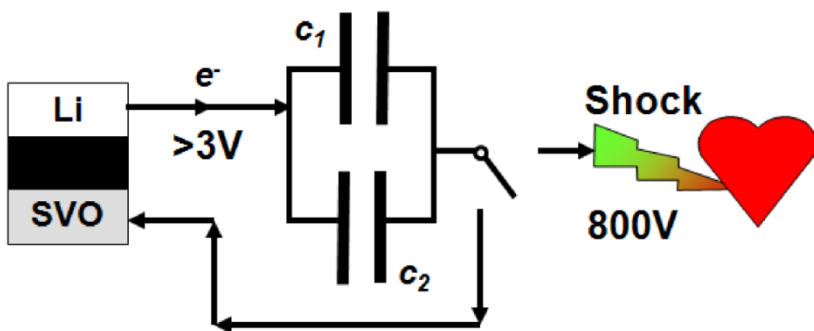


Figure 1.1 Schematic showing the ICD battery circuit where parallel capacitors are charged and then discharged as a high energy shock to the heart.

From the initial discovery of the first silver vanadium oxide fluoride it was apparent that others might also form under the right conditions. Mixed metal oxide fluoride phases are

extremely common for compounds of AMO_xF_y where A can be an alkali metal or alkaline earth metal and M can be any of a number of transition metals. However, the goal of the project presented in this thesis was to investigate the system where $\text{A} = \text{Ag}^+$ and $\text{M} = \text{V}^{5+}$ to discover a new silver vanadium oxide fluoride phase for potential use as a cathode material. Through careful observation, scientific discussions with peers, and serendipity, not only was a new phase discovered and characterized, new synthetic techniques at room temperature were utilized that improved the properties of $\text{Ag}_4\text{V}_2\text{O}_6\text{F}_2$. And finally, the project culminated in a combination of these two concepts into the beginnings of template formation of SVOF within a three-dimensionally ordered macroporous material.

1.2 Synthetic Technique

Mild hydrothermal techniques are an effective, low temperature approach to the synthesis of transition metal oxide fluoride materials. The combination of low temperatures (typically under 200 °C) and autogenous pressures can be favorable for single crystal growth that is suitable for single crystal X-ray diffraction. All of the reactants for the synthesis, which consist of metal oxides, H_2O , and aqueous hydrofluoric acid (HF) are added to a Teflon fluoro(ethylene-propylene) (FEP) pouch.¹⁰ The metal oxides will dissolve in the aqueous HF, which behaves as both a mineralizer and a fluoride source.

The bags are made by folding a 3.5 by 3.0 inch piece of FEP film in half along its shorter axis and sealing it on two sides with a thermal impulse sealer. After the reactants are added, the third side of the pouch is sealed and placed in either a 250 mL polytetrafluoroethylene Teflon-lined Parr autoclave. The pressure vessel is typically backfilled 33% with deionized water, heated for 24 h at 150 °C, and then cooled to room temperature over an additional 24 h.

The bags are opened in air and the products are recovered by vacuum filtration into a polyethylene side-arm filter flask. The “Teflon bag” approach offers a number of synthetic advantages, which include a pseudo-combinatorial method for a number of different reactions to be run under identical reaction conditions, as well as providing an inexpensive reaction vessel that can withstand the harsh chemical environment under which the oxide fluoride products are synthesized. A schematic of the synthetic process is shown in Figure 1.2.

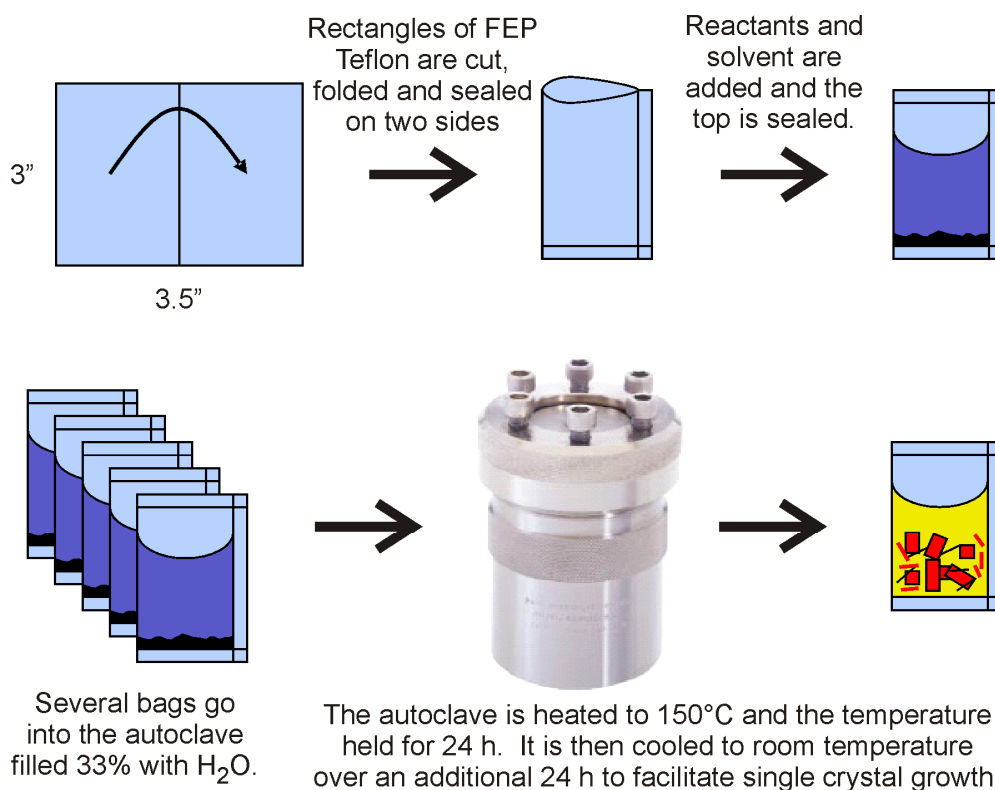


Figure 1.2 Schematic of the Teflon bag hydrothermal synthetic technique.

The FEP pouches were also utilized as reaction vessels at room temperature and at 100 °C. It is known that water from the backfill in the autoclave will diffuse inward at the elevated hydrothermal temperatures and thus play a role in the reaction. One way to avoid this is to perform reactions at lower temperatures, which led to one of the discoveries and the utilization of

the high reactivity between Ag_2O and V_2O_5 in hydrofluoric acid. The method most commonly used for this was placing a sealed reaction pouch in a water bath brought to a boil. Differences were observed for conditions where either the pouch was placed in the bath at room temperature and then slowly brought to a boil or the pouch was placed in the bath already boiling. Alterations to this method could include using a mineral oil bath instead of water to achieve still higher temperatures while still excluding the water diffusion observed from hydrothermal conditions.

1.3 Chapter Summaries

The foundation of this work was the discovery of the first silver vanadium oxide fluoride, $\text{Ag}_4\text{V}_2\text{O}_6\text{F}_2$, which was shown to be a superior cathode for Li batteries.^{8,9} As this was the first phase of its kind, it was necessary to explore the Ag_2O - V_2O_5 - $\text{HF}_{(\text{aq})}$ composition space to find additional silver vanadium oxide fluorides. In **Chapter 2**, reactions were studied under hydrothermal conditions similar to those that first produced SVOF. It was found that metal oxide starting ratio, $\text{HF}_{(\text{aq})}$ amount, and temperature played a role the formation of $\text{Ag}_2\text{V}_4\text{O}_{11}$, $\beta\text{-AgVO}_3$, $\text{Ag}_4\text{V}_2\text{O}_7$, $\text{Ag}_4\text{V}_2\text{O}_6\text{F}_2$, or $\alpha\text{-Ag}_3\text{VO}_4$. The crystal structure of the latter phase had not been solved until here.

Owing to the vastly increased discharge potential above 3 V that $\text{Ag}_4\text{V}_2\text{O}_6\text{F}_2$ exhibited against $\text{Ag}_2\text{V}_4\text{O}_{11}$, a more in depth investigation of its reactivity with lithium in a battery was desired. **Chapter 3** examines the lithium insertion mechanism into SVOF by means of in situ X-ray diffraction, EPR, and TEM to explain the characteristics observed in the discharge curve. It was determined that the first 3.8 Li equivalents are used to reduce Ag^+ to Ag^0 and gave rise to an increasingly polarized cathode. The silver metal morphology consisted of dendrites as well as

nanoparticles observed along the particle edge. This polarization, however, subsided rapidly while half the vanadium was reduced from V^{5+} to V^{3+} , as followed by EPR.

Noticeably absent from the composition space first investigated was the presence of another oxide fluoride phase, which led to a deeper investigation as to what controlled the formation of $Ag_4V_2O_6F_2$ vs. $Ag_4V_2O_7$. In **Chapter 4**, it was realized that another silver vanadium oxide fluoride could be recovered if hydrolysis was prevented. While $Ag_4V_2O_6F_2$ hydrolyzes to $Ag_4V_2O_7$ at higher temperatures (150 °C vs. 200 °C) with an increased presence of H_2O in the system, reactions that utilized decreased water content led to the formation of $Ag_3VO_2F_4$. Its crystal structure was solved and it was also evaluated as a cathode in a Li battery. Unfortunately, it was not stable in the battery because it ion exchanged with the electrolyte.

Attempts to grow crystals of $Ag_3VO_2F_4$ were not fruitful until it was discovered that the material had a negative temperature coefficient of solubility. In **Chapter 5**, the reaction system where this phenomenon was first observed is described, and the driving factors for it to occur are discussed. At low temperatures, a nearly saturated solution of Ag_2O and V_2O_5 dissolved in $HF_{(aq)}$ would precipitate the desired product upon heating (and grow crystals upon slow heating) which would then dissolve upon cooling. The first hypothesis for what happens is that the temperature changes the acidity of the solution toward more dissociated HF at lower temperatures. The increased $[H^+]$ could favor the formation of certain soluble species, thus dissolving $Ag_3VO_2F_4$. Another possibly simultaneous argument addresses the entropy and enthalpy of releasing water and/or hydrogenfluoride of crystallization from two single salts to form the anhydrous double salt $Ag_3VO_2F_4$.

The formation of $\text{Ag}_3\text{VO}_2\text{F}_4$ at both high temperatures (150 °C) and room temperature alongside the formation of $\text{Ag}_4\text{V}_2\text{O}_6\text{F}_2$ at the same high temperatures left one piece of the puzzle empty: formation of the latter phase at room temperature. **Chapter 6** describes the first room temperature synthesis of a cathode material for a primary Li battery. While in Chapter 4 the goal for the formation of the new phase was to limit hydrolysis under hydrothermal conditions, the reverse was the goal at room temperature. With the addition of water to reactions that form $\text{Ag}_3\text{VO}_2\text{F}_4$, $\text{Ag}_4\text{V}_2\text{O}_6\text{F}_2$ would form. Room temperature SVOF was electrochemically compared to hydrothermally-made SVOF (SVOF-Hyd) and SVO. It exhibited less polarization than SVOF-Hyd and maintained the high capacity.

Finally, the concepts and procedures discussed in chapters 4, 5 and 6 were combined to begin the process of synthesizing SVOF within a three-dimensionally ordered macroporous material. **Chapter 7** discusses the obstacles to overcome with regards to infiltrating voids with a precursor solution and controlled phase formation by precipitation would occur followed by a conversion of $\text{Ag}_3\text{VO}_2\text{F}_4$ to the desired $\text{Ag}_4\text{V}_2\text{O}_6\text{F}_2$. Particles formed had dimensions of around 100 nm and appeared amorphous by electron diffraction. Future directions that may be pursued as a result of the work are also described.

Chapter Two

The $\text{Ag}_2\text{O}-\text{V}_2\text{O}_5-\text{HF}_{(\text{aq})}$ System and Crystal Structure of $\alpha\text{-Ag}_3\text{VO}_4$

2.1 Introduction

Mixed metal oxide fluoride species can be generated in direct hydrothermal reactions of early and late transition metal oxide precursors in the presence of hydrogen fluoride (e.g. $(\text{HF})_x \cdot \text{pyridine}$ or $\text{HF}_{(\text{aq})}$).^{1,2} Whereas numerous inorganic-organic hybrid materials have been made, the use of $\text{HF}_{(\text{aq})}$ has led to purely inorganic oxide fluorides, e.g. $\text{Ag}_6\text{Mo}_2\text{O}_7\text{F}_3\text{Cl}$ and $\text{Ag}_4\text{V}_2\text{O}_6\text{F}_2$.³⁻⁵ In these reactions, aqueous HF acts as a mineralizer and provides a source of fluoride, which may be incorporated into the product.

Owing to their application as primary battery materials, the silver vanadium oxides have been studied intensely.⁶⁻⁸ While various silver vanadates are known, $\text{Ag}_4\text{V}_2\text{O}_6\text{F}_2$ represents the first phase reported in the $\text{Ag}_2\text{O}-\text{V}_2\text{O}_5-\text{HF}_{(\text{aq})}$ system. This work focuses on the $\text{Ag}_2\text{O}-\text{V}_2\text{O}_5-\text{HF}_{(\text{aq})}$ system to search for additional silver vanadium oxide fluoride phases and to elucidate the relationships between the other majority all oxide phases formed. During this investigation, the well known silver vanadium oxides $\text{Ag}_2\text{V}_4\text{O}_{11}$, $\beta\text{-AgVO}_3$, $\text{Ag}_4\text{V}_2\text{O}_7$, and $\alpha\text{-Ag}_3\text{VO}_4$ were generated in addition to the aforementioned $\text{Ag}_4\text{V}_2\text{O}_6\text{F}_2$, of which only $\text{Ag}_2\text{V}_4\text{O}_{11}$ and $\beta\text{-AgVO}_3$ previously had been made hydrothermally.^{9,10} The versatility of aqueous hydrofluoric acid to form a wide variety of silver vanadium oxides is noteworthy and appreciable compared to other techniques.

In the 1930s, Britton and Robinson more thoroughly investigated solutions of silver and vanadium salts first studied in the late 1800's.¹¹ Of interest were the ionic species remaining in the solutions upon precipitation of AgVO_3 , $\text{Ag}_4\text{V}_2\text{O}_7$, and Ag_3VO_4 . For example, in solutions targeting a Ag_3VO_4 precipitate, the ions present were not Ag^+ and VO_4^{3-} , but rather Ag^+ , HVO_4^{2-} , and OH^- . Konta *et al.* also studied solution chemistry of silver vanadium oxides by varying the pH between 7 and 14 and the temperature between 273 K and 298 K and various oxides such as

α -AgVO₃, β -AgVO₃, Ag₄V₂O₇, and Ag₃VO₄ were synthesized from aqueous solutions of AgNO₃ and either NH₄VO₃ or Na₃VO₄.¹² Moreover, solid state reactions between Ag₂O and V₂O₅ have been used to form the aforementioned silver vanadates, and two others, AgV₇O₁₈ and Ag₂V₄O₁₁.¹³ Included in these reports were the transition temperatures between α -, β -, and γ -AgVO₃ phases. Since then, crystal structures for Ag₂V₄O₁₁, α - and β -AgVO₃, and Ag₄V₂O₇ have been solved and phases such as δ -AgVO₃ and β -Ag₃VO₄, and nonstoichiometric compounds such as Ag_xV₂O₅ and Ag_{1+x}V₃O₈, have been observed.¹⁴⁻¹⁸ An independent study on the structures of α -, β - and γ -Ag₃VO₄ from refinement of powder X-ray diffraction patterns was performed simultaneously.¹⁹

Recently, other processes have been reported to synthesize silver vanadium oxides. For example, sol-gel techniques have been used for the synthesis of Ag₂V₄O₁₁. The process involves a V₂O₅·*n*H₂O gel combined with a silver-containing salt, which is then heated at up to 450 °C for up to 24 hr. Another method investigated by Kittaka *et al.* utilized mechanical ball milling of different ratios of Ag₂O and V₂O₅, to produce amorphous α -AgVO₃, crystalline Ag₄V₂O₇, or Ag₃VO₄ with additional phases.²⁰

Very few reports exist in the literature discussing the synthesis of silver vanadium oxides using hydrothermal techniques. Liu *et al.* produced small microcrystals 18 to 400 nm wide and lengths of up to tens of micrometers (nanowires) of β -AgVO₃ from solutions of NH₄VO₃ and either Ag₂CO₃ or AgC₂H₃O₂ heated under hydrothermal conditions.¹⁰ Additional phases were also recovered, such as α -AgVO₃, upon variation of temperature, pH, and reagents. Takeuchi *et al.* proposed the use of hydrothermal methods in the synthesis of the cathode material Ag₂V₄O₁₁ (SVO).²¹ The desired small particle size (<1 μ m in diameter) has potential to improve the

modern high-rate SVO batteries by providing higher current pulses more rapidly. Experimental details remain to be specified. However, Mao *et al.* synthesized 10 to 30 nm thick, 70-200 nm wide, and 2 to 5 mm long crystallites (nanobelts) of $\text{Ag}_2\text{V}_4\text{O}_{11}$ from an aqueous solution of V_2O_5 , AgNO_3 , and 1,6-hexanediamine heated under hydrothermal conditions at 180°C for 2 days.⁹

2.2 Synthesis and Characterization

2.2.1 Materials

Caution. Hydrofluoric acid is toxic and corrosive and must be handled with extreme caution and the appropriate protective gear! If contact with the liquid or vapor occurs, proper treatment procedures should be followed immediately.²²⁻²⁴

Materials. Ag_2O (99.5%, DFG), V_2O_5 (99.6%, Alfa-Aesar), and aqueous hydrofluoric acid (48-50% HF by weight, Fisher) were used as received.

2.2.2 Synthesis

Crystals of $\alpha\text{-Ag}_3\text{VO}_4$ were prepared from a reaction of 0.5675 g (2.449×10^{-3} mol) of Ag_2O , 0.0557 g (3.06×10^{-4} mol) of V_2O_5 , and 0.2522 g (of $\text{HF}_{(\text{aq})}$ 6.179×10^{-3} mol HF) in a heat sealed Teflon [fluoro(ethylene-propylene)] pouch.²⁵ The pouch was placed in a 125 mL, poly(tetrafluoroethylene) (PTFE) Teflon lined Parr autoclave, backfilled with 42 mL of deionized H_2O . Up to seven pouches of varied compositions were simultaneously placed in the autoclave to complete a greater quantity of reactions while using one pressure vessel. The autoclave was heated at 150°C for 24 hr. and cooled at a rate of $6^\circ\text{C} / \text{hr}$. The pouch was opened in air and the contents were vacuum filtered to retrieve bright red crystals of $\alpha\text{-Ag}_3\text{VO}_4$ in 78% yield based on V_2O_5 . Identical reaction conditions, other than reagent ratios, were used

to make $\text{Ag}_2\text{V}_4\text{O}_{11}$, $\beta\text{-AgVO}_3$, and $\text{Ag}_4\text{V}_2\text{O}_6\text{F}_2$. Products were analyzed by powder X-ray diffraction.

$\text{Ag}_2\text{V}_4\text{O}_{11}$ was made using 0.2678 g (1.155×10^{-3} mol) of Ag_2O , 0.4198 g (2.308×10^{-3} mol) of V_2O_5 , and 0.2328 g of $\text{HF}_{(\text{aq})}$ (5.703×10^{-3} mol HF). The product was recovered in 98% yield based on V_2O_5 with a trace of $\beta\text{-AgVO}_3$.

$\beta\text{-AgVO}_3$ was made from 0.2979 g (1.285×10^{-3} mol) of Ag_2O , 0.1559 g (8.571×10^{-4} mol) of V_2O_5 , and 0.2572 g of $\text{HF}_{(\text{aq})}$ (6.301×10^{-3} mol HF) with 80% recovery based on V_2O_5 .

$\text{Ag}_4\text{V}_2\text{O}_6\text{F}_2$ was made as previously reported.⁵

$\text{Ag}_4\text{V}_2\text{O}_7$ was made using 0.3970 g (1.713×10^{-3} mol) of Ag_2O , 0.0777 g (4.272×10^{-4} mol) of V_2O_5 , and 0.2561 g of $\text{HF}_{(\text{aq})}$ (6.274×10^{-3} mol HF). However, the system was heated for 24 hr. at 200 °C instead of 150 °C. The product was recovered in 100% yield based on V_2O_5 .

2.2.3 Characterization

Crystallographic Determination. Single-crystal X-ray diffraction data were collected on a Bruker SMART-1000 diffractometer equipped with Mo $K\alpha$ radiation ($\lambda = 0.71073 \text{ \AA}$). Reflections were integrated with the SAINT-Plus program.²⁶ The structure was solved in space group of $C2/c$ by direct methods and refined against F^2 using full-matrix least-squares techniques.²⁷ The $\alpha\text{-Ag}_3\text{VO}_4$ crystal was twinned and absorption correction on one twinned data set was applied using Twinabs, a part of the SAINT integration program. That set of diffraction points was used to solve the structure including anisotropic displacement parameters before a final refinement with all reflections. See Table 2.1 for crystallographic data, Table 2.2 for selected atomic coordinates, Figure 2.1 for a thermal ellipsoid plot, and Supporting Information for the crystallographic information file.

Powder X-ray Diffraction. Powder X-ray diffraction patterns were collected on a Rigaku XDS 2000 with Ni filtered Cu K α radiation ($\lambda = 1.5418 \text{ \AA}$) and compared with patterns recorded in the JCPDS (Joint Committee of Powder Diffraction Standards) database.

Table 2.1 Crystallographic Data for Ag₃VO₄

formula	Ag ₃ VO ₄
fw	438.55
space group	C2/c (No. 15)
<i>a</i> (Å)	10.1885(16)
<i>b</i> (Å)	4.9751(8)
<i>c</i> (Å)	10.2014(17)
β (deg)	115.754(3)
<i>V</i> (Å ³)	465.73(13)
<i>Z</i>	4
<i>T</i> (°C)	−120(2)
λ (Å)	0.71069
ρ_{calc} (g/cm ³)	6.254
μ (mm ^{−1})	14.266
<i>R</i> (<i>F</i>) ^a	0.0295
<i>wR</i> 2(<i>F</i> ²) ^b	0.0771

$$^a R = \sum \|F_o\| - \|F_c\| / \sum \|F_o\|$$

$$^b wR2 = [\sum w(F_o^2 - F_c^2)^2 / \sum w(F_o^2)^2]^{1/2}$$

$$w = 1 / [\sigma^2(F_o^2) + (aP)^2 + bP], P = (F_o^2 + 2F_c^2) / 3,$$

$$a = 0.053, b = 1.7241$$

Table 2.2 Selected Atomic Coordinates for Ag₃VO₄

atom	site	<i>x</i>	<i>y</i>	<i>z</i>	<i>U</i> (eq), ^a Å ²
Ag1	8f	0.23997 (5)	0.03982 (9)	0.09805 (5)	0.01355 (19)
Ag2	4b	0.5000	0.0000	0.5000	0.0168 (2)
V1	4e	0.5000	0.4638 (3)	0.2500	0.0103 (3)
O1	8f	0.3815 (4)	0.2655 (8)	0.2886 (4)	0.0155 (8)
O2	8f	0.0933 (4)	−0.1659 (8)	−0.1029 (4)	0.0161 (8)

^a *U*(eq) is defined as one-third of the trace of the orthogonalized *U*_{ij} tensor.

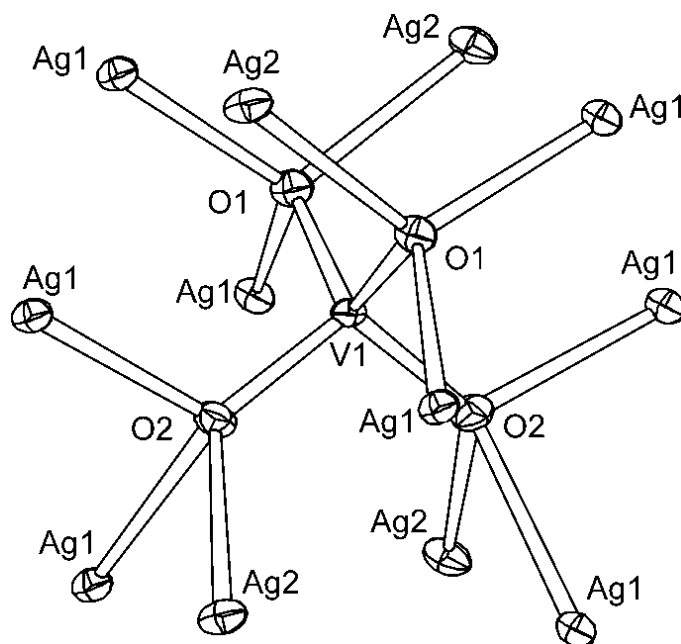


Figure 2.1 Thermal ellipsoid plot (showing 50% probability) of α - Ag_3VO_4 . Vanadium is tetrahedrally coordinated to four tetrahedrally-coordinated oxygen anions.

2.3 Results

2.3.1 Synthesis

From the hydrothermal reactions and conditions reported herein, four silver vanadium oxides and one silver vanadium oxide fluoride were observed. Polycrystalline $\text{Ag}_2\text{V}_4\text{O}_{11}$ and β - AgVO_3 and single crystals of $\text{Ag}_4\text{V}_2\text{O}_6\text{F}_2$, $\text{Ag}_4\text{V}_2\text{O}_7$, and α - Ag_3VO_4 , the structure of the latter is reported here also, were synthesized by reaction of the binary oxides Ag_2O and V_2O_5 with $\text{HF}_{(\text{aq})}$ as a mineralizer in a pressure vessel at 150 to 200 °C under autogenous pressure. The composition space for Ag_2O – V_2O_5 – $\text{HF}_{(\text{aq})}$ was constructed by varying the molar ratio of reagents while maintaining a constant total number of moles. Regions in the composition space diagram are outlined based on the identity of the recovered products as determined by powder X-ray diffraction. Though a mixture of two products is recovered from reactions when a composition

lies on or near a boundary between regions, single phases were formed in the middle of a defined region.

2.3.2 Structural Description

The structure of α -Ag₃VO₄ consists of a cubic close-packed arrangement of metal ions (silver and vanadium) with the oxide anions occupying half of the tetrahedral positions, roughly creating an “anti” sphalerite-type (ZnS) structure. However, sphalerite-type does not adequately describe the extended structure for a number of reasons. First, the cations occupy the close-packed positions rather than anions (ergo the “anti” modifier). Second, the oxide anions are split between T₊ and T₋ holes (Figure 2.2-2.3), which also changes the coordination around the cations, in this case, only around silver, while vanadium is tetrahedrally coordinated to four oxide ligands and resides on a 2 rotational axis. The presence of isolated [VO₄]³⁻ tetrahedra had been demonstrated previously by infrared and Raman studies.²⁸ The [VO₄]³⁻ anion has bond lengths of V-O1 = 1.732(4) Å and V-O2 = 1.711(4) Å and bond angles of O1-V-O1 = 110.5(3)°, O1-V-O2 = 110.95(18)° and 108.18(18)°, and O2-V-O2 = 108.0(3)°. Silver in α -Ag₃VO₄ has two different coordination spheres (Figure 2.4-2.5). With four oxide ligands, silver is either distorted square planar with local D_{2h} symmetry (or exhibiting a 2 rotation within the extended structure), or in a pseudo see-saw arrangement with local C symmetry. The volume around silver beyond the oxygen coordination sphere includes more silver at distances of 2.9619(9) Å, 3.1771(6) Å, and 3.2190(6) Å within a close packed layer (Figure 2.6). Silver silver distances less than 3.0 Å are common to a few solid state compounds, including silver pyrovanadate, Ag₄V₂O₇, which has minimum silver distances of 2.989 Å.^{16,29} Characteristics such as a sharp absorption edge in the UV-visible light spectrum and electrical and ionic conductivity are

common to materials with d^{10} silver cations. Indeed, α - Ag_3VO_4 is bright red and was reported to increase the ionic conductivity of silver at ambient temperature when added to either CuI or AgI .^{30,31}

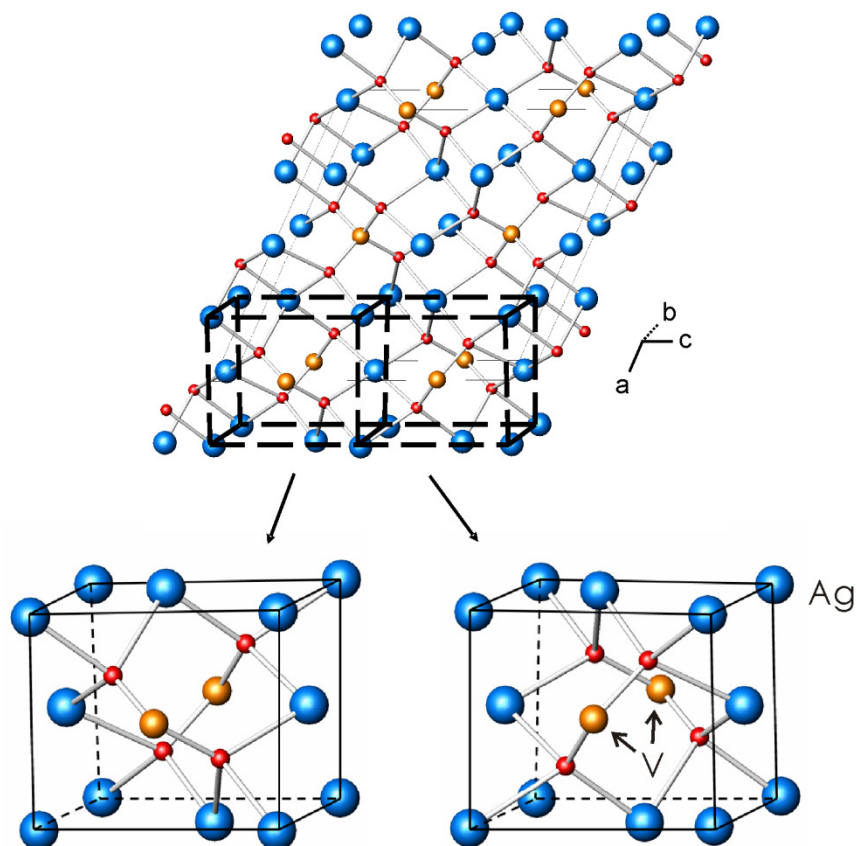


Figure 2.2 Primitive cells in α - Ag_3VO_4 have a distorted “anti” sphalerite-type structure of face-centered Ag and V cations with O^{2-} anions in either T_+ or T_- holes. Blue = Ag, Orange = V, Red = O.

K_3VO_4 and $\text{K}_3\text{Cr}(\text{O}_2)_4$ are two compounds with structures similar to that of α - Ag_3VO_4 .^{32,33} Both structures are “anti” sphalerite-type with cations in a cubic close-packed arrangement and the oxide or peroxide anions, unlike α - Ag_3VO_4 , occupy in only the T_+ holes. The reason why α - Ag_3VO_4 exhibits alternating cells of opposite tetrahedral positions may be

because of the interactions between silver ions. Jansen notes that there are frequently drastic differences between structures of ternary silver (I) oxides and their sodium or potassium analogues, where the monovalent cation is present in a high ratio, such as the tendency for the silver cations to aggregate to form two-dimensional ribbons or layers with the silver-silver distances less than 3.30 \AA .²⁹

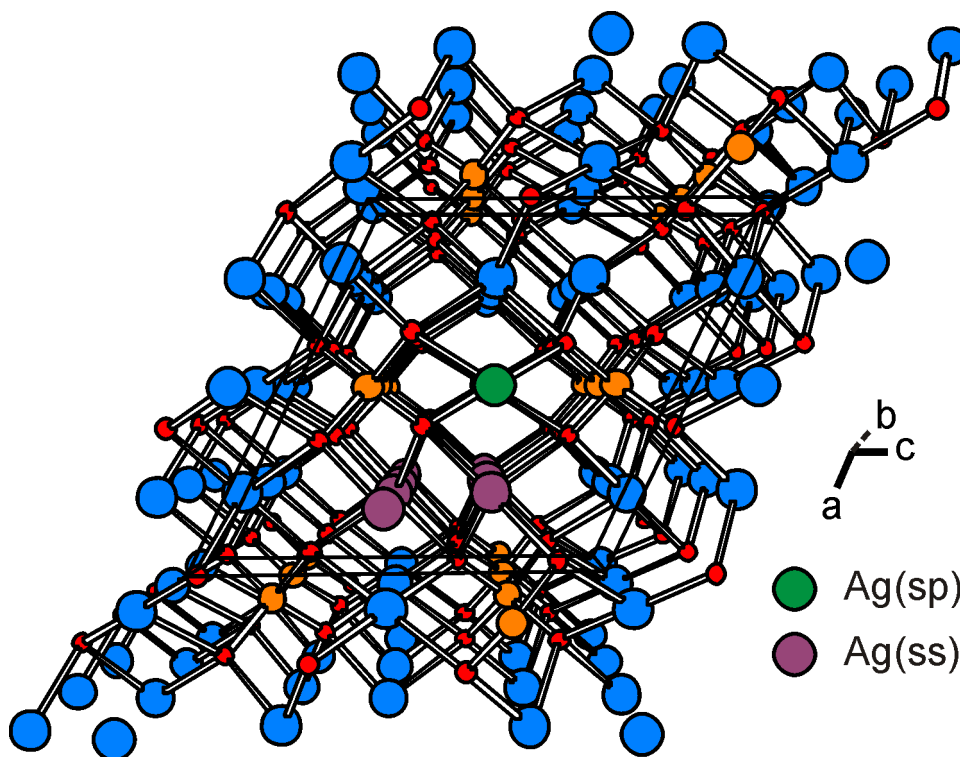


Figure 2.3 Perspective drawing of Ag_3VO_4 . The off-center purple atoms are the see-saw coordinated Ag1 and the central green atoms are Ag2 in the nearly square planer coordination. Blue = Ag, Orange = V, Red = O.

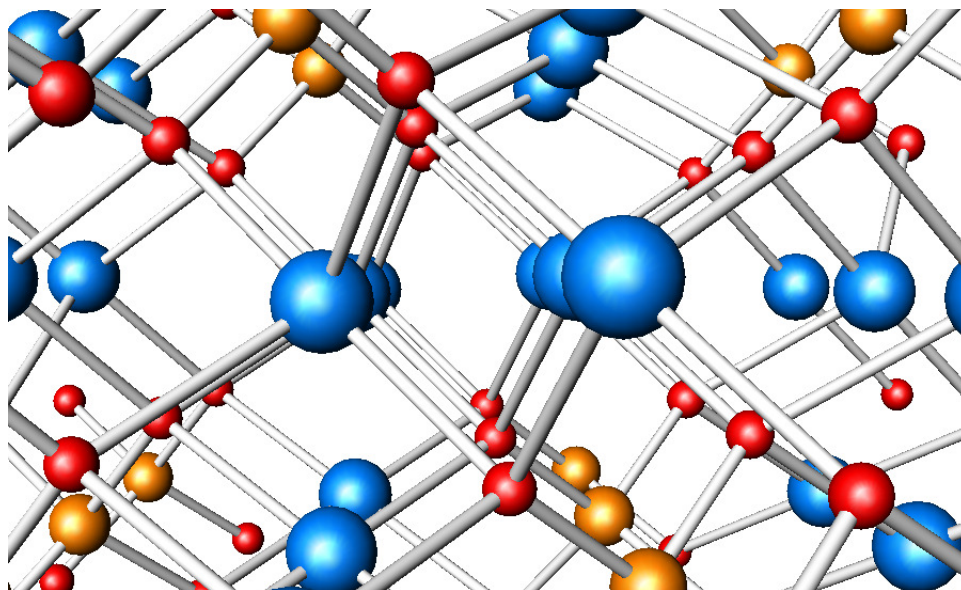


Figure 2.4 Perspective drawing of Ag_3VO_4 . In the center are the see-saw Ag1. Blue = Ag, Orange = V, Red = O.

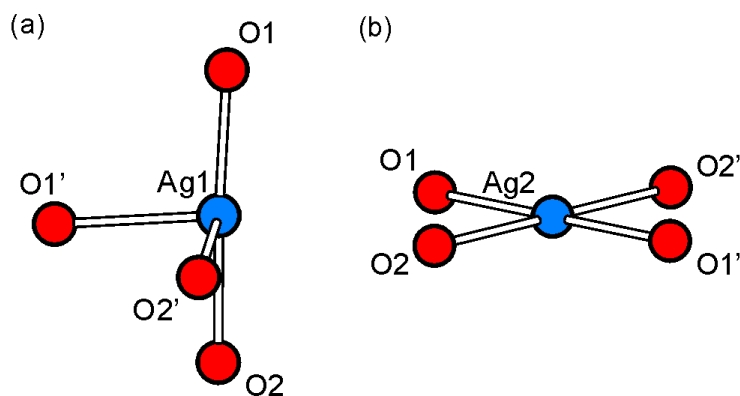


Figure 2.5 Coordination environment of silver atoms in $\alpha\text{-Ag}_3\text{VO}_4$. (a) Pseudo see-saw with bond angles of $\text{O1-Ag1-O1}' = 98.13(9)^\circ$, $\text{O1-Ag1-O2}' = 100.73(14)^\circ$, $\text{O1-Ag1-O2} = 176.47(15)^\circ$, $\text{O1}'\text{-Ag1-O2}' = 91.11(13)^\circ$, $\text{O1}'\text{-Ag1-O2} = 84.40(13)^\circ$, and $\text{O2}'\text{-Ag1-O2} = 81.54(14)^\circ$ and bond lengths $\text{Ag1-O1} = 2.164(4) \text{ \AA}$, $\text{Ag1-O1}' = 2.444(4) \text{ \AA}$, $\text{Ag1-O2} = 2.505(4) \text{ \AA}$, and $\text{Ag1-O2}' = 2.196(4) \text{ \AA}$. (b) Distorted square planer with linear $\text{O1-Ag2-O1}'$ and $\text{O2-Ag2-O2}'$ bond angles and $\text{O1-Ag2-O2} = 97.57(14)^\circ$ and bond lengths $\text{Ag2-O1/O1}' = 2.364(4) \text{ \AA}$ and $\text{Ag2-O2/O2}' = 2.374(4) \text{ \AA}$.

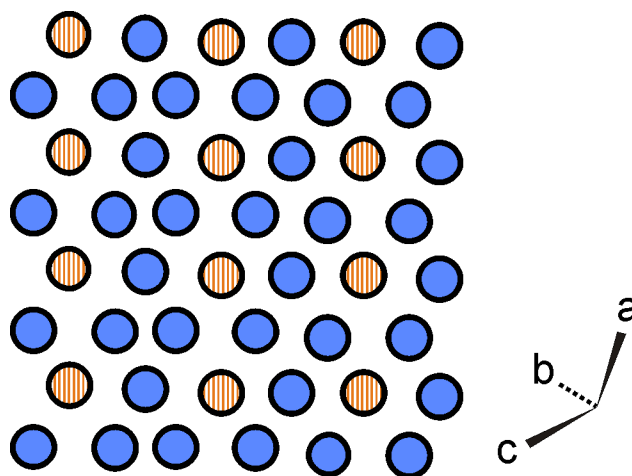


Figure 2.6 A close packed layer in α - Ag_3VO_4 . Blue = Ag, Orange stripes = V.

2.4 Discussion

At different mole ratios of Ag_2O , V_2O_5 , and $\text{HF}_{(\text{aq})}$ in the hydrothermal system at 150 °C, $\text{Ag}_2\text{V}_4\text{O}_{11}$, β - AgVO_3 , $\text{Ag}_4\text{V}_2\text{O}_6\text{F}_2$, and α - Ag_3VO_4 are observed (Figure 2.7). Unlike the solid state reaction products, $\text{AgV}_7\text{O}_{18}$ and $\text{Ag}_4\text{V}_2\text{O}_7$ were not observed.¹³ Particularly noteworthy is the presence of a single oxyfluoride $\text{Ag}_4\text{V}_2\text{O}_6\text{F}_2$ and the absence of the oxide $\text{Ag}_4\text{V}_2\text{O}_7$ (at 150 °C), both which have the same Ag:V ratio. However, at 200 °C, $\text{Ag}_4\text{V}_2\text{O}_7$ is observed instead of $\text{Ag}_4\text{V}_2\text{O}_6\text{F}_2$, which will be addressed later. The composition space focused on the $\text{HF}_{(\text{aq})}$ -rich region because experiments with insufficient $\text{HF}_{(\text{aq})}$ under any of the aforementioned conditions resulted in incomplete solubilization and only partial reaction of the reactants. In addition, in order to optimize the synthesis (in particular the yield) of $\text{Ag}_4\text{V}_2\text{O}_6\text{F}_2$, the composition space diagram was studied in two different ways. First, varying the $\text{Ag}_2\text{O}:\text{V}_2\text{O}_5$ ratio while maintaining a constant overall metal-oxide: $\text{HF}_{(\text{aq})}$ ratio (Figure 2.7, Line A), and second, keeping the $\text{Ag}_2\text{O}:\text{V}_2\text{O}_5$ ratio fixed while varying the amount of $\text{HF}_{(\text{aq})}$ in the system (Figure 2.7, Line B).

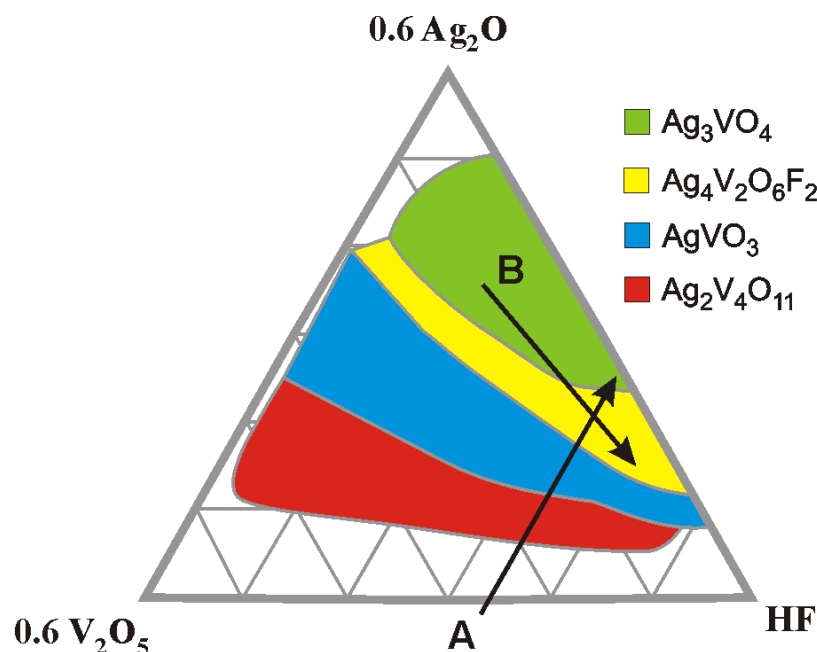


Figure 2.7 Composition space for the hydrothermal system of $\text{Ag}_2\text{O}-\text{V}_2\text{O}_5-\text{HF}_{(\text{aq})}$. Formation regions for the silver vanadates and the silver vanadium oxide fluoride are outlined. Line A represents a constant $\text{HF}_{(\text{aq})}$ quantity while varying $\text{Ag}_2\text{O}:\text{V}_2\text{O}_5$ ratio, increasing toward a higher silver fraction. Line B represents a constant 4:1 $\text{Ag}_2\text{O}:\text{V}_2\text{O}_5$ ratio, increasing toward a higher $\text{HF}_{(\text{aq})}$ fraction.

Constant $\text{HF}_{(\text{aq})}$. In the first trend, reactions with an increasing $\text{Ag}_2\text{O}:\text{V}_2\text{O}_5$ ratio yield products with higher silver contents. However, there is no direct stoichiometric relationship between the $\text{Ag}_2\text{O}:\text{V}_2\text{O}_5$ starting ratio and the silver to vanadium ratio in the product. For example, 1:1 $\text{Ag}_2\text{O}:\text{V}_2\text{O}_5$ in a hydrothermal reaction (this work), in a typical solid state reaction, or in a mechanochemical reaction yields $\beta\text{-AgVO}_3$.^{13,20,34} However, at 2:1 $\text{Ag}_2\text{O}:\text{V}_2\text{O}_5$ the reported system (with an appropriate quantity of $\text{HF}_{(\text{aq})}$, mentioned later) yields $\beta\text{-AgVO}_3$, whereas in solid state and mechanochemical reactions $\text{Ag}_4\text{V}_2\text{O}_7$ forms. For hydrothermal reactions, $\text{Ag}_4\text{V}_2\text{O}_6\text{F}_2$ is phase pure at 4:1 $\text{Ag}_2\text{O}:\text{V}_2\text{O}_5$, and similarly $\alpha\text{-Ag}_3\text{VO}_4$ is only obtained phase-pure at ratios of 8:1 $\text{Ag}_2\text{O}:\text{V}_2\text{O}_5$. The silver not incorporated in the final solid product for the reported system remains in solution, rather than forming an amorphous phase, as evidenced

by precipitation of AgCl with hydrochloric acid. Other hydrothermal syntheses of silver-containing compounds have also been more successful (higher yield) upon an excess addition of the silver-containing reagent.^{35,36} Indeed, as early as 1930, it was noted that precipitation of Ag_3VO_4 from 3:1 sodium vanadate and AgNO_3 occurred more readily with excess AgNO_3 .¹¹

Constant $\text{Ag}_2\text{O}:\text{V}_2\text{O}_5$. The second trend in the $\text{Ag}_2\text{O}-\text{V}_2\text{O}_5-\text{HF}_{(\text{aq})}$ composition space shows that product formation depends on the quantity of $\text{HF}_{(\text{aq})}$ added, while maintaining a constant $\text{Ag}_2\text{O}:\text{V}_2\text{O}_5$ ratio. The mineralizer in the hydrothermal reactions plays an important role in determining the speciation and solubilities of reactants. Reactions are more favorable when the mineralizer initially helps solubilize the reactants, but if the mineralizer prevents any product from forming by either dissolving it or stabilizing the reactant species in solution, no reaction occurs.³⁷ In the aforementioned system, the higher mole ratio of $\text{HF}_{(\text{aq})}$ solubilizes some of the silver well enough to prevent it from combining with vanadium into a precipitate (Table 2.3). At a 1:1 $\text{Ag}_2\text{O}:\text{V}_2\text{O}_5$ ratio, $\beta\text{-AgVO}_3$ was obtained at a low $\text{HF}_{(\text{aq})}$ quantity and $\text{Ag}_2\text{V}_4\text{O}_{11}$ was made by increasing the $\text{HF}_{(\text{aq})}$ content. At a 2:1 $\text{Ag}_2\text{O}:\text{V}_2\text{O}_5$ ratio, $\text{Ag}_4\text{V}_2\text{O}_6\text{F}_2$ formed with a low $\text{HF}_{(\text{aq})}$ concentration, and increasing the $\text{HF}_{(\text{aq})}$ quantity yielded AgVO_3 . Finally, at a 4:1 $\text{Ag}_2\text{O}:\text{V}_2\text{O}_5$ ratio, $\alpha\text{-Ag}_3\text{VO}_4$ formed with a low $\text{HF}_{(\text{aq})}$ concentration while $\text{Ag}_4\text{V}_2\text{O}_6\text{F}_2$ formed at a higher $\text{HF}_{(\text{aq})}$ concentration.

Table 2.3 Dependency of product on the molar concentration of $\text{HF}_{(\text{aq})}$ in the hydrothermal $\text{Ag}_2\text{O}-\text{V}_2\text{O}_5-\text{HF}_{(\text{aq})}$ system.

$\text{Ag}:\text{V}:\text{HF}_{(\text{aq})}^*$	$\text{Ag}_2\text{V}_4\text{O}_{11}$	AgVO_3	$\text{Ag}_4\text{V}_2\text{O}_6\text{F}_2$	Ag_3VO_4
1 : 1 : x	x = 8	4		
2 : 1 : x		15	7	
4 : 1 : x			15	4
8 : 1 : x				20

* The values for x are not accounting for the moles of water in $\text{HF}_{(\text{aq})}$.

The two tendencies above, however, do not address completely the formation of $\text{Ag}_4\text{V}_2\text{O}_7$ in lieu of $\text{Ag}_4\text{V}_2\text{O}_6\text{F}_2$ in the composition space. Originally with the intent of growing larger crystals of $\text{Ag}_4\text{V}_2\text{O}_6\text{F}_2$, hydrothermal reactions were carried out at higher temperatures (200 °C) where larger, red-orange crystals of $\text{Ag}_4\text{V}_2\text{O}_7$ were recovered. To study the differences between the two systems producing $\text{Ag}_4\text{V}_2\text{O}_6\text{F}_2$ and $\text{Ag}_4\text{V}_2\text{O}_7$, a series of reactions was performed using various heating temperatures and durations (equal amounts of reactants were loaded into the reaction pouches to form the two different products). Similar heating profiles were used, as described previously, with holding the maximum temperature between 150 °C and 200 °C at 10 °C increments. Whereas $\text{Ag}_4\text{V}_2\text{O}_7$ was observed at temperatures as low as 170 °C, it was the dominant phase replacing $\text{Ag}_4\text{V}_2\text{O}_6\text{F}_2$ above 190 °C. The silver vanadium oxide phases observed from reactions at 150 °C were also observed from reactions at 200 °C. Because reactions heated to a maximum temperature of 200 °C were cooled slowly, such reactions would be at temperature above 150 °C for 500 minutes longer than those where the maximum temperature was initially 150 °C. Adjustments to the heating duration such that the total reaction time (heating and cooling) were the same at any given maximum temperature yielded no difference.

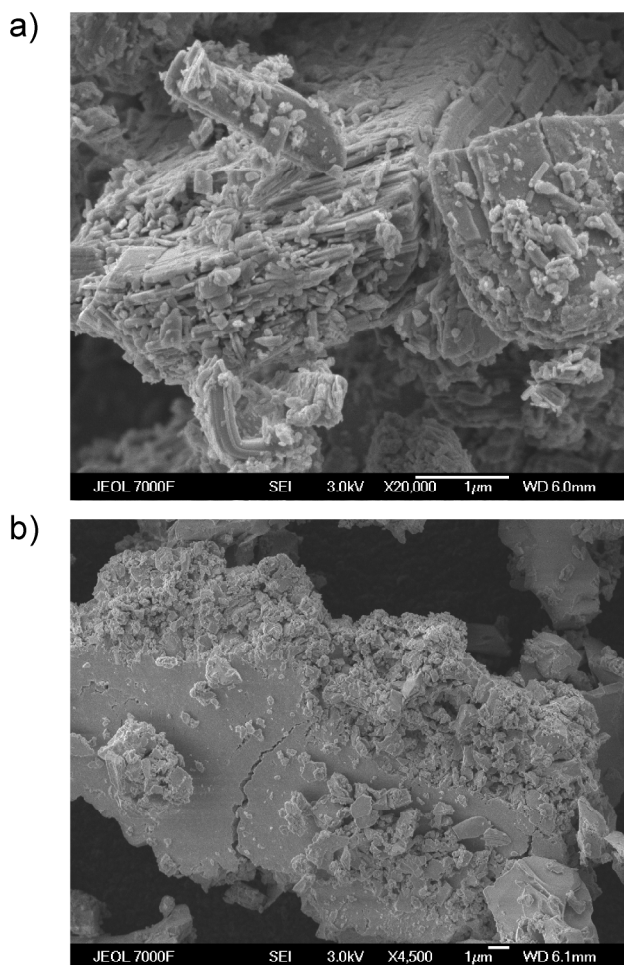


Figure 2.8 SEM of (a) $\text{Ag}_2\text{V}_4\text{O}_{11}$ and (b) $\text{Ag}_4\text{V}_2\text{O}_6\text{F}_2$ particles from hydrothermal synthesis.

In regard to the earlier discussion on small particle sizes of the battery material $\text{Ag}_2\text{V}_4\text{O}_{11}$, the particle sizes the battery materials made in the reported system were considered. Synthesis of $\text{Ag}_2\text{V}_4\text{O}_{11}$ yielded particles that are on the order of one micrometer in dimensions (Figure 2.8a).³⁸ In contrast, the particle sizes of as prepared $\text{Ag}_4\text{V}_2\text{O}_6\text{F}_2$ are more widely dispersed from large crystals to sub-micron particles (Figure 2.8b). Synthesis of more uniformly small sized particles may also improve the performance of batteries incorporating $\text{Ag}_4\text{V}_2\text{O}_6\text{F}_2$ as the active cathode material.

2.5 Conclusions

The $\text{Ag}_2\text{O}-\text{V}_2\text{O}_5-\text{HF}_{(\text{aq})}$ system produces a variety of silver vanadium oxides and one silver vanadium oxide fluoride under the hydrothermal conditions at 150 °C. Elevating the temperature, $\text{Ag}_4\text{V}_2\text{O}_7$ is formed instead of $\text{Ag}_4\text{V}_2\text{O}_6\text{F}_2$ at 200 °C. The versatility of this system was shown in producing four stoichiometrically different silver vanadium oxides, as well as forming particles of $\text{Ag}_2\text{V}_4\text{O}_{11}$ potentially small enough for improving specific applications and excellent crystals of $\alpha\text{-Ag}_3\text{VO}_4$ large enough for the single-crystal X-ray diffraction study.

Chapter Three
In-Depth Electrochemical Characterization of $\text{Ag}_4\text{V}_2\text{O}_6\text{F}_2$

3.1 Introduction

Inorganic chemistry plays an active role in many different fields of medicine. For example, inorganic chemists are involved in the development of electrochemical-based ion/molecular sensors to analyze and quantify *in situ* and/or *in vivo* vital signs. They also contribute to advances in the elaboration of biomaterial compatible glasses for bone grafting or, more generally, for restorative surgery. One significant step forward in the bio-medical area that inorganic chemistry has made possible is the management of cardiac dysfunction including arrhythmia. Years of intensive research have led to small and more efficient batteries as the power source for implantable cardioverter defibrillators (ICDs). To meet the stringent requirements of high energy output and reliability, the cathode material of the lithium primary battery is at the core of ICD research. Since 1984, $\text{Ag}_2\text{V}_4\text{O}_{11}$ (SVO) has provided the high chemical/electrochemical stability and high discharge rate required of the cathode material. To replace SVO, a new material would need to display a higher volumetric capacity and redox potential while maintaining the above-mentioned electrochemical characteristics.

Implantable Cardioverter Defibrillators (ICDs) enable the treatment of human ventricular fibrillation by administering either a 700-800 V shock to the right ventricle or a low-energy stimulus similar to a cardiac pacemaker. Since its invention more than 25 years ago, seven generations of power sources for ICD have been subsequently reported.¹ The volumetric efficiency was improved between these designs and is considered more important than the gravimetric capacity in order that the device is of a reasonable size in the chest cavity. Two such improvements were the reduced headspace and separator volume. In addition, the transition from a two-cell to a single cell battery was, from a technological point of view, a significant breakthrough in ICD size reduction. This device delivers therapy from a lithium primary battery

supplying two parallel capacitors to drive high voltage pulse discharges. These capacitors are charged within a few seconds to administer eventual subsequent discharges.² For this reason, during the battery's discharge, the successive electrochemical steps necessitate high kinetics and good Li^+/e^- conduction to reduce battery polarization and to maintain efficient delivery of battery power. Meeting these requirements, the cathode $\text{Ag}_2\text{V}_4\text{O}_{11}$ (SVO) has been a commercial success because of its high chemical stability³ and good electron/ion conductivity ($\sigma_{\text{e}} \sim 10^{-2}$ S/cm and $\text{D}_{(\text{Li}^+)} \sim 10^{-8}$ cm²/s).^{4,5} The electrode has been so carefully optimized that SVO provides performance close to what can be theoretically expected. To realize additional size reduction and to achieve the next level in performance, new cathode materials exhibiting a higher volumetric capacity and a greater capacity above 3 V (vs. Li^+/Li^0), while maintaining high electrode stability and discharge rates, will be required.

To address these issues, our approach is to synthesize new materials with significantly greater Ag/V ratios and partial fluoride substitution for oxide to increase the cell potential.⁶ Our group reported recently the reactions of Ag_2O and V_2O_5 in $\text{HF}_{(\text{aq})}$ under hydrothermal conditions.⁷ This study established the preferred composition and relative solubilities which lead to the formation of red, transparent single crystals of the new silver vanadium oxyfluoride $\text{Ag}_4\text{V}_2\text{O}_6\text{F}_2$ (SVOF). Preliminary characterizational and electrochemical results, including a higher crystal structure density of 6.03 g/cm³ (vs. 4.80 g/cm³ for SVO) and a higher capacity above 3 V (vs. Li^+/Li^0), were encouraging.^{6,8} From a capacity point of view, SVO can deliver approximately 100 mAh/g above 3 V, which is largely due to the reduction of silver; by comparison, the greater Ag/V ratio enables SVOF to exhibit a superior capacity of *c.a.* 148 mAh/g through two biphasic transitions at around 3.40 V and 3.20 V (vs. Li^+/Li^0). It is also

noteworthy, owing to its high density ($\rho = 6.03 \text{ g/cm}^3$), that SVOF can provide almost twice the volumetric capacity above 3 V as compared to SVO, 892 mAh/cm^3 vs. 479 mAh/cm^3 , respectively.

In light of SVOF's potential as a new cathode for medical battery applications, we embarked on this collaboration to gather additional information on the electrochemical reactivity of SVOF vs. lithium and the lithium insertion mechanism. To understand the aforementioned properties and processes, *in situ* XRD measurements during electrode reduction, as well as Electron Paramagnetic Resonance (EPR) and High Resolution Transmission Electron Microscopy (HRTEM) investigations were pursued. The combined results will be discussed and a mechanism proposed.

3.2 Synthesis and Characterization

3.2.1 Materials

Caution. Hydrofluoric acid is toxic and corrosive and must be handled with extreme caution and the appropriate protective gear! If contact with the liquid or vapor occurs, proper treatment procedures should be followed immediately.⁹⁻¹¹

Materials. Ag_2O (99%, Fisher), V_2O_5 (99.6%, Alfa-Aesar), and aqueous hydrofluoric acid (48-50% HF by weight, Fisher) were used as received.

3.2.2 Synthesis

$\text{Ag}_4\text{V}_2\text{O}_6\text{F}_2$ was synthesized successfully as a single phase from autogenous hydrothermal conditions.^{6,7} The reactants consisting of 0.3972 g Ag_2O , 0.0779 g V_2O_5 and 0.2572 g of $\text{HF}_{(\text{aq})}$ (48-50% by weight) corresponding to a 4:1 Ag:V molar ratio were combined within a FEP Teflon pouch.¹² The sealed pouch was then placed in a 125 mL PTFE Teflon lined autoclave

(Parr Instruments) which was backfilled with 42 mL de-ionized H₂O. The autoclave was heated for 24 hours at 150 °C and cooled at 0.1 °C/min to room temperature. Around 0.25 g of water from the backfill entered the pouch during the reaction owing to the semi-permeability of the FEP Teflon to water above 120 °C. Finally, the pouch was opened under air and the products filtered to retrieve red crystals of Ag₄V₂O₆F₂ in 85% yield based on V.

3.2.3 Characterization

Powder X-ray Diffraction. The X-ray diffraction (XRD) patterns were recorded in a ($\theta/2\theta$) configuration using a Bruker D8 diffractometer with Cu K α radiation ($\lambda = 0.15418$ nm).

Electron Microscopy. The particle size and morphology was investigated using an Environmental Scanning Electron Microscopy (ESEM) FEI Quanta 200FEG coupled with an Energy Dispersion Spectroscopy (EDS) analysis system (Oxford Link Isis). To further investigate the local structure of the discharged material, HRTEM experiments were also performed using a FEI Tecnai F-20 S-twin microscope. For this, the battery was dismantled in an Ar-filled glove box and the retrieved cathode product was thoroughly washed three times in dimethyl carbonate (DMC) before being deposited on a copper grid coated with a lacey-carbon film. A home-designed TEM sample holder, which allows the investigation of air sensitive materials, was used to prevent the discharged SVOF from further reaction or decomposition prior to the microscopy investigations.

Electron Paramagnetic Resonance. EPR experiments were performed on different electrochemically lithiated SVOF materials (from Li₀Ag₄V₂O₆F₂ to Li_{3.5}Ag₄V₂O₆F₂) at room temperature and 4 K using a Bruker ELEXYS E580 X band spectrometer with an amplitude modulation of 1 G and microwave power of 2 mW for Continuous Wave (CW) experiments. To recover the partially lithiated material, the batteries were dismantled in an Ar-filled glove box

and rinsed with DMC. The material was transferred to the EPR tube and sealed while in the glove box, and then flame sealed under vacuum. The three-pulse Electron Spin Echo Envelope Modulation (ESEEM) experiment $\pi/2 - \tau - \pi/2 - T - \pi/2 - \tau$ echo was performed with 16 ns $\pi/2$ pulse duration, and the time domain were recorded at $\tau+T$ and extracted from Fourier transform. Experiments were recorded at various τ values to avoid the inherent “blind spots” in such a sequence.

Electrochemical Characterization. The electrochemical characterization of SVOF was carried out by manually grinding and mixing the single crystals with 14% wt. SP-type carbon black. The measurements were recorded following a two-electrode configuration using a Swagelok-type cell assembled in an Ar filled glove box. Lithium metal foil was used as the counter and reference electrodes. Two pieces of Whatman GF/D borosilicate glass fiber sheets were thoroughly soaked with 1M LiPF₆ EC / DMC 1:1 electrolyte (LP30 - Merck Selectipur grade). The electrode cycling tests were monitored by a VMP.

***In situ* Powder X-ray Diffraction and Electrochemistry.** In complement to these techniques, *in situ* XRD experiments, recorded on a Bruker D8 diffractometer with a copper anti-cathode, were performed by utilizing an electrochemical cell capped by a beryllium window functioning as the positive current collector. The electrochemistry of this cell was controlled by a Mac Pile galvanostat system, at a discharge rate of *c.a.* D/10 (insertion of 1 Li⁺ in 10 h) and XRD patterns were collected at intervals of 0.09 Li⁺ per formula unit.

3.3 Results

3.3.1 Synthesis

Following the synthetic route described in the experimental section, pure and well crystallized SVOF is easily prepared (Figure 3.1). The unit cell parameters were refined using the reported monoclinic crystal structure and Fullprof software in full pattern matching mode.¹³ The cell parameters thus obtained ($a = 5.596(1)$ Å, $b = 10.554(2)$ Å, $c = 12.516(3)$ Å and $\beta = 90.464(6)^\circ$) were in agreement with those reported from the single crystal structure determination. As a result of the grinding/mixing step with carbon, the needle-like single crystals of SVOF were broken into irregular pieces of heterogeneous size up to ~ 20 μm (Figure 3.1 inset). Energy-dispersive X-ray spectroscopy (EDS) acquisitions on different areas revealed the appropriate $\text{Ag}/\text{V} = 2$ ratio within the particles.

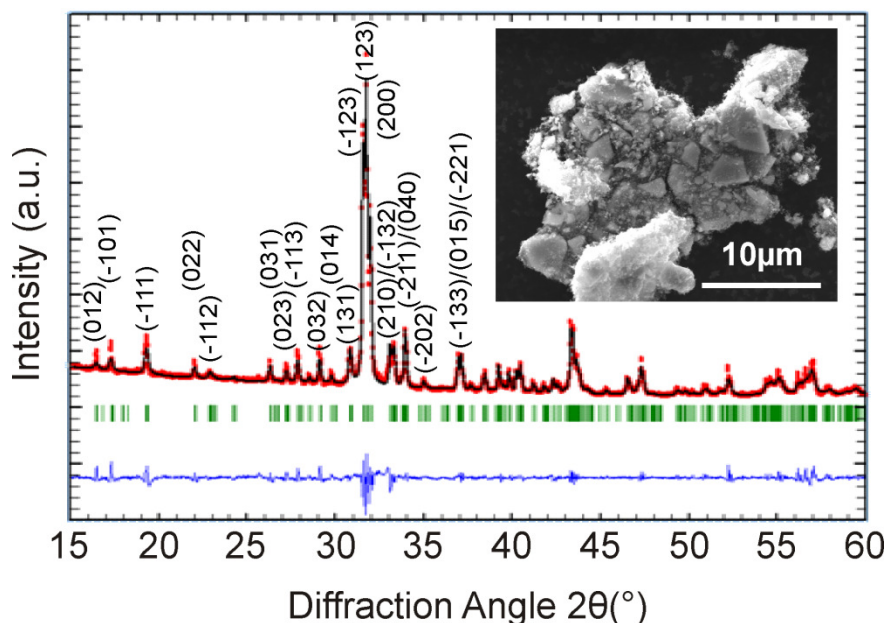


Figure 3.1 Full-pattern matching refinement of the powder X-ray diffraction pattern of ground $\text{Ag}_4\text{V}_2\text{O}_6\text{F}_2$ (SVOF). Inset: Scanning electron microscopy picture of the composite SVOF/ C_{sp} electrode.

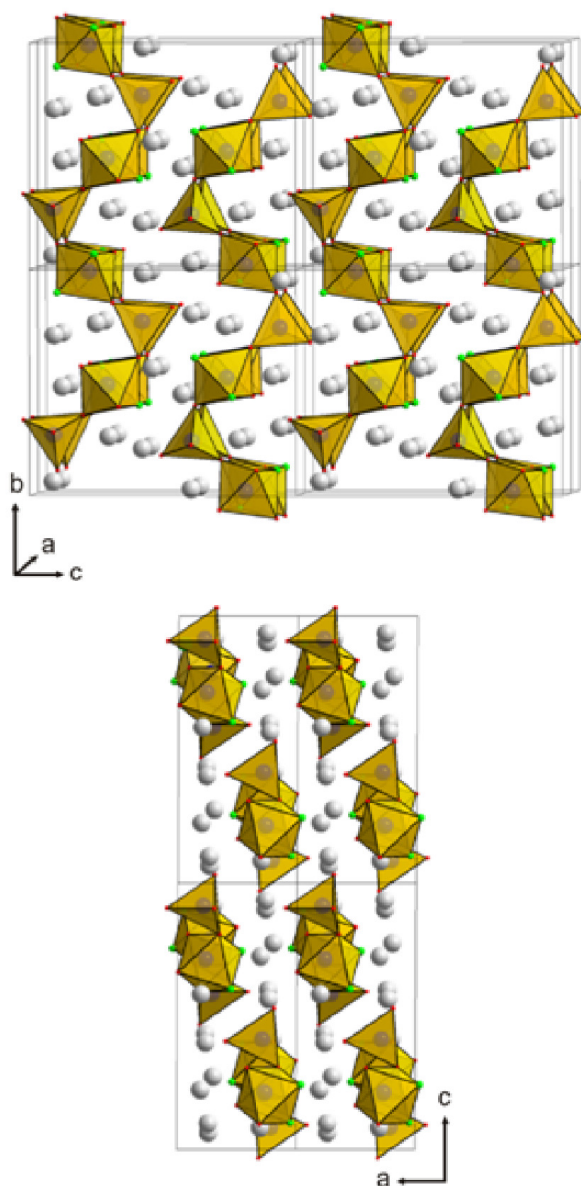


Figure 3.2 Structural representation of SVOF in the (bc) and (ac) planes with the V^{5+} -centered polyhedron.

The SVOF structure is composed (Figure 3.2) of isolated chains of alternating corner-sharing VO_4F_2 octahedra and VO_4 tetrahedra along the b axis. Between the (101) sheets of chains, silver cations are distributed among four distinct crystallographic sites where silver

adopts four-, five- or seven-fold coordination ($\text{Ag}(3)\text{O}_3\text{F}$, $\text{Ag}(1)\text{O}_4\text{F}$, $\text{Ag}(2)\text{O}_4\text{F}_3$ and $\text{Ag}(4)\text{O}_5\text{F}_2$). Although the crystallographic directions $[100]$ and $[010]$ appear favorable for silver ion diffusion, the optimal diffusion pathways are not yet understood.

3.3.2 Electrochemical Properties

Figure 3.3a shows a typical discharge/charge trace of SVOF down to a cut-off potential of *c.a.* 0.01 V (vs. Li^+/Li^0). Despite a moderate cycling rate (*i.e.* C/10), the reaction of lithium with SVOF appears mostly irreversible, in contrast to SVO.¹⁴⁻¹⁶ The entire discharge down to 0.01 V corresponds to the uptake of approximately 17.2 Li^+ per formula unit, or a gravimetric capacity of around 700 mAh/g (the capacity from C_{sp} is included in this value). Approximately half of this capacity is recovered during the subsequent charge. More insights on the electrochemical reversibility of the system are emphasized in Figure 3.3b. The cell recharge after 2 or 4 lithium inserted, corresponding to a cut-off potential of 3.01 V or 2.48 V (vs. Li^+/Li^0), depicts a highly irreversible Li reaction mechanism given that approximately 85% and 80% of the discharged capacity is not recovered, respectively. Lithium insertion into SVOF proceeds along two narrow plateaus above at ~3.45 V and 3.25 V in OCV conditions, followed by a smooth and continuous potential decrease reminiscent of solid solution behavior.⁶ In comparison to SVO, the increase of the silver reduction potential by about 300 mV is due to the presence of fluoride within the silver environment that modifies its chemical potential via a strengthening of the ionic character of the Ag-O/F bonds.

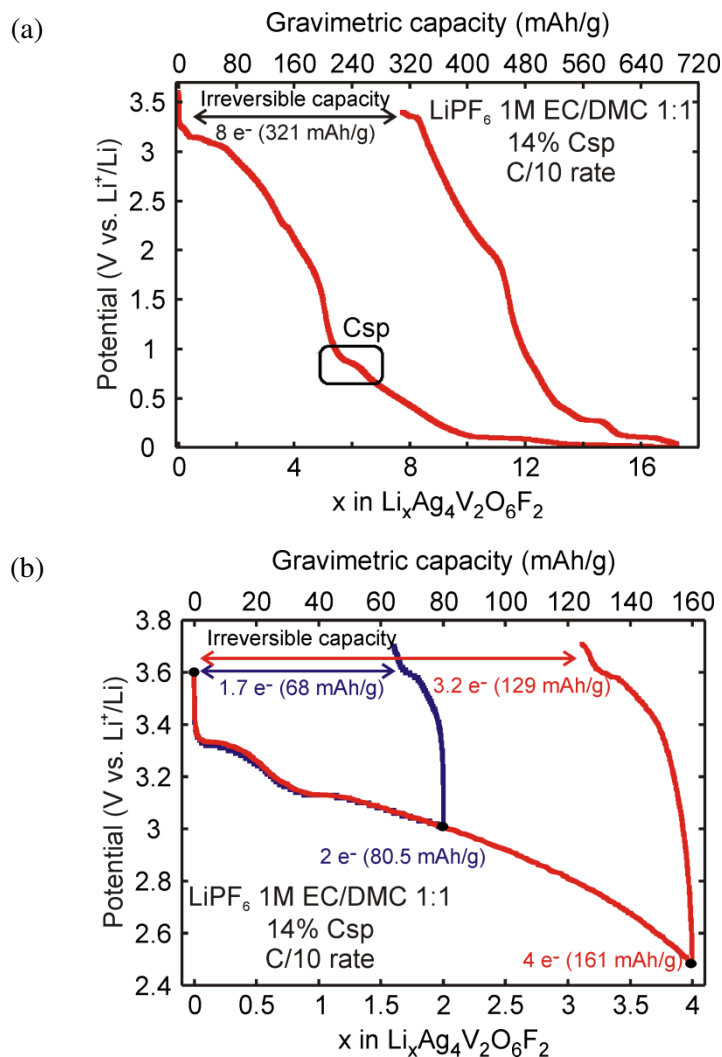


Figure 3.3 1st cycle galvanostatic curve recorded at C/10 rate of a composite SVOF/ C_{sp} electrode in 1M LiPF_6 EC/DMC 1:1 electrolyte (a) down to 0.01V cut-off potential (b) after two and four lithium inserted.

The discharge trace of SVOF is compared in Figure 3.4a to SVO synthesized by a similar solvothermal route.⁷ The SVO recovered from the hydrothermal synthesis formed needle-like, 2-5 μm in length, 0.2-1 μm wide, and 50-100 nm thick particles. Further details on the characterization and electrochemical properties of SVO obtained by this route will be reported elsewhere. As mentioned, by discharging both cathodes at D/50, SVOF exhibits a significantly

higher potential than SVO for the first 150 mAh/g, where a potential crossover between materials occurs. The benefit of SVOF above 3 V and 2.5 V is shown in Figure 3.4b, where the influence of the discharge rate on the capacity of SVOF and the SVO is depicted. A decrease of the capacity with increasing the discharge rate is noticed for SVOF and SVO. Such an influence of the discharge rate on the electrochemical capacity was reported for SVO prepared by a solid state reaction.¹⁷⁻¹⁹ While 148 mAh/g is thermodynamically available above 3 V for SVOF, 101 mAh/g is accessible at D/50, 80 mAh/g at D/10 and 16 mAh/g is recovered at D. At a cut-off potential of 2.5 V, a comparable capacity drop with the discharge rate is also observed (156 mAh/g, 147 mAh/g and 95 mAh/g recorded at D/50, D/10 and D rates, respectively). Owing to the fact that both compounds exhibit the formation of silver metal, which increases the electronic conductivity of the composite electrode, such power rate limitations, which can translate to high polarization observed on the charge/discharge curves, are more prone to originate from the structure rather than from electronic limitations. Nevertheless, it is important not to over-interpret this comparison since particle size; electrode porosity, etc. are parameters which can also affect the performance and rate capability of the electrode. A more extensive examination of the discharge curves at various rates reveals differences that suggest the lithium insertion and silver extraction are rather complex. In fact, a third feature appeared when the cell was more rapidly discharged at D while such an additional plateau does not appear when the cell is discharged at D/50 (Figure 3.4c, arrows).

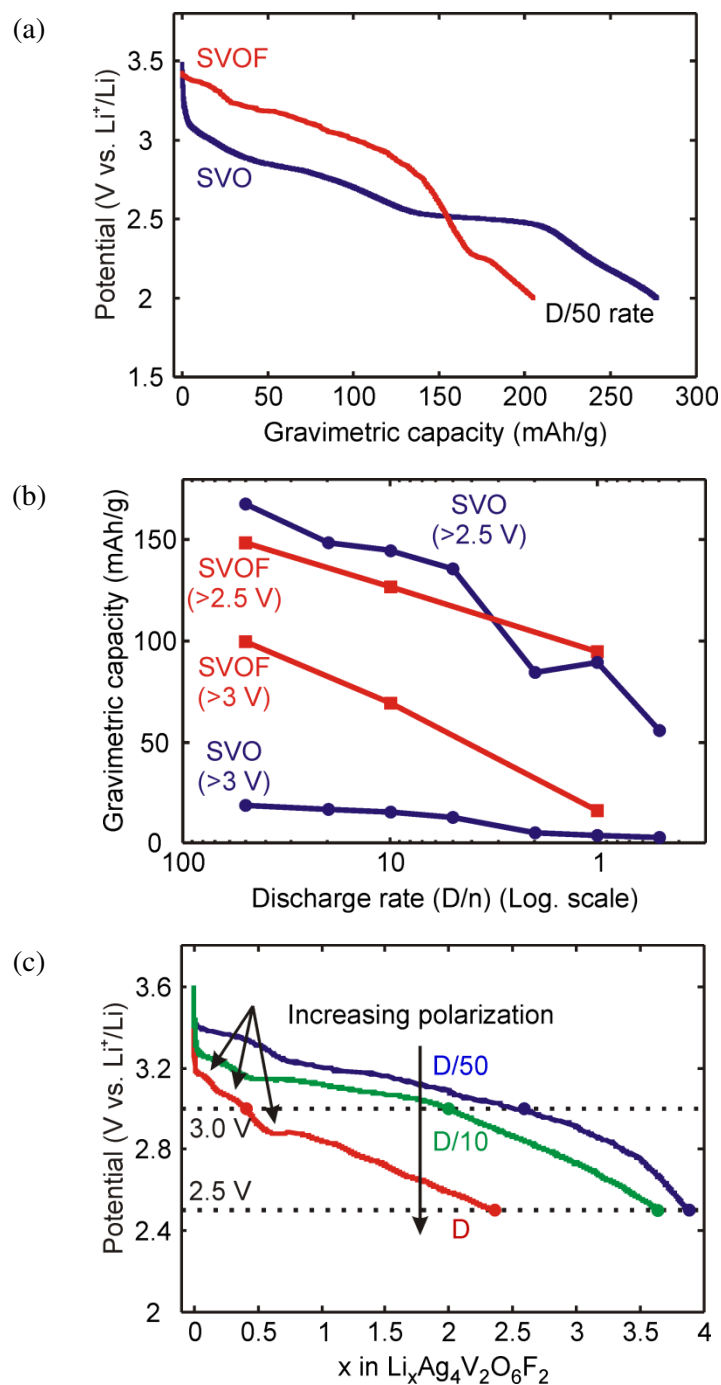


Figure 3.4 (a) Comparison of a galvanostatic-driven discharge performed at D/50 between SVOF and SVO synthesized by a similar solvothermal route. (b) Evolution of the electrode capacity as a function of the discharge rate beyond 3 V and 2.5 V for SVOF and SVO. (c) Influence of the discharge rate on the electrochemical discharge curve of SVOF (D/50, D/10 and D).

To evaluate the difference between the discharge curve and the Open Circuit Potential (OCP) of SVOF, Galvanostatic Intermittent Titration Technique (G.I.T.T.) measurements were performed. For this, a cathodic current corresponding to an insertion rate of D/10 was applied for 2 hours. This step was followed by a relaxation period ($I = 0$) of 15 hours. Note the existence of a significant electrode polarization that increases from 275 mV to 550 mV during the uptake of the first four lithium equivalents followed by an abrupt decrease near $x = 3.80$ to values less than 50 mV (Figure 3.5). The significant polarization change that occurs near $x = 4$ suggests a relationship between the amount of lithium reacted and the four equivalents of silver based on the formula $\text{Ag}_4\text{V}_2\text{O}_6\text{F}_2$. Upon further Li insertion, two additional Li composition domains appear that differ by the amplitude of their polarization, which implies different reactivity mechanisms. The second domain has a significantly lower polarization between the fourth and sixth lithium inserted, followed by a third domain characterized by an increase in polarization.

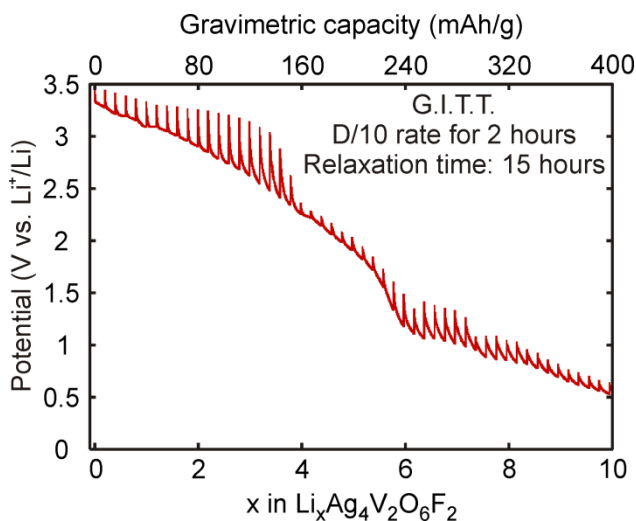


Figure 3.5a G.I.T.T. curve of SVOF/C_{sp} composite electrode in 1M LiPF₆ EC/DMC 1:1 electrolyte by applying a D/10 discharge rate for 2 hours followed by 15 hours relaxation time.

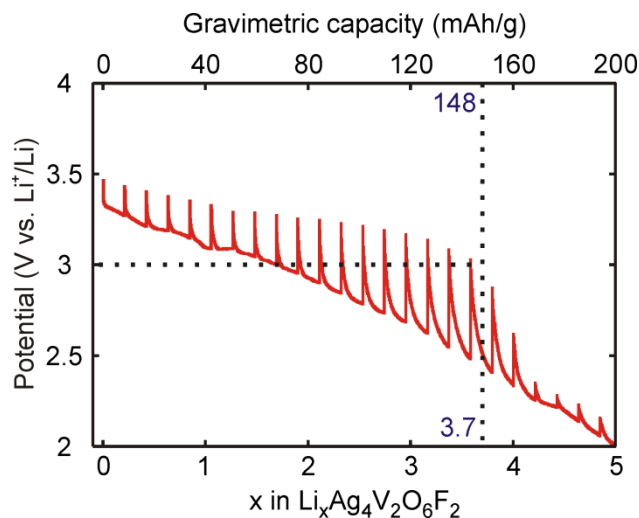


Figure 3.5b G.I.T.T. curve of SVOF/C_{sp} composite electrode in 1M LiPF₆ EC/DMC 1:1 electrolyte by applying a D/10 discharge rate for 2 hours followed by 15 hours relaxation time. A total of 3.7 Li (148 mAh/g) is inserted above a potential of 3 V.

3.4 Discussion

To understand the insertion mechanism that gives rise to these different phenomena, we embarked on an *in situ* X-ray diffraction study. These measurements revealed the structural evolution of SVOF during lithium insertion. Figure 3.6a gathers the diffractograms recorded each 0.09 Li⁺ inserted within the lithium composition range Li₀Ag₄V₂O₆F₂ - Li₁Ag₄V₂O₆F₂. At the early stage of the lithium insertion, the progressive appearance of two diffraction peaks centered at $2\theta = 38.16^\circ$ and $2\theta = 44.32^\circ$ is assigned to silver metal. No perceptible shift of the SVOF diffraction peaks was noted. However, simultaneously, one can also notice a slight intensity decrease and broadening of the peaks corresponding to the lithiated SVOF phase implying the onset of a structural amorphization or decrease in crystallinity (Figure 3.6b). Such effects (increase in the silver content peak and decrease in the Li_xSVOF main peaks) become more pronounced upon further lithiation ($1 \leq x \leq 4$ in Li_xAg₄V₂O₆F₂), such that by $x = 4$, a composite electrode consisting of well crystallized metallic silver coexists with an “X-ray”

amorphous matrix. The mismatch between the ionic radii of lithium ($r_{\text{Li}^+} = 0.76 \text{ \AA}$) and silver ($r_{\text{Ag}^+} = 1.15\text{-}1.35 \text{ \AA}$) and the atomic radius of silver ($r_{\text{Ag}} = 1.44 \text{ \AA}$) is most likely at the origin of these structural changes.²⁰

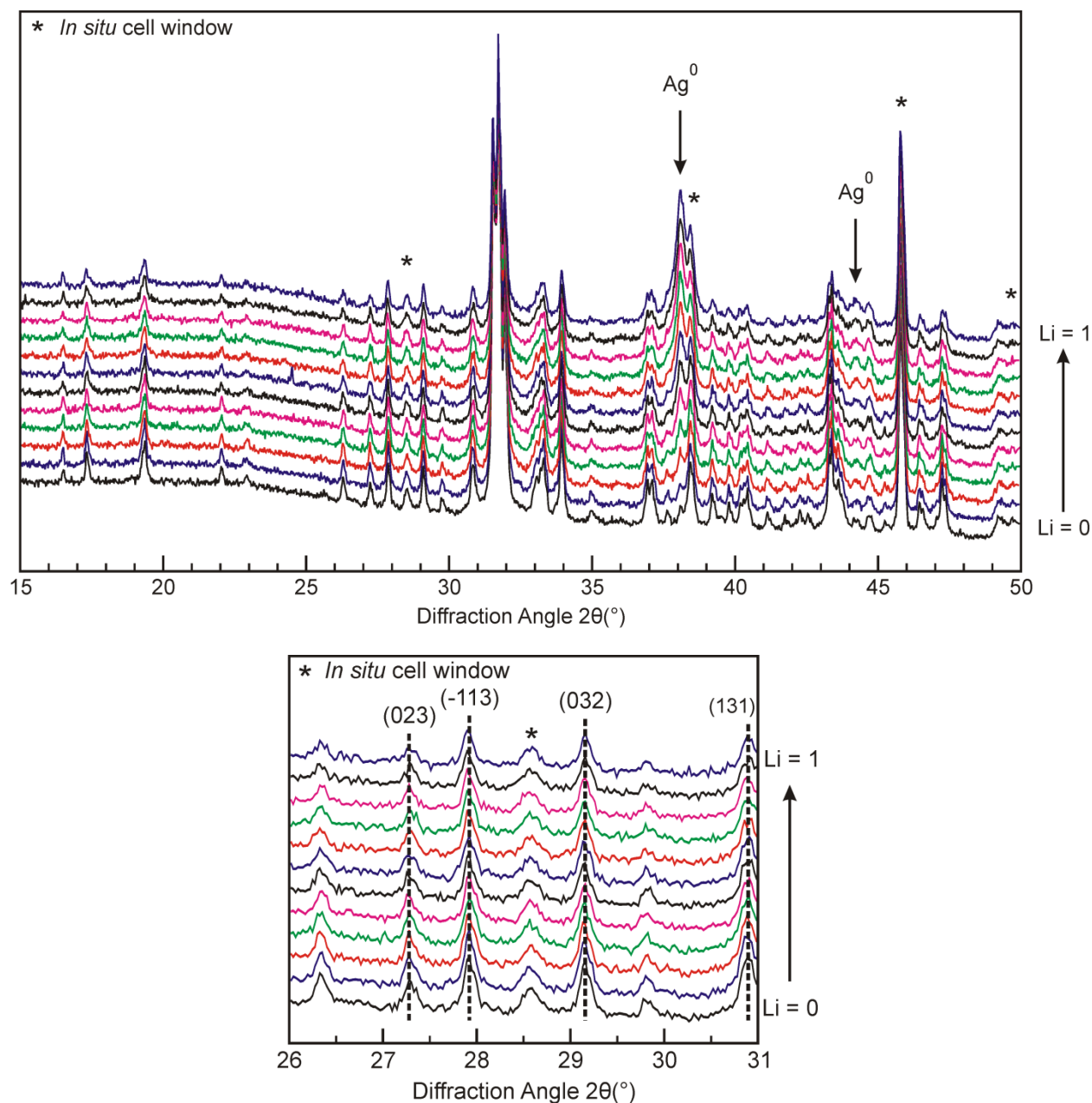


Figure 3.6 *In situ* evolution of the XRD pattern recorded every 0.09 Li^+ inserted at a D/10 discharge rate between $\text{Li}_0\text{Ag}_4\text{V}_2\text{O}_6\text{F}_2$ and $\text{Li}_1\text{Ag}_4\text{V}_2\text{O}_6\text{F}_2$ in a 2θ range of (a) 15-50° (b) 26-31°.

Further discharge, $4 \leq x \leq 7$ in $\text{Li}_x\text{Ag}_4\text{V}_2\text{O}_6\text{F}_2$, does not noticeably modify the amplitude of the Ag peak, but leads to a full and complete amorphization of the SVOF phase (Figure 3.7a). There is also the peculiar appearance and disappearance of two unidentified broad diffraction peaks at $2\theta = 21.32^\circ$ and 23.62° between the composition $\text{Li}_2\text{Ag}_4\text{V}_2\text{O}_6\text{F}_2$ and $\text{Li}_5\text{Ag}_4\text{V}_2\text{O}_6\text{F}_2$. Although their origin is not clear, we speculate that some structural correlation persists during the silver withdrawal. This feature is not reversible since we did not observe any phase recrystallization when recharging the cell. This experimental evidence demonstrates the irreversible character of the silver reduction, in contrast to the reported reversible copper extrusion mechanism in $\text{Cu}_{2.33}\text{V}_4\text{O}_{11}$.²¹ Finally, at more reductive potentials, an alloying reaction involving the silver metal, still in electronic contact with the composite electrode, and the lithium is observed. The formation of AgLi_x alloys was confirmed by XRD on the discharged SVOF with the occurrence of both AgLi and Ag_4Li_9 diffraction peaks while concurrently the two silver metal peaks practically vanished (Figure 3.7b). The reactivity of silver metal vs. lithium has been investigated by Taillades et al.,²² where both the reported diffraction evidence and the electrochemical signature at low potential (i.e. $< 1.5 \text{ V vs. Li}^+/\text{Li}^0$) support the alloying reaction between Ag and Li on fully discharged SVOF.

The decreasing intensity of the SVOF diffraction peaks together with the appearance of the silver metal was followed by integrating the diffraction peak area of the silver (111) reflection as a function of the lithium content (Figure 3.8). A linear relationship was observed between the loss of crystallinity of SVOF and amount of lithium inserted up to the point where the material becomes amorphous between $\text{Li}_3\text{Ag}_4\text{V}_2\text{O}_6\text{F}_2$ and $\text{Li}_4\text{Ag}_4\text{V}_2\text{O}_6\text{F}_2$. Interestingly, a non-linear variation in the appearance of silver metal was observed that reaches its maximum

near the composition $\text{Li}_4\text{Ag}_4\text{V}_2\text{O}_6\text{F}_2$. Such a deviation from linearity raised two hypotheses: (i) a competition between Ag^+/Li^+ displacement reaction and V^{5+} reduction and (ii) the nucleation of nano-crystalline silver metal particles not detected by XRD.

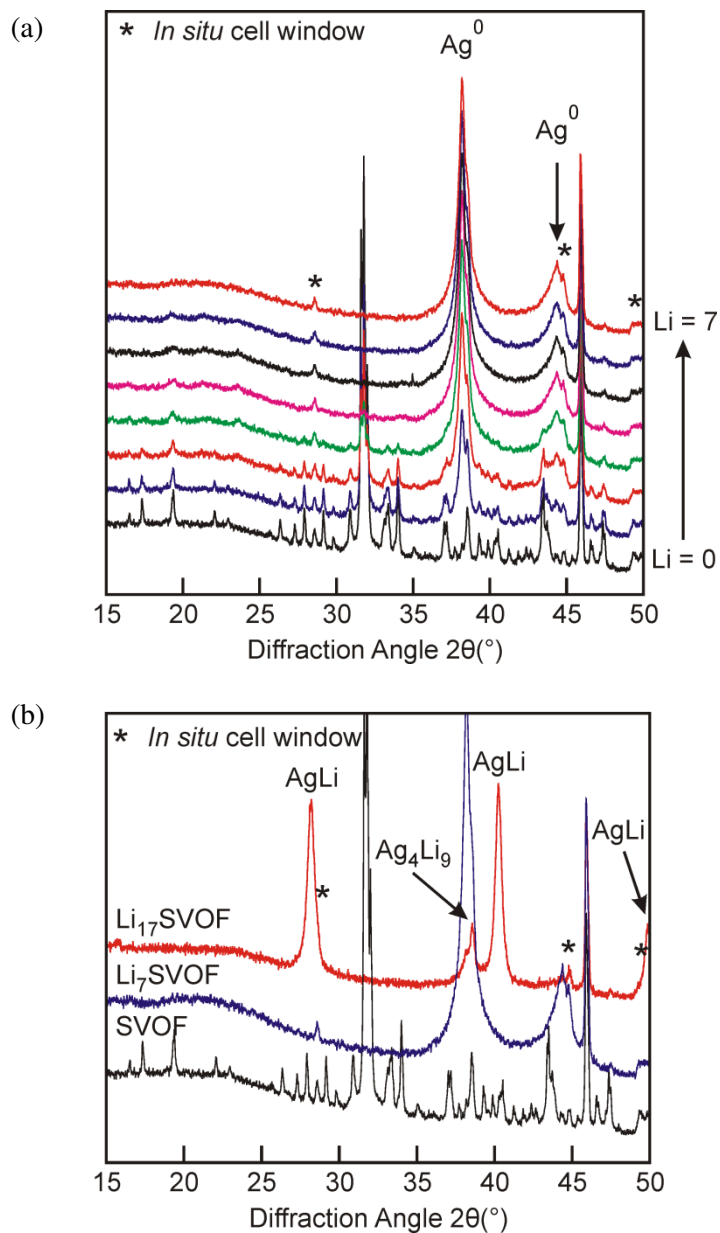


Figure 3.7 (a) *In situ* evolution of the XRD pattern recorded every 1 Li^+ inserted at a D/10 discharge rate between $\text{Li}_0\text{Ag}_4\text{V}_2\text{O}_6\text{F}_2$ and $\text{Li}_7\text{Ag}_4\text{V}_2\text{O}_6\text{F}_2$ in a 2θ range of $15\text{--}50^{\circ}$ (b) Comparison of the XRD patterns for SVOF , $\text{Li}_7\text{Ag}_4\text{V}_2\text{O}_6\text{F}_2$ and $\text{Li}_{17}\text{Ag}_4\text{V}_2\text{O}_6\text{F}_2$.

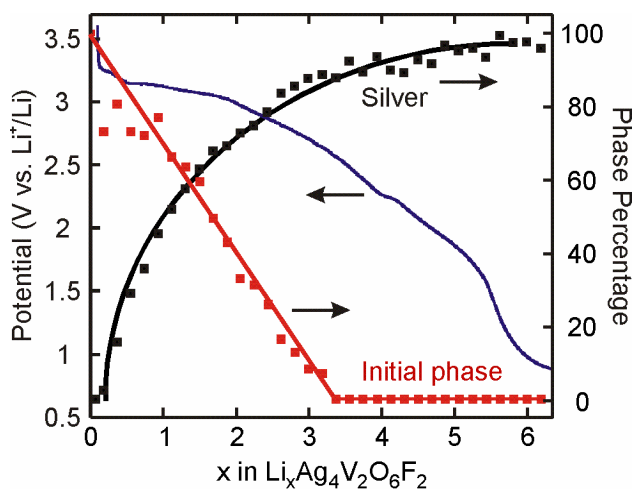


Figure 3.8 Evolution of the silver metal and SVOF XRD peak area as a function of x in $\text{Li}_x\text{Ag}_4\text{V}_2\text{O}_6\text{F}_2$.

To gain further insight into these subtle Li-driven electrochemical reactions and to address the first hypothesis via the appearance of a V^{4+} signal, EPR measurements were performed on several electrochemically lithiated SVOF compositions between $\text{Li}_0\text{Ag}_4\text{V}_2\text{O}_6\text{F}_2$ and $\text{Li}_6\text{Ag}_4\text{V}_2\text{O}_6\text{F}_2$. The spectra recorded at room temperature, displayed in Figure 3.9, clearly evidenced no V^{4+} formation through this composition range. In addition, no V^{4+} feature was found by measurements at 4 K. The starting material, i.e. $\text{Li}_0\text{Ag}_4\text{V}_2\text{O}_6\text{F}_2$, exhibits a very weak EPR signal that may be due to a small concentration of paramagnetic defects. All the spectra recorded by varying the Li^+ amount from 1 to 6 consisted of a narrow isotropic line of 13 G at a g value of 2.0021. Moreover we can clearly see that increasing the Li^+ inserted results in the increase of the of the EPR signal. Such a value of $g = 2.0021$, close to that of the free electron, has been reported related to the formation of Ag^0 nanoclusters and their surface conduction electrons.²³ Hence, the first 3.5 Li^+ reduce Ag^+ which allows us to rule out the first hypothesis. Furthermore, increasing the Li^+ amount to Li_6 does not appear to result in the formation of V^{4+} species, suggesting that the composition range 4 to 6 Li^+ corresponds to a selective redox

processes involving reduction of half of the V^{5+} in SVOF (redox couple V^{5+}/V^{3+}) rather than all the V^{5+} reduced to V^{4+} . This may reflect that the tetrahedral VO_4 groups in the isolated chains of alternation VO_4F_2 octahedra and VO_4 tetrahedra are difficult to reduce.²⁴ Although not common, a two electron reduction of an oxide cathode material has been observed.²⁵

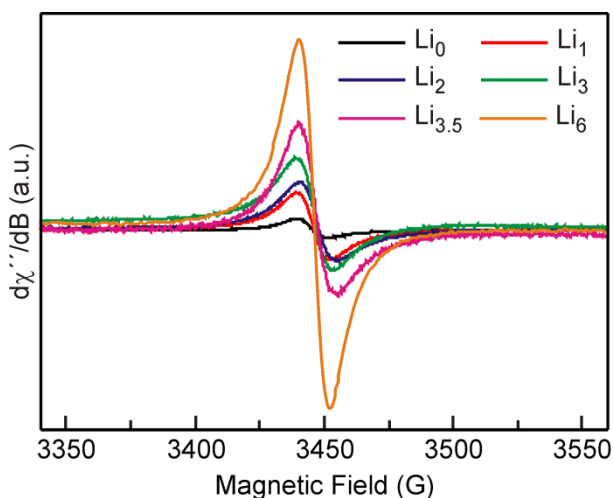


Figure 3.9 CW EPR spectra for $Li_xAg_4V_2O_6F_2$ for $x=0, 1, 2, 3, 3.5$ and 6 . The spectra were recorded at room temperature.

In order to have a better understanding of the nuclear environment of these Ag^0 nanoclusters, three-pulse ESEEM experiments were also performed on samples lithiated to $Li = 1$ and 3.5 . The spectra, Figure 3.10, were recorded using a τ value of 136 ns which minimizes the “blind spots” effect. These show for 1 Li^+ insertion two peaks arising from the ^{51}V nuclear Larmor frequency detected at 3.9 MHz and the 7Li nuclear frequency at 5.8 MHz. Increasing the Li^+ content from 1 to 3.5 results in a decrease of the ^{51}V peak and an increase of the 7Li peak, which appears to indicate the conduction electrons on silver are located closer to the lithium than the vanadium. For a value of $Li^+ = 6$ no pulsed EPR spectra can be measured at low temperature. Because the sample at 6 Li^+ is diamagnetic at low temperature, no spin echo can be recorded.

Thus, we recorded a series of CW EPR spectra in the temperature range 4-45 K and found that the $g \approx 2$ signal decreased with decreasing temperature. This phenomenon comes from the J coupling constant owing to the exchange interaction mechanism between coupled electronic spins. At low temperature a populated diamagnetic $S = 0$ indicates an antiferromagnetic coupling between conduction electrons associated with the silver particles. Figure 3.11 shows the temperature behavior for the $\text{Li}^+ = 6$ sample. Plotting the product of the signal intensity and the temperature versus temperature, the J coupling constant can be fit according to the Bleaney-Bowers equation.²⁶ A J value of -4.2 cm^{-1} provides a satisfactory fit of the curve.

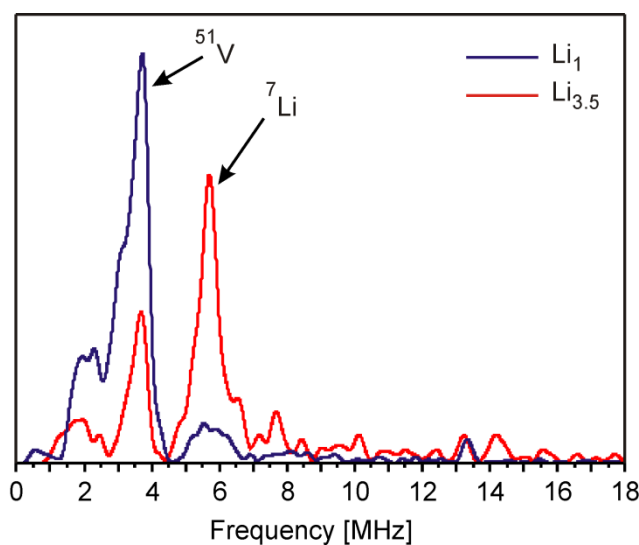


Figure 3.10 Three-pulse ESEEM spectra recorded at 4K for $\text{Li}_1\text{Ag}_4\text{V}_2\text{O}_6\text{F}_2$ and $\text{Li}_{3.5}\text{Ag}_4\text{V}_2\text{O}_6\text{F}_2$.

In light of the combined results provided by the *in situ* XRD investigation and the EPR, the three different domains pointed out by the G.I.T.T. curve can be described by the sequence of (i) the silver displacement reaction with lithium (ii) half of V^{5+} reduction to V^{3+} and (iii) complete reduction to V^{3+} and the eventual formation of Ag/Li alloy. Therefore, the significant drop in polarization observed around the fourth lithium inserted is due to a change from the

Ag^+/Li^+ displacement reaction to an insertion redox reaction involving the reduction of the V^{5+} and the insertion of lithium ion into the structure.

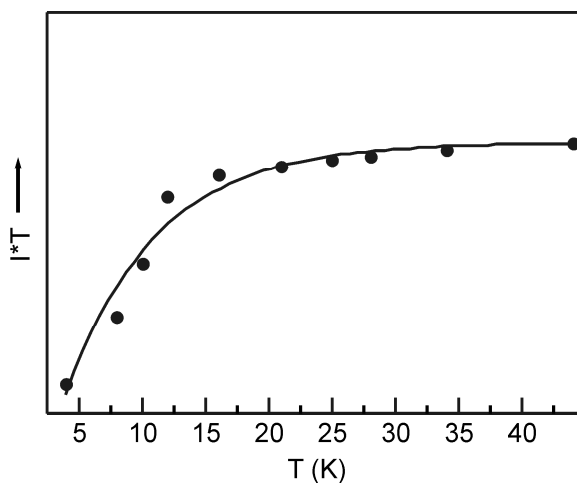


Figure 3.11 Plot of EPR intensity signal * temperature product (IT) versus temperature for $\text{Li}_6\text{Ag}_4\text{V}_2\text{O}_6\text{F}_2$ compound. The data was fitted according to the Bleaney-Bowers equation.

To investigate the second hypothesis, HRTEM was used to study the morphology of the formed silver metal on a sample that was electrochemically discharged at D/10 to 1.5 V. The bright-field images show the occurrence of two contrasts within the particles (Figure 3.12a). EDS and TEM measurements carried out on these two areas revealed the coexistence of silver metal (dark zone) within a matrix of composition $\text{Ag}_{0.12}\text{-Li}_x\text{-V}_2\text{-O}_y\text{-F}_z$ (Li_xSVOF). The small amount of unreduced silver in the Li_xSVOF matrix is consistent with the change in the GITT curve at $x = 3.8$ assigned to the end of the silver reduction. The unreduced silver could be isolated in the collapsed Li_xSVOF matrix and therefore very difficult to access for reduction. This explanation may also account for the continuous increase of polarization between $x = 0$ to $x = 3.8$.

In addition to the formation of silver between the $\text{Li}_x\text{-SVOF}$ layers in the form of long submicron wide dendrites and particle exfoliation (Figure 3.12a, inset), the second morphology consists of silver metal nanoparticles of about 3-5 nm diameter within the Li_xSVOF matrix (Figure 3.12b). The observation of nanosized silver metal particles accounts for the discrepancy observed in the Bragg peak intensities in Figure 3.8 and also accounts for the broad silver diffraction peaks. The formation of two different silver morphologies may have their origin in the surfaces created during the grinding of the as prepared SVOF crystallites. However, the coexistence of silver nanoparticles and silver dendrites also results from the influence of the discharge rate. Additional HRTEM investigations were performed on SVOF samples that were separately discharged at rates of D and D/50 to the same cut-off potential. Although both silver morphologies were still observed, the faster discharge rate surprisingly promotes the formation of silver dendrites. A similar relationship was reported for copper extrusion from the thiospinel CuCr_2S_4 .²⁷ To account for this observation, we consider that the nano-sized silver particles could originate from different pathways made favorable because of the low rate.

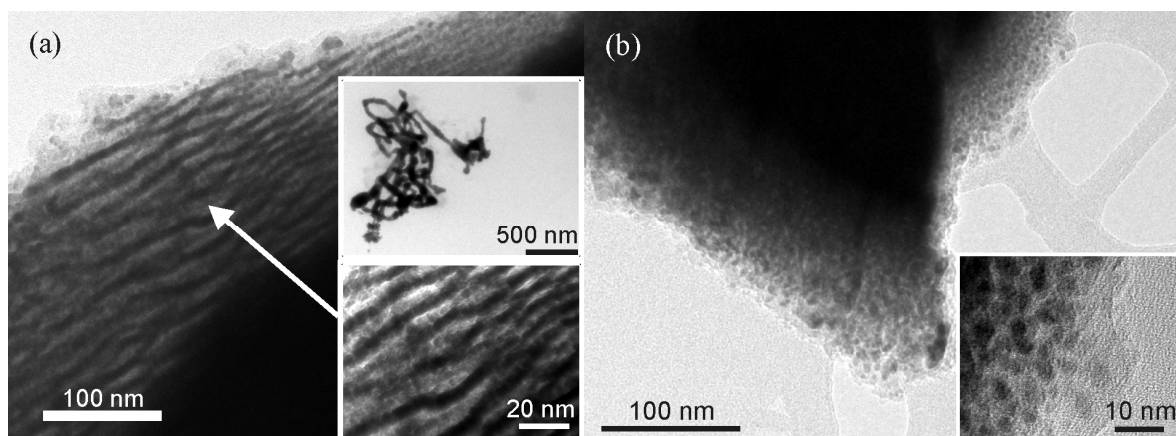


Figure 3.12 High Resolution Transmission Electron Microscopy bright field image obtained on an electrochemically discharged SVOF showing (a) the particle exfoliation with silver dendrites (b) the silver nanoparticles embedded in the amorphous Li_xSVOF matrix.

3.5 Conclusions

Additional galvanostatic and GITT electrochemical investigations have increased our understanding of the reactivity of $\text{Ag}_4\text{V}_2\text{O}_6\text{F}_2$ (SVOF) vs. lithium. *In situ* XRD measurements combined with EPR investigations suggest that a Ag^+/Li^+ displacement reaction occurs from $\text{Li}_0\text{Ag}_4\text{V}_2\text{O}_6\text{F}_2$ to $\text{Li}_{\sim 4.0}\text{Ag}_4\text{V}_2\text{O}_6\text{F}_2$. This reduction is accompanied by (i) significant electrode polarization underscoring the difficulties of silver withdrawal and (ii) continuous structure amorphization. This silver extrusion was found to be almost entirely irreversible. The metallic silver that forms exhibits two distinct morphologies: long dendrites with particle exfoliation and nanosized particles embedded in a Li_xSVOF matrix. As deduced by different EDS experiments, the amorphous matrix contains a small percentage of unreduced silver ions leading to an average composition $\text{Ag}_{0.12}\text{Li}_x\text{V}_4\text{O}_y\text{F}_z$. Following the silver displacement, a decrease in the cathode polarization is observed. This decrease is linked to a reversible vanadium redox of the V^{5+} to V^{3+} present in the amorphous matrix. In order to minimize the polarization for high-rate Ag-based electrodes, an engineered approach that decreases the length scale for ion diffusion by combining design of particle size and microstructure is under study.

Chapter Four

Ag₃VO₂F₄: Discovery and Characterization

4.1 Introduction

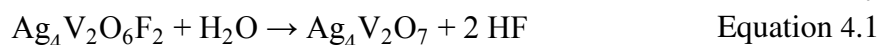
Silver vanadium oxide ($\text{Ag}_2\text{V}_4\text{O}_{11}$, SVO) is used commercially as a cathode material in primary lithium batteries for implantable cardioverter defibrillators (ICDs). SVO has a high capacity of 315 mAh/g, of which 100mAh/g is above 3 V, where ICDs work most efficiently. An ongoing goal of the medical battery community is to increase the useful capacity of battery materials, which arises from the reduction of silver. One apparent way is to increase the Ag:V ratio in the active material. However, it was reported that cathodes with AgVO_3 mixed with $\text{Ag}_2\text{V}_4\text{O}_{11}$ did not perform as well as those with only $\text{Ag}_2\text{V}_4\text{O}_{11}$. While the silver vanadates $\text{Ag}_4\text{V}_2\text{O}_7$ and Ag_3VO_4 also have a higher silver content, no reports of electrochemical characterization exist.

Recently, Sorensen *et al.* reported the new silver vanadium oxide fluoride $\text{Ag}_4\text{V}_2\text{O}_6\text{F}_2$ (SVOF).¹ Owing to the increased silver content, this new phase had a higher capacity of 148 mAh/g above 3 V, and the inclusion of the more electronegative fluoride anion in the coordination sphere of silver increased the initially delivered potential to 3.52 V, nearly 300 mV greater than SVO. In addition, an important attribute of SVOF was its chemical/electrochemical stability which allows the cell to discharge at the high potential.

Further investigation into the $\text{Ag}_2\text{O}-\text{V}_2\text{O}_5-\text{HF}_{(\text{aq})}$ system under hydrothermal conditions revealed a rich chemistry producing silver vanadium oxides with Ag:V ratios ranging from 1:2 to 3:1, in addition to SVOF.² Noticeably absent from the list of products was another silver vanadium oxide fluoride phase. However, trends within the composition diagram, as outlined in Section 2.4, have led to the discovery of a new phase. The aforementioned composition space is complete for the given reaction conditions. The reason for this is that this new silver vanadium oxide fluoride was not stable enough to withstand the conditions in the autoclave. To target this

unknown phase that could show greater electrochemical activity than $\text{Ag}_4\text{V}_2\text{O}_6\text{F}_2$, we wanted to incorporate a large amount of silver and fluoride. Firstly, it was known that an excess of silver was needed to (i) form phases with a silver to vanadium ratio greater than 1, and (ii) compensate for the higher relative solubility of silver versus vanadium. Secondly, the amount of HF also can affect the product formed in that more HF essentially lowers the amount of silver that remains in solution and thus out of the product, but would likely lead to a higher fluoridated phase. These two parameters were manipulated from the previous study in chapter 2, and eventually led to a new phase.

The discovery of the compound with a formula of $\text{Ag}_3\text{VO}_2\text{F}_4$ was from the realization of hydrolysis of the only known silver vanadium oxide fluoride phase. As elaborated in chapter two, $\text{Ag}_4\text{V}_2\text{O}_6\text{F}_2$ hydrolyzes into $\text{Ag}_4\text{V}_2\text{O}_7$ according to Equation 4.1. What was conjectured was that while $\text{Ag}_4\text{V}_2\text{O}_6\text{F}_2$ hydrolyzes into $\text{Ag}_4\text{V}_2\text{O}_7$, then perhaps some compound X hydrolyze into $\text{Ag}_4\text{V}_2\text{O}_6\text{F}_2$ (Equation 4.2) or into a silver vanadium oxide (Equation 4.3-4.4). While X may not follow one of the three theoretical reactions, it is clear that it must have a fluoride content greater than the potential product and hence the system to form X should have a higher fluoride concentration than for presently known reactions (i.e. a reaction that targets AgVO_3 , like one in chapter two, needs to have more fluoride in the system to make a compound X). Furthermore, if these equations were treated as equilibria, lower water content in the system should also favor X. While the former suggestion may be achieved by including fluoride salts as the reagents, the latter suggestion was more easily implemented by lowering the amount of water involved with the reaction, as described here.



The hydrothermal conditions used to find *X* are described in section 1.2. However, the key points to remember are as follows. The FEP Teflon pouch with the reactants is placed into a 125 mL PTFE Teflon liner for a Parr autoclave, which is then backfilled with 42 mL of H₂O. One property of the pouches is that they are semi-permeable at reaction temperatures and allow water to diffuse. What is observed for these reactions is water from the backfill enters the pouch, as determined by the mass of the pouch before and after the reaction. By limiting the amount of water that diffuses into the pouch, perhaps Equations 3.2-3.4 could be either driven to the left or not driven toward completion, thus resulting in a new compound *X*. To achieve this, two methods were investigated. Firstly, multiple diffusion layers were utilized by loading reactions into a pouch within a pouch and perhaps then again within a pouch, effectively achieving two and three layers of the FEP material, respectively. Secondly, reactions at temperatures lower than those which allow diffusion, such as at 100 °C, should also lead to complete reactions without the addition of water.

4.2 Synthesis and Characterization

4.2.1 Materials

Caution. Hydrofluoric acid is toxic and corrosive and must be handled with extreme caution and the appropriate protective gear! If contact with the liquid or vapor occurs, proper treatment procedures should be followed immediately.³⁻⁵

Materials. Ag_2O (99.9%, Fisher), V_2O_5 (99.6%, Alfa-Aesar), and aqueous hydrofluoric acid (48-50% HF by weight, Fisher) were used as received.

4.2.2 Synthesis

The new silver vanadium oxide fluoride $\text{Ag}_3\text{VO}_2\text{F}_4$ was synthesized from a reaction of 0.3977 g (1.716×10^{-3} mol) of Ag_2O , 0.0779 g (4.28×10^{-4} mol) of V_2O_5 , and 0.2555 g of $\text{HF}_{(\text{aq})}$ (6.260×10^{-3} mol HF) in a heat sealed Teflon [fluoro(ethylene-propylene)] pouch.⁶ The reaction pouch was then subject to three different reaction schemes. First, a reaction in a single pouch was placed in a water bath which was then brought to a boil. The bath was held at 100 °C for between 2 and 24 hours. For the shorter time periods, water was added to the bath to replace what had boiled away, and for longer time periods, a simple reflux system with a round bottom flask and water-cooled condenser was used. The pouch was opened in air and the contents were vacuum filtered to retrieve bright red polycrystalline $\text{Ag}_3\text{VO}_2\text{F}_4$, from which a single crystal was picked out for structural X-ray diffraction studies. For the second reaction scheme at higher temperatures, the effect of multiple pouches was investigated by placing the reaction pouch into another pouch. Also investigated was the effect of a pouch within a pouch within a pouch. The double or triple pouch was then placed into a 125 mL, poly(tetrafluoroethylene) (PTFE) Teflon lined Parr autoclave which was backfilled with 42 mL of deionized H_2O . The autoclave was heated at 150 °C for 24 hr. and cooled at a rate of 6 °C / hr. Again, the pouch was opened and products filtered to recover $\text{Ag}_3\text{VO}_2\text{F}_4$.

Eventually, it was realized that the necessary reaction proceeded before being subjected to the above two reaction schema. Hence, a third set of conditions consisted of assembling the reaction pouch and leaving it at room temperature. This technique, however, does not lead to the

growth of any crystals large enough for single crystal X-ray diffraction. A fourth technique to consistently recover single crystals, will be described in chapter 5.

4.2.3 Characterization

Crystallographic Determination. The selected crystal exhibited dimensions of 0.11 x 0.20 x 0.28 mm and was collected at 100 K with Mo-K α radiation on a Bruker AXS Kappa Apex II CCD diffractometer. Reflections were integrated with the SAINT module within the APEX2 suite.⁷ Examination of the diffraction patterns of the single crystals of Ag₃VO₂F₄ showed evidence of partial merohedral twinning. However, the predominance of one component helped to determine the basic unit cell with the twin law with the program CELL_NOW. The structure of Ag₃VO₂F₄ was solved by direct methods in SHELX, using a “detwinned” reflection file prepared by TWINABS from the intensities of the first domain (HKLF 4).⁸ This first solution had a space group of P2₁/n with R1 = 0.0730, wR2 = 0.2753, mean V—O/F distance of 1.855 Å and a first residue of 11.41 e[−]Å^{−3} at 0.30 Å of V. The vanadium atom was then allowed to move away from its center of symmetry with a fixed occupation ratio of 0.5. The two V center are separated by 0.455(2) Å in an equatorial plane compared to its environment. The observation of the V—O/F distances in this plane shows indeed two V—O short distances of 1.675(2) and 1.707(2) Å with *trans* V—F distances of 2.001(2) Å and 2.025(2) Å. These ligand sites in the plane are statistically occupied by 0.5 oxide and 0.5 fluoride, with their atomic parameters (atomic coordinates and anisotropic atomic displacement parameters) being constrained to the same values. The two remaining ligands correspond to fluoride with intermediate bond distances of 1.866(2) Å and 1.887(2) Å from both V positions. This solution provided a satisfactory model with values of R1 = 0.0568 and wR2 = 0.2223. Further refinement could be done around the Ag1 site. Two residues of 7.55 and 5.86 e[−]Å^{−3} were observed at 0.41 Å and 0.49 Å from Ag1,

respectively, and then introduced in the model; the sum of the three sites being constrained to unity. The final refinement, using the HKLF 5 option for more accurate solution and the determination of the twin domain ratios, includes anisotropic displacement parameters and further correction from secondary extinction effects, giving $R1 = 0.0403$ and $wR2 = 0.1194$ with negligible electron residue. The occupancies of the Ag1 sites are split according to the ratios 0.66(2):0.26(2):0.08(2) and the twin ratios from domain I to VI are $tI = 0.5142(3)$, $tII = 0.006(2)$, $tIII = 0.0145(5)$, $tIV = 0.399(3)$, $tV = 0.0138(5)$, $tVI = 0.0525(2)$. See Table 4.1 for crystallographic data and Table 4.2 for selected atomic coordinates.

Powder X-ray Diffraction. Powder X-ray diffraction patterns were collected on a Rigaku XDS 2000 with Ni filtered Cu $K\alpha$ radiation ($\lambda = 1.5418 \text{ \AA}$) and compared with patterns recorded in the JCPDS (Joint Committee of Powder Diffraction Standards) database.

Electrochemical Characterization. In a dry room, to prevent hydrolyzation of the oxide fluoride, a sample of $Ag_3VO_2F_4$ was finely ground and then mixed with 10 wt % acetylene black and 10 wt % polyvinylidenedifluoride (PVDF) binder. This electrode mixture was then laminated onto aluminum foil and dried at 75°C for 1 h in an oven under air in the dry room. Electrochemical button cells were assembled in an argon-filled glovebox using lithium foil as the negative electrode. The electrodes were separated by a Celgard separator, and a 1 M $LiPF_6$ in a 1:1 by weight mixture of ethylene carbonate (EC)/diethyl carbonate (DEC) solution was used as the electrolyte. Cells were discharged using either a 0.001 mA constant current on a MacPile II galvanostat/potentiostat or by stepping in 0.05 V increments using a 0.1 mA current with 6 h rests between voltage steps on a Maccor galvanostat.

Table 4.1 Crystallographic Data for $\text{Ag}_3\text{VO}_2\text{F}_4$

formula	$\text{Ag}_3\text{VO}_2\text{F}_4$
fw	482.5
space group	$\text{P2}_1/\text{n}$ (No. 14)
a (Å)	5.7568(2)
b (Å)	5.7811(2)
c (Å)	8.0883(18)
β (deg)	90.6610(15)
V (Å ³)	269.166(17)
Z	2
T (°C)	−120(2)
λ (Å)	0.71073
ρ_{calc} (g/cm ³)	5.954
μ (mm ^{−1})	12.447
$R(F)^a$	0.0403
$wR_2(F^2)^b$	0.1194

$$^a R = \sum ||F_o| - |F_c|| / \sum |F_o|$$

$$^b wR_2 = [\sum w(F_o^2 - F_c^2)^2 / \sum w(F_o^2)^2]^{1/2}$$

Table 4.2 Selected Atomic Coordinates for $\text{Ag}_3\text{VO}_2\text{F}_4$

atom	site	x	y	z	$U(eq),^a \text{Å}^2$	Occupancy
Ag1a	4e	0.0003 (6)	0.4524 (6)	0.2638 (4)	0.0173 (3)	0.63 (2)
Ag1b	4e	−0.0283 (15)	0.4409 (10)	0.2480 (7)	0.0149 (6)	0.30 (2)
Ag1c	4e	0.020 (2)	0.484 (3)	0.238 (3)	0.0166 (12)	0.077 (16)
Ag2	2b	0.0000	0.0000	0.5000	0.01592 (7)	1
V1a	2a	−0.01606 (18)	0.0195 (2)	0.02158 (14)	0.01500 (14)	0.50
V1b	2a	0.01606 (18)	−0.0195 (2)	−0.02158 (14)	0.01500 (14)	0.50
F1	4e	0.1014 (4)	0.0365 (4)	0.2158 (2)	0.0212 (3)	0.50
O1	4e	0.1014 (4)	0.0365 (4)	0.2158 (2)	0.0212 (3)	0.50
F2	4e	−0.2649 (4)	0.1633 (4)	0.0512 (3)	0.0210 (4)	0.50
O2	4e	−0.2649 (4)	0.1633 (4)	0.0512 (3)	0.0210 (4)	0.50
F3	4e	0.1476 (4)	0.2750 (3)	−0.0569 (3)	0.0232 (4)	1

^a $U(eq)$ is defined as one-third of the trace of the orthogonalized U_{ij} tensor.

4.3 Results

4.3.1 Synthesis

Phase pure $\text{Ag}_3\text{VO}_2\text{F}_4$ was formed from a variety of reaction conditions, as listed above. In actuality, only one reaction scheme was needed to form this phase and the other reaction descriptions were merely treatments of the material. In all three methods, $\text{HF}_{(\text{aq})}$ was added to a 4:1 mole ratio mixture of Ag_2O and V_2O_5 . This exothermic reaction quickly produced the bright red $\text{Ag}_3\text{VO}_2\text{F}_4$ phase from the black and orange precursors. This system was then exposed to

different heating conditions mentioned above. Hydrothermally treating the reaction at 150 °C yielded some crystals large enough for single crystal X-ray diffraction. Product from reactions placed into the boiling water bath and from reactions at room temperature did not yield large enough crystals.

However, another difference was noted for the products recovered from reactions heated at 150 °C versus 100 °C and between short and long reaction times. The longer the duration that $\text{Ag}_3\text{VO}_2\text{F}_4$ was heated, the more resistant it was to hydrolysis from moisture in the air. The change in the product can easily be monitored by a change in color and subsequently powder X-ray diffraction patterns. Figure 4.1 shows a very pure sample of $\text{Ag}_3\text{VO}_2\text{F}_4$ from a reaction that was boiled for 24 hours (labeled “reflux 24 hours”) and a sample that was reacted at 100 °C for an hour (initial diffractogram labeled “boil fresh”). The latter sample was left on the diffraction slide on the bench top and patterns were recorded at later times (after 1, 3, and 52 hours). These patterns are compared to the Joint Committee on Powder Diffraction Standards (JCPDS) Powder Diffraction File (PDF) for Ag_3VO_4 (bottom of figure) and $\text{Ag}_4\text{V}_2\text{O}_6\text{F}_2$ synthesized from hydrothermal conditions (top of figure). Following the dashed red lines, representing a characteristic peak in each of the three phases, one can easily observe the evolution of Ag_3VO_4 and $\text{Ag}_4\text{V}_2\text{O}_6\text{F}_2$ from $\text{Ag}_3\text{VO}_2\text{F}_4$. While this phase hydrolyzes noticeably over the course of a few hours, product from room temperature reactions and reactions for less time were more reactive, perhaps owing to the lesser degree of crystallinity, where the more crystalline material is slower to hydrolyze. The stability of more highly crystallized $\text{Ag}_3\text{VO}_2\text{F}_4$ is discussed in chapter 5.

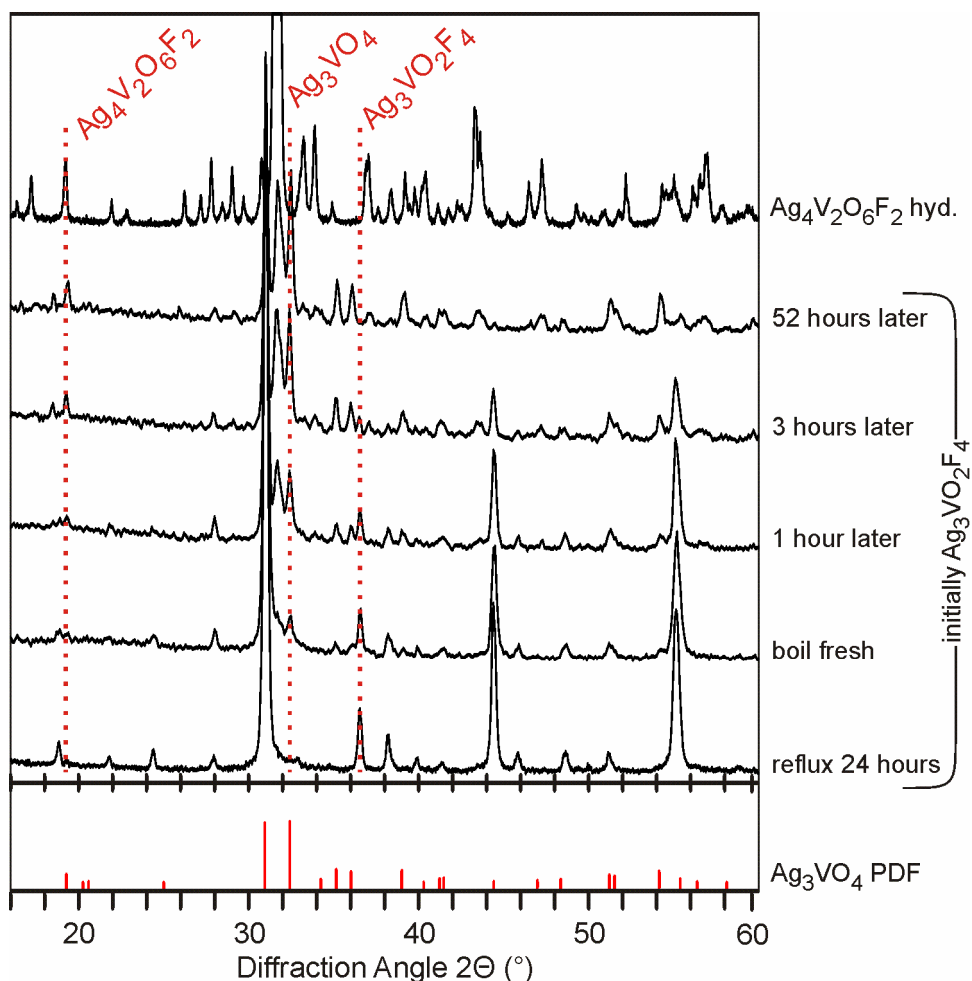


Figure 4.1 Powder X-ray diffraction patterns showing the decomposition of $\text{Ag}_3\text{VO}_2\text{F}_4$ into Ag_3VO_4 and $\text{Ag}_4\text{V}_2\text{O}_6\text{F}_2$ over 52 hours (from the sample labeled “boil fresh”). Also shown is the increased purity and stability of $\text{Ag}_3\text{VO}_2\text{F}_4$ from a reaction at 100 °C for 24 hours.

4.3.2 Structural Description

The structure of $\text{Ag}_3\text{VO}_2\text{F}_4$ is a cryolite-type structure, which is homotypic to that of a perovskite structure of the formula ABO_3 (Figure 4.2). The B-site cations sit at the center of corner sharing octahedra in all three dimensions. The A-site cations are 10-coordinate within the spaces between octahedral faces. The formula $\text{Ag}_3\text{VO}_2\text{F}_4$ could be written as $(\text{Ag}_2)(\text{AgV})\text{O}_2\text{F}_4$ to show that silver occupies the A-site positions and the B-site cations are 50% Ag and 50% V. In fact, the B-site cations are ordered, alternating between silver- and vanadium-centered octahedral

in all directions (as is characteristic of cryolite-type compounds). The oxide and fluoride positions, which cannot be differentiated by their X-ray scattering properties, must be determined by structural characteristics, such as through a distortion of a d^0 transition metal cation within an octahedra. In an octahedron with one, two, or three oxide ligands, the metal center will shift toward the corner, edge, or face with the oxide owing to the shorter covalent bond formed from the stronger $d\pi$ - $p\pi$ overlap with the oxide than with the fluoride (Figure 4.3).⁹ Examples of structural units that exhibit this behavior are $[\text{MOF}_5]^{n-}$ ($\text{M} = \text{V}^{5+}, \text{Nb}^{5+}, \text{Ta}^{5+}; n = 2$),¹⁰⁻¹³ $[\text{MO}_2\text{F}_4]^{n-}$ ($\text{M} = \text{V}^{5+}, n = 3; \text{M} = \text{Mo}^{6+}, \text{W}^{6+}, n = 2$),¹³⁻¹⁵ and $[\text{MO}_3\text{F}_3]^{n-}$ ($\text{M} = \text{Mo}^{6+}, n = 3$).^{16,17} Thus, the metal-oxide bond(s) should be the shortest, with the fluoride(s) *trans* to that oxide as the longest. In the initial structural solution of $\text{Ag}_3\text{VO}_2\text{F}_4$, the distance from the vanadium center to any ligand was $\sim 1.855 \text{ \AA}$, which shows no distortion and therefore no long-range oxide/fluoride ordering. However, as described above, a final refinement with the vanadium position equally split between two locations revealed short and long metal center-to-ligand distances. The two short bonds are *cis* to each other, thus giving vanadium-centered octahedra that can be represented by Figure 4.4.

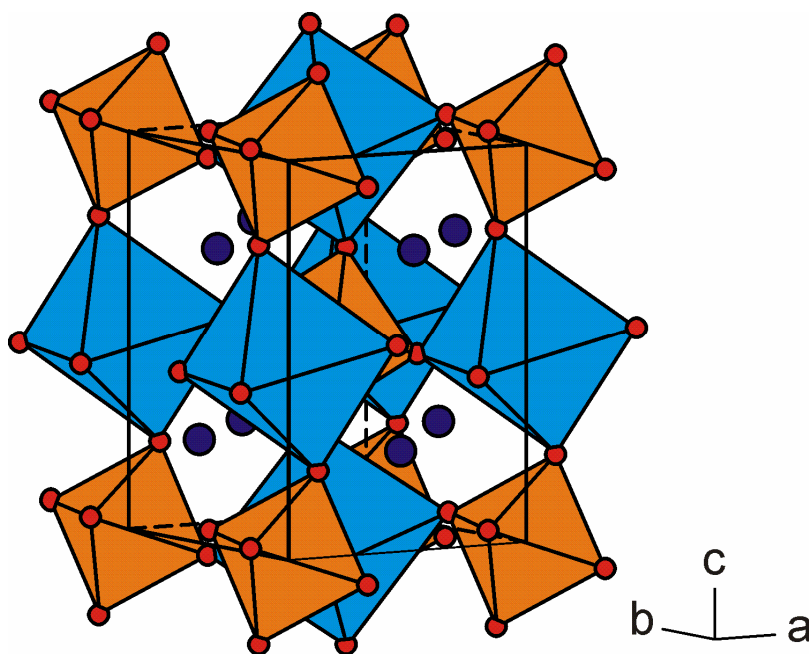


Figure 4.2 Cryolite unit cell of $\text{Ag}_3\text{VO}_2\text{F}_4$, similar to a perovskite structure, consisting of infinite corner sharing octahedra. Smaller, orange octahedra are vanadium-centered $[\text{VO}_{2/2}\text{F}_{4/2}]^+$, and larger blue octahedra are silver-centered $[\text{AgO}_{2/2}\text{F}_{4/2}]^{3-}$. Silver also resides in the A-site (dark blue) and is 10 coordinate. Red circles represent disordered oxide/fluoride anions.

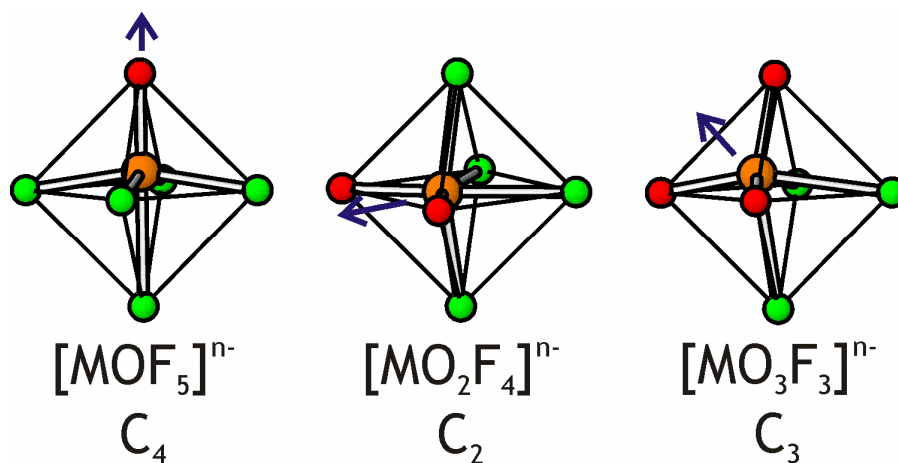


Figure 4.3 Examples of distortions of d^0 transition metals in an octahedral environment surrounded by oxide and fluoride ligands. Shorter, stronger metal-oxide bonds form and thus the central cation can distort toward a corner, edge, or face.

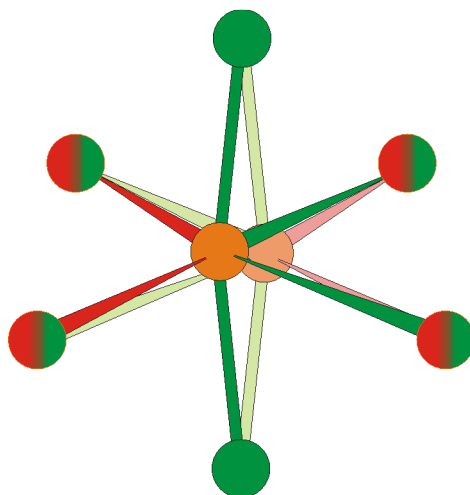


Figure 4.4 Depiction of the $\text{cis-VO}_2\text{F}_4^{3-}$ anion solved with a split-occupancy vanadium (orange) center. One vanadium position and the representative bonds are lighter in color to help differentiate between the two sets. V-O bonds are in red; V-F bonds are in green. The two defined fluoride positions are green, and the mixed oxide / fluoride positions are mixed red / green.

4.4 Discussion

4.4.1 Multiple Pouch Reactions

Hydrolysis of oxide fluoride compounds is widely observed, but also is not the expected norm as many oxide fluorides are stable in ambient conditions. In the efforts to find a new silver vanadium oxide fluoride phase two hydrolysis reactions were realized. First, hydrolysis of the already known $\text{Ag}_4\text{V}_2\text{O}_6\text{F}_2$ was more fully understood. While equation 4.1 was previously known to occur, further experiments between 150 °C and 200 °C show that both temperature and water were factors for its hydrolysis to $\text{Ag}_4\text{V}_2\text{O}_7$. Secondly, the hydrolysis of $\text{Ag}_3\text{VO}_2\text{F}_4$ to SVOF and Ag_3VO_4 was observed, where in the hypothetical equations 4.2 and 4.4, X would be $\text{Ag}_3\text{VO}_2\text{F}_4$. These results are expressed in Figure 4.5. In addition, the new reaction technique that utilizes a triple pouch allowed reactions to introduce a controlled amount of water into the reaction system to observe product hydrolysis.

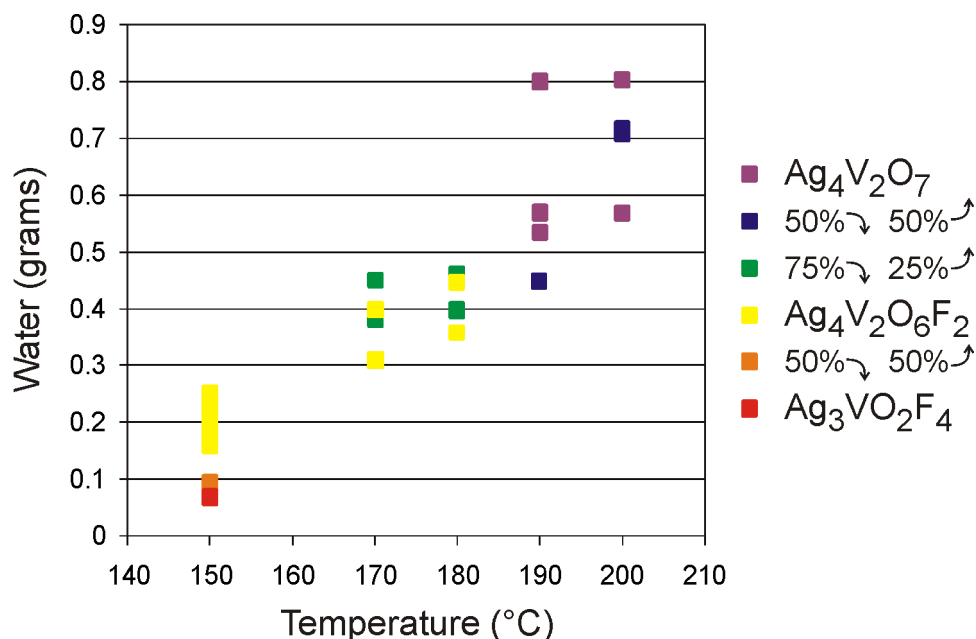


Figure 4.5 Plot of products recovered from reactions under hydrothermal conditions. Some reactions lead to phase pure product of $\text{Ag}_3\text{VO}_2\text{F}_4$, $\text{Ag}_4\text{V}_2\text{O}_6\text{F}_2$, or $\text{Ag}_4\text{V}_2\text{O}_7$ and others lead to a mixed product. Arrows next to the percentages point to the pure phase that belongs to that percent value.

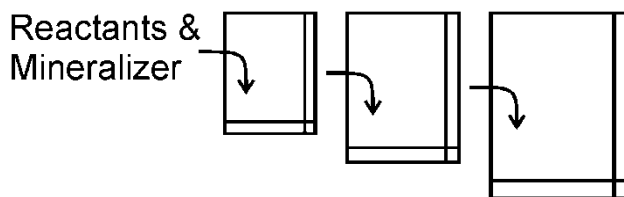


Figure 4.6 Reaction setup showing the triple pouch. Dimensions of the outermost pouch were identical to those for “typical” single-pouch reactions (1.75 in. x 3 in.) and the inner two pouches were cut to fit snugly in their respective outer pouch. The horizontal and vertical lines along the edges represent the heat-sealed seal.

A major breakthrough and realization through this work has been the utilization of multiple reaction pouches (Figure 4.6). It is known that the FEP pouches are semi-permeable to water at reaction temperatures. Reaction temperatures that have been explored in other systems were between 150 °C to 200 °C, the upper limit of which is close to the melting point of the material. Depending on the amount of reagents, or more specifically the mineralizer, and the temperature the amount of water that enters a single pouch can vary by over a magnitude (i.e.

less than 0.1 g to more than 1.0 g), but is consistent and repeatable for identical reactions and conditions. By placing a pouch within a pouch, two barriers of diffusion are between the reactants and the autoclave backfill. The second layer of diffusion separates the backfill from the mineralizer, and weakens the effect that the mineralizer has on drawing the backfill into the reaction. At 150 °C, a double pouch draws in ~0.15 g vs. 0.20 – 0.30 g for a single pouch, for reactions with reactant quantities described in 4.2.2. With a third pouch layer, the amount of water that diffuses can be reduced to under 0.05 g and $\text{Ag}_3\text{VO}_2\text{F}_4$ is formed.

However, temperature also affects the amount of diffusion, and the advantage of having multiple pouches is quickly lost as temperature is increased. At 200 °C, a single pouch will draw in ~0.80 g of water, and a triple pouch will draw in ~0.55 g of water. Even as low as 170 °C, a single pouch will draw in ~0.40 g of water vs. ~0.35 for a triple pouch. While these two variables are correlated, additional water can be added to the reaction pouch to study the results from high-water, low-temperature systems. As can be seen in Figure 4.5, the major phase shifts from $\text{Ag}_4\text{V}_2\text{O}_6\text{F}_2$ to $\text{Ag}_4\text{V}_2\text{O}_7$ as temperature and water are concurrently increased; and a mixed product was recovered between the two extremes. Percentages of mixed phases were estimated from relative intensities of powder X-ray diffraction peaks.

4.4.2 Electrochemistry

Since the electrochemical properties of $\text{Ag}_4\text{V}_2\text{O}_6\text{F}_2$ compare favorably to $\text{Ag}_2\text{V}_4\text{O}_{11}$, it was the goal to find a second silver vanadium oxide fluoride phase and evaluate its electrochemical activity. The improvements of $\text{Ag}_4\text{V}_2\text{O}_6\text{F}_2$ over $\text{Ag}_2\text{V}_4\text{O}_{11}$ as a cathode material are attributed to the increased silver density (greater capacity) and the incorporated fluoride (greater potential). Thus, $\text{Ag}_3\text{VO}_2\text{F}_4$, which has an even higher silver density and more fluoride content than $\text{Ag}_4\text{V}_2\text{O}_6\text{F}_2$, seemed highly promising as a cathode material.

The electrochemical testing was performed with a current controlled discharge stepping the voltage in 5 mV steps with 6 hour rests between steps (Figure 4.7). The tested cell discharged quickly to 2.3 V (vs. Li^+/Li^0) with an initial open circuit voltage of 3.11 V (probably > 3.3 V as made). After a small plateau, the battery slowly over time discharged to 0.92 V, giving a capacity of 151 mAh/g. Powder XRD of each electrode after discharge showed Ag at the cathode and Li and Ag at the anode. The presence of Ag at the anode and the fully discharged cells before the galvanostatic tests, described next, infer ion exchange with the electrolyte. In a second type of experiment, galvanostatic tests (using a constant current discharge) on other cells were attempted. All cells tested were fully discharged by the time the test was started, roughly 1 day after the cells were assembled. In fact, the cells maintained nearly a constant 0.34 V. This is attributed to lithiation of the aluminum current collector (~0.4 V). The nearly negligible performance of $\text{Ag}_3\text{VO}_2\text{F}_4$ as a cathode in a lithium battery could be owing to its structure. The lack of long range connectivity between vanadium oxide fluoride octahedra in the crystal structure of $\text{Ag}_3\text{VO}_2\text{F}_4$ allows silver to readily leave the structure before a load is put across the battery. In contrast, the vanadium oxide fluoride chains in $\text{Ag}_4\text{V}_2\text{O}_6\text{F}_2$ maintain a framework structure during silver reduction, similar to the vanadium oxide layers in $\text{Ag}_2\text{V}_4\text{O}_{11}$, which is robust enough to withstand ion exchange with the electrolyte. For comparison of $\text{Ag}_3\text{VO}_2\text{F}_4$ to SVOF, Figure 4.8 shows the reduction of SVOF under the same current controlled discharge test conditions as described above.

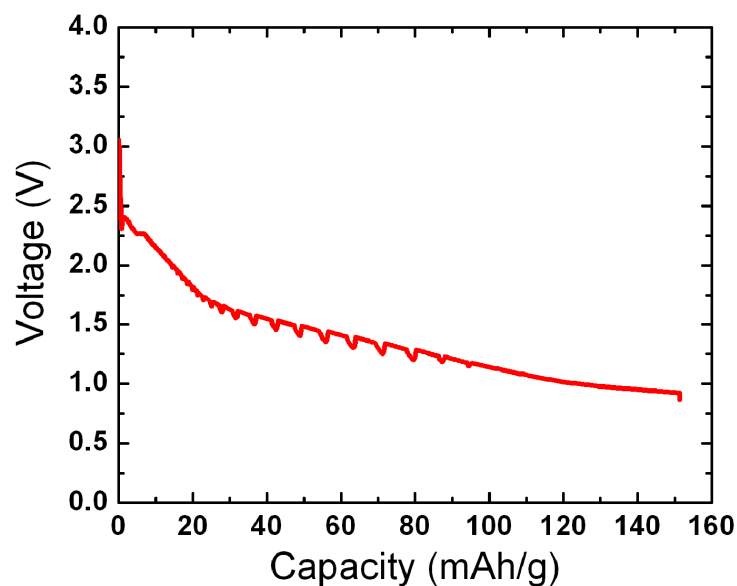


Figure 4.7 Voltage vs. capacity for $\text{Ag}_3\text{VO}_2\text{F}_4$ discharged in 5 mV steps followed by a relaxation time of 6 hours.

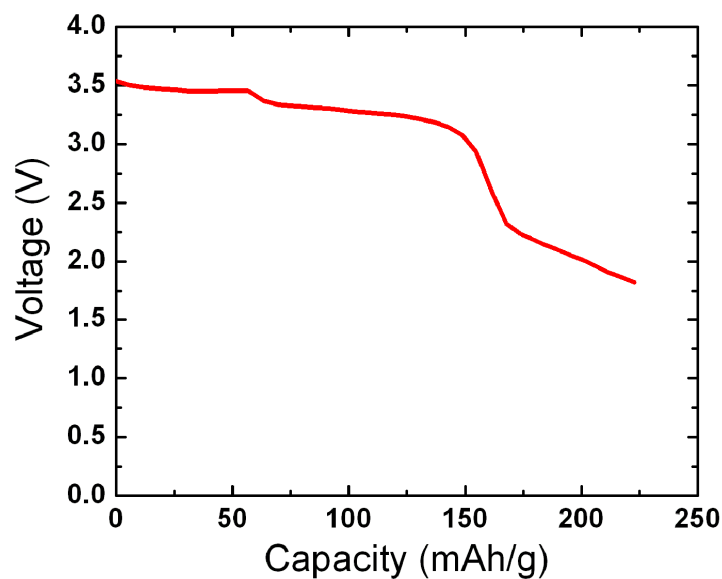


Figure 4.8 Voltage vs. capacity for $\text{Ag}_4\text{V}_2\text{O}_6\text{F}_2$ discharged in 5 mV steps followed by a relaxation time of 6 hours.

4.5 Conclusions

A new silver vanadium oxide fluoride phase $\text{Ag}_3\text{VO}_2\text{F}_4$ with the cryolite-type structure was discovered in the Ag_2O - V_2O_5 - $\text{HF}_{(\text{aq})}$ system. Imperative to the formation of this phase was

the exclusion of water that knowingly was included in the investigation of the same system under hydrothermal conditions. Also observed was that this phase was formed from the onset when hydrofluoric acid was added to the silver and vanadium oxides. While the exclusion of water and room temperature synthesis were exciting, the electrochemical activity of $\text{Ag}_3\text{VO}_2\text{F}_4$, higher density of silver and increased fluoride content, was less that desirable.

Chapter Five
Reversibility of $\text{Ag}_3\text{VO}_2\text{F}_4$ Formation

5.1 Introduction

Generally taught in chemistry classes, and what is most often observed in chemistry labs, is an increased solubility of a solid solute in a solvent at higher temperatures. However, some compounds exhibit a negative temperature coefficient of solubility, where a compound precipitates upon heating and dissolves upon cooling. One such example of this is $\text{Ce}_2(\text{SO}_4)_3$ in water.¹ A saturated solution at room temperature (19.09 g / 100 g H_2O) will begin to precipitate crystals at 84 °C and more fully crystallize at 100 °C (0.78 g / 100g H_2O), only to dissolve upon cooling. This phenomenon can also be observed for the systems of LiOC_2H_5 in ethanol, calcium acetate in water, and AlPO_4 in phosphoric acid.²⁻⁴ A negative temperature coefficient of solubility not only can be observed in ionic compounds, but metal oxide materials as well. Fe_2O_3 in a basic aqueous solution with an elevated H_2 concentration can be less soluble at higher temperatures.⁵

In more general terms, the temperature change is responsible for changing the properties of the system from that of a soluble solute to an insoluble solute. This is reflected as a change in Gibbs free energy, $\Delta G = \Delta H - T\Delta S$, where ΔG is negative (favorable) for Equation 5.1 at low temperatures and positive (unfavorable) at high temperatures. Therefore, ΔH and ΔS must have similar signs and the term $T\Delta S$ must be near that of ΔH so that a slight increase or decrease in temperature is enough to shift the system toward insolubility or solubility, respectively.



As precipitation upon heating and dissolving upon cooling is not common, it was not expected to be observed for the new silver vanadium oxide fluoride, $\text{Ag}_3\text{VO}_2\text{F}_4$. However, experiments described in chapter 4, and a bit of serendipity, led to the discovery of this property for this material; and, is the fourth method to synthesize this material.

5.2 Synthesis and Characterization

5.2.1 Materials

Caution. Hydrofluoric acid is toxic and corrosive and must be handled with extreme caution and the appropriate protective gear! If contact with the liquid or vapor occurs, proper treatment procedures should be followed immediately.⁶⁻⁸

Materials. Ag_2O (99.9%, Fisher), V_2O_5 (99.6%, Alfa-Aesar), and aqueous hydrofluoric acid (48-50% HF by weight, Fisher) were used as received.

5.2.2 Synthesis

The new silver vanadium oxide fluoride $\text{Ag}_3\text{VO}_2\text{F}_4$ was synthesized from a reaction of 0.3972 g (1.716×10^{-3} mol) of Ag_2O , 0.0780 g (4.28×10^{-4} mol) of V_2O_5 , and 0.5530 g of $\text{HF}_{(\text{aq})}$ (1.3×10^{-2} mol HF) in a heat sealed Teflon [fluoro(ethylene-propylene)] pouch.⁹ The reaction proceeds at room temperature until the metal oxides are dissolved, forming a yellow solution. The dissolving processes can be assisted by manually shaking the Teflon pouch, to encourage mixing. From here, two methods can be employed to form $\text{Ag}_3\text{VO}_2\text{F}_4$: heat the reaction system to 100 °C either slowly or quickly. The former can be achieved from a water bath brought to a boil slowly with the reaction pouch in the water, and the latter from introducing the pouch into a water bath already at a boil. The product must then be filtered hot by removing the pouch from the hot water bath where it is immediately cut it open and emptied.

5.3 Results

The synthesis of $\text{Ag}_3\text{VO}_2\text{F}_4$ via precipitation upon heating was surprising. In a particular reaction that was targeting $\text{Ag}_3\text{VO}_2\text{F}_4$, too much $\text{HF}_{(\text{aq})}$ was added. Almost immediately, nearly all the Ag_2O and V_2O_5 dissolved to form a yellow solution, whereas the expected results would

have been for the immediate formation of a red precipitate, as described in chapter 4. Continuing with the reaction process anyway, with no expectations, the Teflon pouch was placed into a boiling water bath. Within 10 seconds, a deep orange precipitate fell out of solution. After no more precipitate formation was visually observed, the pouch was removed from the bath to allow it to cool so that it could be cut open and filtered to retrieve the product. Unexpectedly, after a few minutes, there was nothing to filter as the solid had dissolved. Because the yellow solution then resembled the initial solution, the pouch was placed back into the water bath and immediately, the orange precipitate began to form. This process of precipitation upon heating and dissolving upon cooling is repeatable, similar to a system changing by an equilibrium shift. Eventually the product was recovered by filtering while hot and confirmed to be $\text{Ag}_3\text{VO}_2\text{F}_4$.

Variations in the synthesis can lead to formation of large single crystals, smaller polycrystalline particles, or no product at all. Firstly, if the reaction pouch is slowly heated, $\text{Ag}_3\text{VO}_2\text{F}_4$ is precipitated slowly as larger crystals. An example of slowly heating is ramping the water bath temperature from room temperature to boiling in four or five increments over the course of three to five hours. Crystals formed can have a hexagonal plate-like or octahedral morphology up to 1 mm in dimension. Alternatively, immediate high heat exposure will lead to the rapid precipitation of polycrystalline particles. For the reverse of this equilibrium, cooling the reaction pouch to room temperature would proceed differently based on how the particles were formed. Large crystals would dissolve very slowly over the course of hours and the more quickly formed small particles would dissolve within a minute with encouragement from mixing/agitation. A second variable that was necessary to control was the quantity of $\text{HF}_{(\text{aq})}$ added. Less $\text{HF}_{(\text{aq})}$, (e.g. 0.45 g) would not dissolve all the immediately-formed $\text{Ag}_3\text{VO}_2\text{F}_4$,

preventing crystal growth or complete observation of the negative temperature coefficient of solubility. Too much $\text{HF}_{(\text{aq})}$ (e.g. 0.60 g) would fully dissolve all solid phases, but not allow precipitation or crystal growth upon heating.

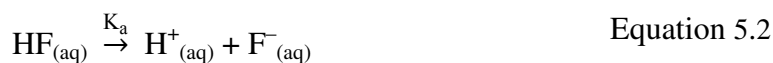
5.4 Discussion

Two hypotheses were formed to rationalize what was happening in solution. The first is that the increased temperature is changing the nature of the acidic solution, making it more or less acidic, and the species in solution were adjusted based on the influx or removal of H^+ . The second (not necessarily exclusive) hypothesis was that the process is entropy driven where waters of hydration, or associated HF molecules, are liberated from the soluble species, thus leading to new species that would combine and form a precipitate. The steps toward understanding this phenomenon were to investigate the properties of $\text{HF}_{(\text{aq})}$ between two temperatures and to learn what species might be in solution. However, the overarching explanation for both hypotheses is thermodynamics and the effects of entropy and enthalpy.

5.4.1 Temperature and Dissociation of HF

To study the first hypothesis, an understanding of both the nature of $\text{HF}_{(\text{aq})}$ solutions at elevated temperatures and the Ag- and V-species in solution were needed. By measuring the conductance of dilute HF solutions at temperature between 25 and 200 °C, Ellis was able to determine the ionic concentration and thus determine the ionization dependence on temperature.¹⁰ What was found was that at higher temperatures, the K_a of HF decreased (Equation 5.2) and K_1 for the association of the fluoride ion with HF increased (Equation 5.3). Unfortunately, this study only focused on solutions up to 0.1 molal concentration, which equates to 0.2% HF by weight (compared to the 48-50% concentration used for SVOF synthesis).

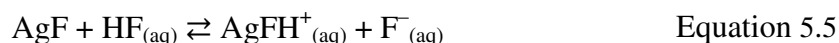
However, thermodynamics supports the measurements by Ellis, according to Equation 5.4.¹¹ The enthalpies for the ionic disassociation of the halide acids HX (X = F, Cl, Br, I) are all negative (-13, -57, -64, and -59 kJ/mol, respectively), as are the entropic changes (at 298 K, $T\Delta S$ = -31, -17, -10, and -2 kJ/mol, respectively). The much less negative entropy value for HF is due to the fluoride ion in solution directing water and HF molecules into a tetrahedral orientation, thus forming order and decreasing entropy.¹² As both ΔH and ΔS are negative, temperature will have an effect in equation 5.4. As the solution is cooled, K_a will grow larger and lead to more dissociated HF. As the solution is heated, where precipitation of $\text{Ag}_3\text{VO}_2\text{F}_4$ is observed, HF becomes more associated (i.e. a decrease in $[\text{H}^+_{(\text{aq})}]$ and $[\text{F}^-_{(\text{aq})}]$). It is this decreased acidity that would affect the species in solution.



$$\ln K_a(T) = \frac{-\Delta G}{RT} = \frac{1}{R} \left(\Delta S - \frac{\Delta H}{T} \right) \quad \text{Equation 5.4}$$

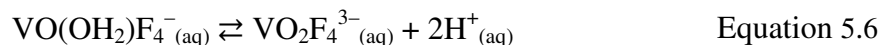
The literature has very few reports on the species of silver dissolved in hydrofluoric acid. Silver oxide dissolved in HF, like many oxides, will react with the acid to form water and the complementary fluoride, in this case, AgF. However, it is not the phase that can be recovered from these solutions that is important, but rather it is the form of the dissolved ion that would be affected by changes from acidity and temperature. In a study on the reaction of AgF with arenes in anhydrous HF, McCaulay and Lien conclude that AgF acts as a base and probably forms the species AgFH^+ according to equation 5.5.¹³ In addition, Klatt postulated the presence of AgFH^+ from an elevated boiling point according to the addition of 4 molal from AgN_3 dissolving in HF.

That is, the boiling point increase corresponded to 4 moles of additional ions assigned to AgFH^+ , HN_3H^+ , and 2F^- .¹⁴ Not much, if any, has been said on the reactivity of this species in a changing pH environment. Perhaps when the temperature is raised, where less $\text{H}^+_{(\text{aq})}$ and $\text{F}^-_{(\text{aq})}$ are available, equation 5.5 would shift to the right. But, as the silver is already completely dissolved, the equation already lies fully to the right and thus a decreased acidity would have no effect.



While plenty is known about vanadium oxides in aqueous solutions, both acidic and basic, vanadium (V) oxide in $\text{HF}_{(\text{aq})}$ has been shown or theorized to have either possible structure for the species $[\text{VO}_2\text{F}_4]^{3-}$. The *trans* conformer was rationalized from ^{19}F and ^{51}V NMR. The NMR studies by Gillespie and Rao performed on $\text{Na}(\text{NH}_4)_2\text{VO}_2\text{F}_4$ in water and V_2O_5 in 48% $\text{HF}_{(\text{aq})}$ confirmed the 1:4:6:4:1 quintet (for the ^{51}V signal) observed by Hatton *et al.*^{15,16} The structure that would explain the four equivalent fluoride ligands was initially believed to be a square pyramidal VOF_4^- and then expanded to include the *trans*- $\text{VO}_2\text{F}_4^{3-}$ structure. However, Gillespie and Rao suggest that even though the structure may be VOF_4^- , it is probably hydrated by a water molecule as a *trans* octahedral $\text{VO}(\text{OH}_2)\text{F}_4^-$ structure; and, depending on the acidity, may lose one or two protons to finally give $\text{VO}_2\text{F}_4^{3-}$. It is this chemistry that may lead toward precipitation of $\text{Ag}_3\text{VO}_2\text{F}_4$. In other words, where the completely dissolved system at room temperature would have vanadium as $\text{VO}(\text{OH}_2)\text{F}_4^-$, an increase in temperature may lead to the $\text{VO}_2\text{F}_4^{3-}$ species that would be more susceptible to combination with silver. As the temperature of the Ag_2O - V_2O_5 - $\text{HF}_{(\text{aq})}$ system is raised and $[\text{H}^+_{(\text{aq})}]$ and $[\text{F}^-_{(\text{aq})}]$ in the solution decrease, $\text{VO}(\text{OH}_2)\text{F}_4^-$ would lose the first and second protons in the more basic solution according to

equation 5.6. In the opposite fashion, as the temperature of the system is lowered, the increased $[H^+]$ would help re-dissolve $Ag_3VO_2F_4$.



Other studies on the structure of vanadium centered species utilized ESR, IR, and a single crystal X-ray diffraction to show both *trans* and *cis* conformers. Rao *et al.* irradiated $(NH_4)_3VO_2F_4$ with gamma radiation to reduce V^{5+} to V^{4+} to be studied by electron spin resonance (ESR).¹⁷ It was concluded that the isolated $VO_2F_4^{3-}$ anion (i.e. no V-O-V chains) distorts from D_{4h} symmetry as V^{5+} into C_{4v} symmetry as V^{4+} . However, on the same material, Davidovich *et al.* found VO_2^+ stretching vibrations in the IR spectra indicating non-linearity. In addition, single crystal X-ray structural determination of the same material, $(NH_4)_3VO_2F_4$, showed two distinct isolated $VO_2F_4^{3-}$ octahedra.¹⁸ One had oxide/fluoride distortion and thus the conformation could not be determined. However, the other had a *cis* conformation that showed the vanadium center distorted toward the octahedral edge, forming two shorter stronger V-O bonds. It is unclear, however, as to how the vanadium species in the Ag_2O - V_2O_5 - $HF_{(aq)}$ system, if it is *trans*- $VO(OH_2)F_4^{3-}$ / $VO_2F_4^{3-}$, reorients to the *cis* conformation in the solid state.

5.4.2 Temperature and Waters of Hydration

Another argument as to the origin of a compound precipitating upon heating is due to liberation of associated water (e.g. $AgF \cdot 2H_2O$) or hydrofluoride (e.g. $AgF \cdot 2HF$) from the solid state to form a compound without the associated molecule(s). Findlay describes this and other examples of the phase rule; figures here were adapted from therein.¹⁹ To begin to understand the system, it is useful to begin with the solubility and precipitation of another system with simple compounds and build to more complex systems. For example, a system with NaCl and KCl

dissolved in H_2O would precipitate each salt individually. Evaporating H_2O from an unsaturated solution would alter the molar ratio of the three compounds along the dashed line away from the H_2O corner (Figure 5.1).^{20,21} When the ratio lies on the isothermal solubility curve, in this example, NaCl will begin to precipitate. This will continue until the concentration of the salts in solution reaches the intersection of the NaCl and KCl solubility curves where both salts will coprecipitate. A slightly more complex system is one where the either or both salt phases precipitate as hydrates (Figures 5.2a, 5.2b).^{22,23} Similar evaporation and precipitation scenarios would precipitate the respective salt or hydrated salt. If the two salts can combine to form a double salt, a third isothermal solubility curve will appear in the diagram (Figure 5.3a).²⁴ And likewise, a double salt with a hydrate can form from its two respective hydrated salts (Figure 5.3b).²⁵

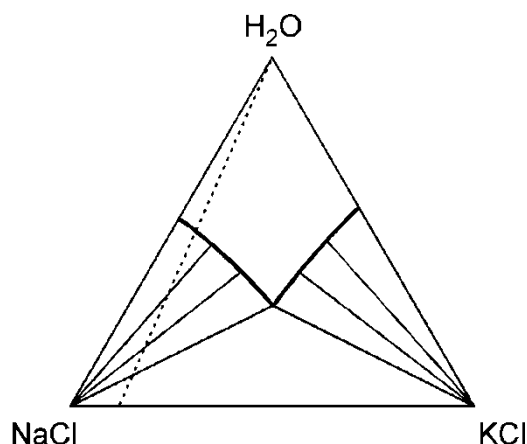


Figure 5.1 Solubility curves for NaCl and KCl in H_2O . Following the dashed line from the H_2O vertex would first precipitate NaCl and eventually coprecipitate NaCl and KCl .

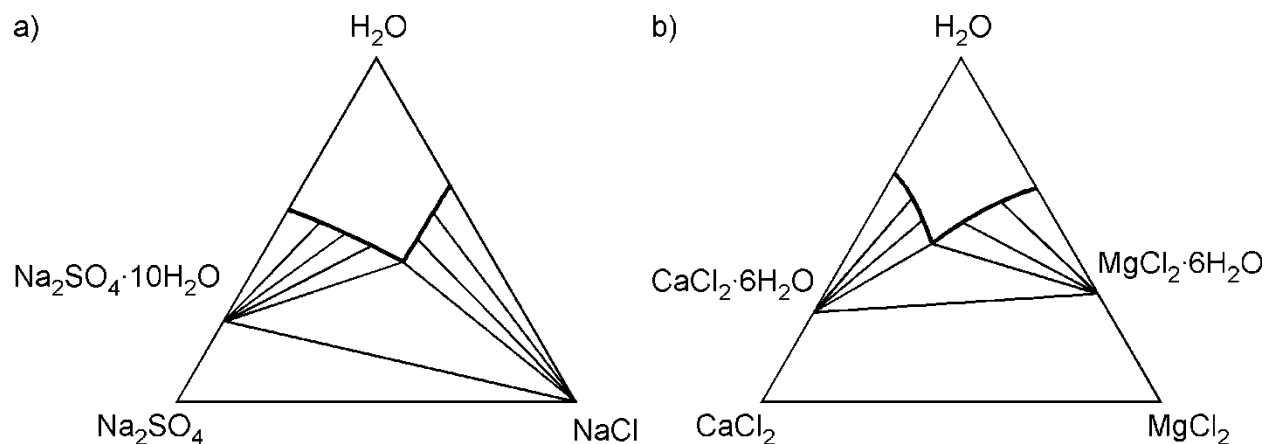


Figure 5.2 Solubility curves for (a) Na_2SO_4 and NaCl in H_2O and (b) CaCl_2 and MgCl_2 in H_2O which show their respective hydrated precipitates of $\text{Na}_2\text{SO}_4 \cdot 10\text{H}_2\text{O}$, $\text{CaCl}_2 \cdot 6\text{H}_2\text{O}$, and $\text{MgCl}_2 \cdot 6\text{H}_2\text{O}$.

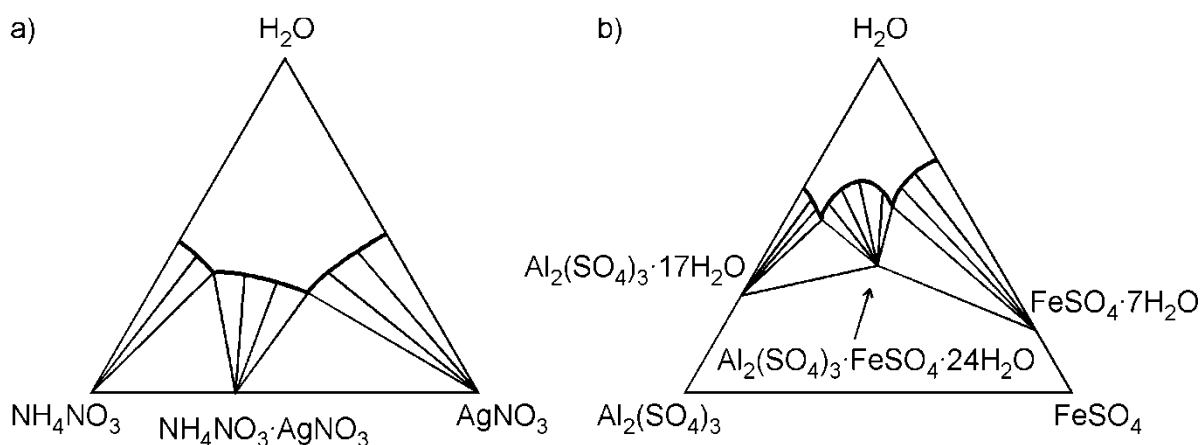
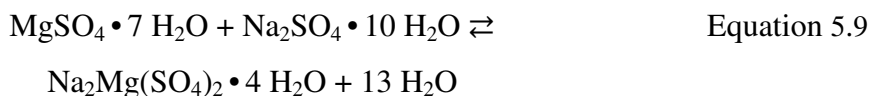
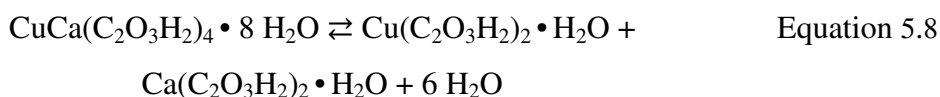
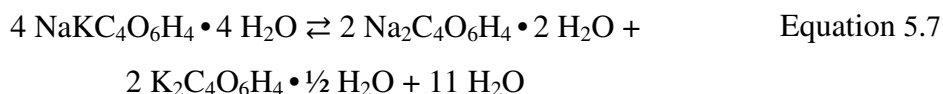


Figure 5.3 Solubility curves for (a) NH_4NO_3 and AgNO_3 in H_2O , where the double salt $\text{NH}_4 \cdot \text{AgNO}_3$ forms and (b) $\text{Al}_2(\text{SO}_4)_3$ and FeSO_4 in H_2O where $\text{Al}_2(\text{SO}_4)_3 \cdot \text{FeSO}_4 \cdot 24\text{H}_2\text{O}$ can be recovered, along with the respective single salt hydrates.

Temperature plays an important role in the solubility of hydrated salts and formation of double salts. For example, heating a single salt hydrate, $\text{Na}_2\text{SO}_4 \cdot 10\text{H}_2\text{O}$ will drive off the water to form anhydrous sodium sulfate at a transition temperature of 32.5°C . The similar phenomena can occur for a double salt. For example, equation 5.7 shows the dehydration of a double salt ($\text{NaKC}_4\text{O}_6\text{H}_4 \cdot 4\text{H}_2\text{O}$) to two single lesser-hydrated salts with the release of water at 55°C .²⁶ The

process is reversible as long as the system is in a closed vessel to prevent the loss of water. Another system, while it does not give the appearance of liquefaction owing to fewer waters of hydration released, is that from the double salt $\text{CaCu}(\text{C}_2\text{H}_3\text{O}_2) \cdot 8\text{H}_2\text{O}$ according to equation 5.8.²⁷ The opposite effect is also possible: a double salt can be formed from two single hydrated salts above the transition temperature, as for the case of sodium and magnesium sulphates forming astracanite, $\text{Na}_2\text{Mg}(\text{SO}_4)_2$, equation 5.9. The similarity in all of these processes is the liberation of water upon heating. The general rule, stated by Findlay, is that “if the water of crystallization of the two constituent salts together is greater than that of the double salt the latter will be produced from the former on raising the temperature.”¹⁹ LeChatelier’s principle can be applied too. As heat is applied to the system, it will shift according to the direction that is accompanied by the absorption of heat. In the case of these salts, the heat involved in the hydration and dehydration is greater than the other thermodynamic changes that also happen, thus driving the overall sign of ΔG .



From the examples in Equations 5.7 - 5.9, triangular solubility diagrams can be built for a system at both low and high temperatures. Taking the reaction represented in equation 5.9, the single salts $\text{MgSO}_4 \cdot 7\text{H}_2\text{O}$ and $\text{Na}_2\text{SO}_4 \cdot 10\text{H}_2\text{O}$ would be the only phases that precipitate at low temperatures (Figure 5.4a). However, as the temperature is raised, the formation of the double

salt $\text{Na}_2\text{Mg}(\text{SO}_4)_2 \cdot 4\text{H}_2\text{O}$ would be possible and therefore have its own solubility curve (Figure 5.4b). Initially, the double salt would be incongruently saturating, as shown by the dashed line that connects the point for the double salt to the H_2O vertex that does not pass through the solubility curve for the double salt. As the temperature of the system is increased, the double salt becomes congruently saturating and the solubility curve would extend toward the line and eventually pass it, which leads to a diagram similar to Figure 5.3.

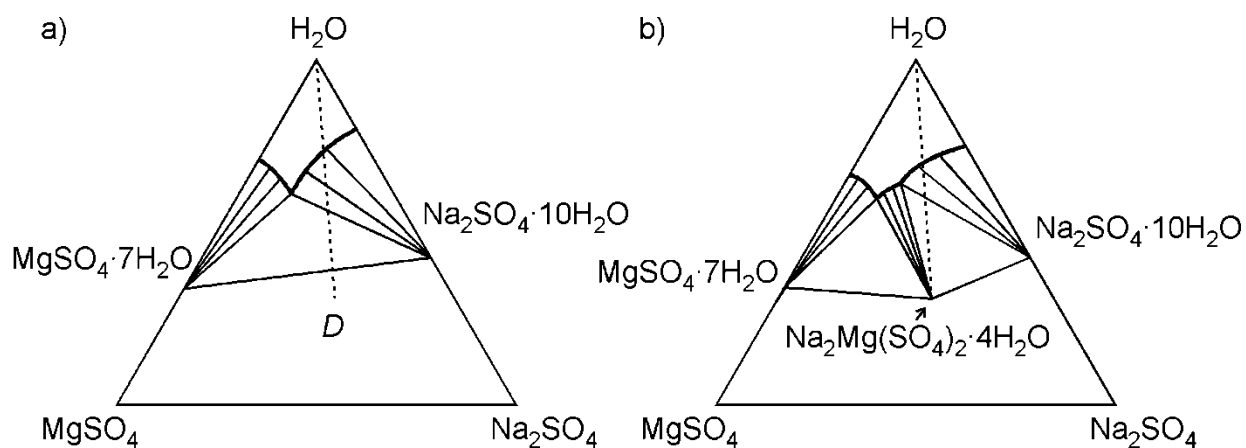


Figure 5.4 Solubility curves for MgSO_4 and Na_2SO_4 in H_2O and their respective hydrates $\text{MgSO}_4 \cdot 7\text{H}_2\text{O}$ and $\text{Na}_2\text{SO}_4 \cdot 10\text{H}_2\text{O}$ at (a) low temperature and (b) high temperature showing the appearance of the double salt $\text{Na}_2\text{Mg}(\text{SO}_4)_2 \cdot 4\text{H}_2\text{O}$, also represented by *D*.

The thermodynamically-driven negative temperature coefficient of solubility of $\text{Ag}_3\text{VO}_2\text{F}_4$ can be rationalized by a solubility diagram that includes single salts of silver and vanadium in hydrofluoric acid. A combination of two solid salts with the release of the water or hydrofluoride of crystallization could lead to the formation of what may be considered a double salt, $\text{Ag}_3\text{VO}_2\text{F}_4$. Therefore, salts of silver and vanadium should be investigated as they are formed in hydrofluoric acid. The solubility diagram of AgF in $\text{HF}_{(\text{aq})}$ was examined by Thomas and Jache for solutions at $0\text{ }^\circ\text{C}$ and $-15\text{ }^\circ\text{C}$.²⁸ In the AgF - HF - H_2O solubility diagram, AgF is fairly soluble and precipitates out as $\text{AgF} \cdot n\text{H}_2\text{O}$ ($n = 4, 2, 2$), $3\text{AgF} \cdot 2\text{HF}$, $\text{AgF} \cdot 7\text{HF} \cdot 2\text{H}_2\text{O}$, or

$\text{AgF} \cdot n\text{HF}$ ($n = 2, 3, 5$) as evaluated against increased HF concentrations up to 56% by weight HF (Figure 5.5). All but one of these single salts of silver are similar once the respective crystallized “solvent” is released. The solubility of V_2O_5 in hydrofluoric acid was examined by Nikolaev and Buslaev for solutions at 0 °C, 16°C and 25°C.^{29,30} In the V_2O_5 -HF- H_2O solubility diagram, V_2O_5 is soluble and precipitates as V_2O_5 , $3\text{VO}_2\text{F} \cdot \text{HF} \cdot \text{H}_2\text{O}$, $4\text{VOF}_3 \cdot 3\text{HF} \cdot 3\text{H}_2\text{O}$, $2\text{VOF}_3 \cdot 3\text{HF} \cdot \text{H}_2\text{O}$, and VOF_3 from solutions of HF with increased concentrations up to 82% by weight (Figure 5.5).

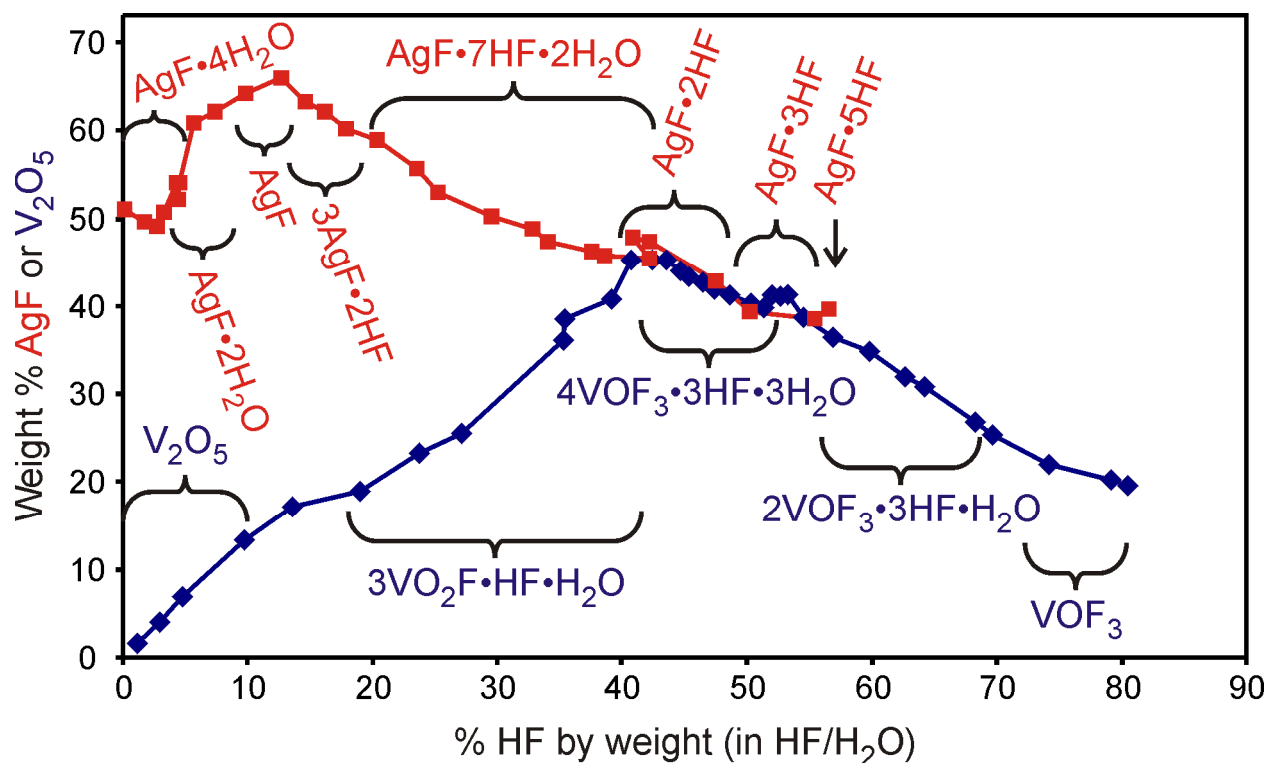
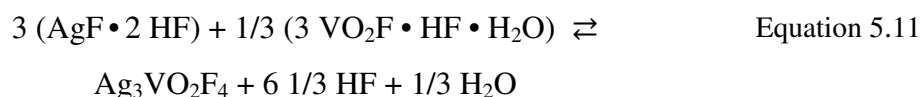
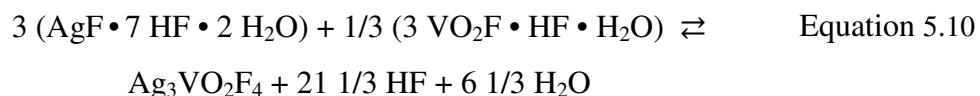


Figure 5.5 Solubility and precipitate diagram for AgF -HF- H_2O and V_2O_5 -HF- H_2O systems that show the precipitates recovered from saturated solutions. Notable are the vast number of phases with water and hydrofluoride of crystallization.

From the studies on the silver and vanadium precipitates from hydrofluoric acid, it is apparent that the salts that are most interesting are those from solutions below a concentration of 48-50% HF by weight. The lower concentration bound, since both silver and vanadium are

present in the reaction system that produces $\text{Ag}_3\text{VO}_2\text{F}_4$, cannot be determined because the precipitates would be affected by the common-ion effect. What can be assumed from this is that the apparent $\text{HF}_{(\text{aq})}$ concentration experienced by silver and vanadium should have a concentration lower than the stock 48-50% $\text{HF}_{(\text{aq})}$ solution. Therefore, the salts that are of concern would be $\text{AgF} \cdot 7\text{HF} \cdot 2\text{H}_2\text{O}$ and $\text{AgF} \cdot 2\text{HF}$ for silver and $3\text{VO}_2\text{F} \cdot \text{HF} \cdot \text{H}_2\text{O}$ and $4\text{VOF}_3 \cdot 3\text{HF} \cdot 3\text{H}_2\text{O}$. Together, it is possible to write a balanced equation for the formation $\text{Ag}_3\text{VO}_2\text{F}_4$ that also yields HF and H_2O (equation 5.10, 5.11). This equation follows the arguments above for the release of the water of crystallization upon heating. The difference between this equation and equations 5.7 - 5.9 is that the silver and vanadium species are completely dissolved beforehand and the reaction yields the less soluble product. However, it would be interesting to experimentally isolate the silver and vanadium single salts and react them together per equations 5.10 and 5.11.



Finally, from these reactions between two single salts producing a double salt, water, and hydrogen fluoride upon heating, it is possible to construct triangular solubility diagrams similar to the ones for MgSO_4 and Na_2SO_4 in H_2O that changed with a changed temperature. As an example, from Equation 5.11, the compounds AgF and VO_2F can be plotted against $\text{H}_2\text{O} / \text{HF}$ and on the edges are plotted their hydrate and/or hydrofluoride salts and the anhydrous double salt (Figure 5.6). The solubility curve shape and position are not meant to reflect measured values, but to give an idea of the concept. The solubility diagram for the low temperature system,

where everything is dissolved, would resemble Figure 5.4a, where the high temperature system would reflect the figure below.

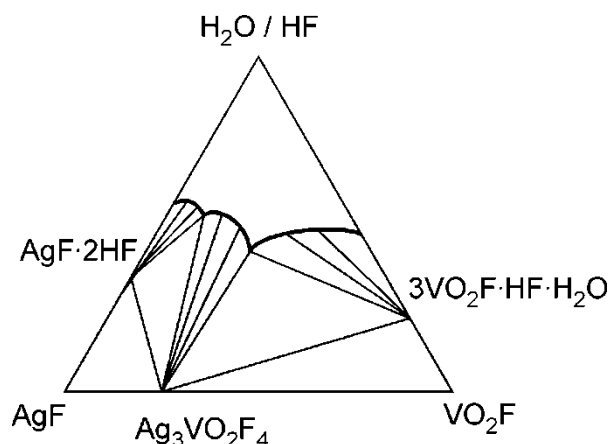


Figure 5.6 Theoretical solubility curves for AgF and VO_2F in $\text{H}_2\text{O}/\text{HF}$ and their respective hydrates $\text{AgF}\cdot 2\text{HF}$ and $3\text{VO}_2\text{F}\cdot \text{HF}\cdot \text{H}_2\text{O}$ at high temperature. The magnitude and width of the curves were arbitrarily drawn, though placement of each salt is accurate.

5.5 Future Directions

Progression from the research presented here should involve attempts to synthesize materials with different transition metals substituted for vanadium, namely other d^0 transition metal cations. Many of these metals are soluble in hydrofluoric acid and have been isolated as metal oxide, metal oxide fluoride, and/or metal fluorides with water or hydrofluoride of crystallization. Studies on the solubility and precipitates of Ti^{4+} , V^{5+} , Zr^{4+} , Nb^{5+} , Mo^{6+} , Ta^{5+} , and W^{6+} from various concentrations of hydrofluoric acid are presented in Figure 5.7.^{29,31-35} While it is not apparent which of these metal salts could react with a silver salt to form a compound, the presence of the crystallized solvent molecules may at least indicate some level of a possible reaction.

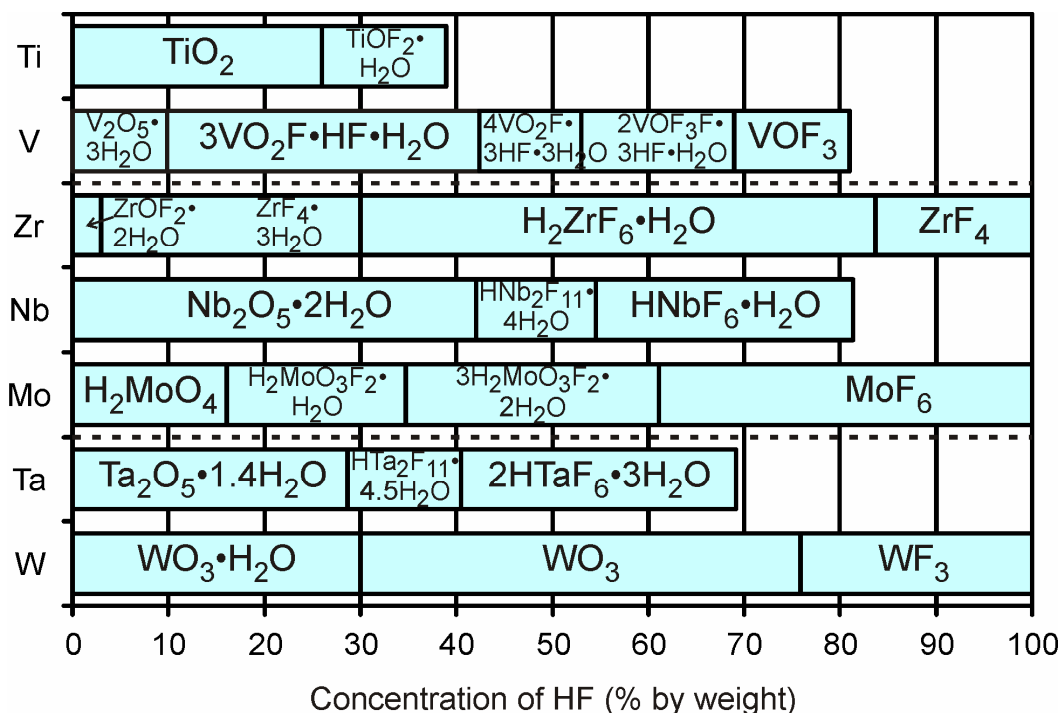


Figure 5.7 Precipitation of metal oxides / oxide fluorides / fluorides from a variety of hydrofluoric acid solution concentrations. Dotted lines were drawn to separate elements by period.

Indeed, initial studies on the reaction between 2:1 molar ratio of Ag_2O and MoO_3 in hydrofluoric acid under hydrothermal conditions (150 °C for 24 hours) have given promising results that other cryolite-type phases can be synthesized by similar means. The product recovered was analyzed by powder X-ray diffraction and did not match any known silver and/or molybdenum powder diffraction file pattern. However, it did closely match that for $\text{Ag}_3\text{VO}_2\text{F}_4$. By comparing the peaks with those for $\text{Ag}_3\text{VO}_2\text{F}_4$, a peak shift can be observed (Figure 5.8). Indeed, the larger Mo^{6+} (0.73 Å vs. 0.68 Å for V^{5+}) in the B-site shifted the peaks closer together for $\text{Ag}_3\text{MoO}_3\text{F}_3$ as expected from the physics of the X-ray diffraction measurement.³⁶ To grow crystals of this material, similar crystal growth techniques should be studied: medium to high concentrations of $\text{HF}_{(\text{aq})}$, mild to high excess mole quantity of $\text{HF}_{(\text{aq})}$, and a slow temperature

change from room temperature to 100°C. It is also published that the phases Ag_3TiOF_5 , $\text{Ag}_3\text{NbO}_2\text{F}_4$, and $\text{Ag}_3\text{WO}_3\text{F}_3$, which have been synthesized by a solid state reaction, have similar unit cell dimensions as $\text{Ag}_3\text{VO}_2\text{F}_4$, as determined by powder X-ray diffraction.³⁷ Growth of single crystals of these materials might be possible by slowly heating the necessary respective solutions in hydrofluoric acid.

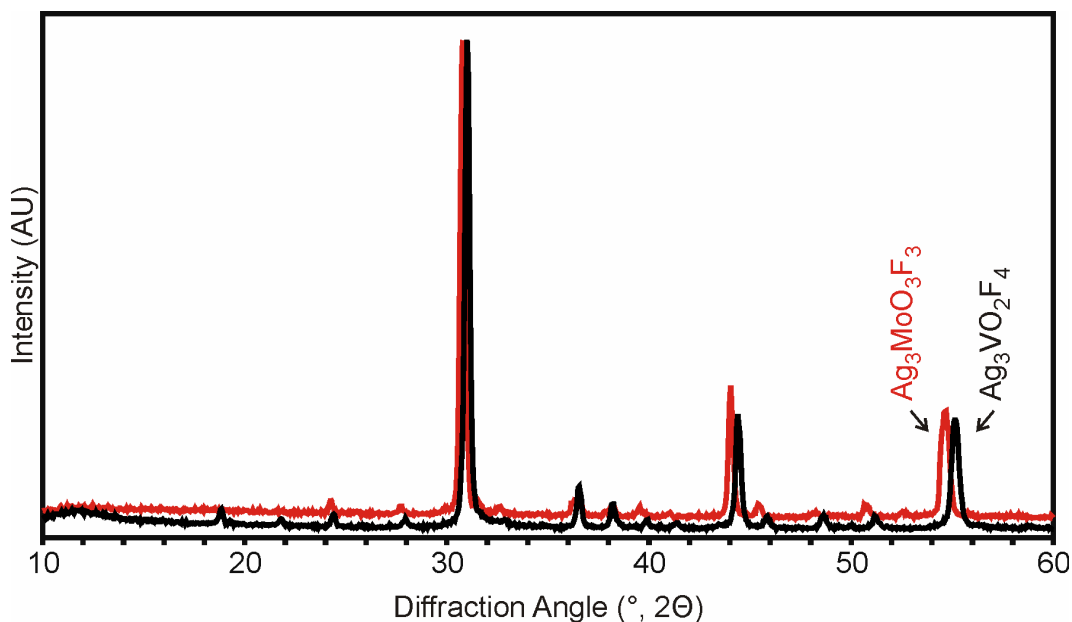


Figure 5.8 Powder X-ray diffractogram of $\text{Ag}_3\text{VO}_2\text{F}_4$ and $\text{Ag}_3\text{MoO}_3\text{F}_3$ showing the peak shift to smaller angles for the larger lattice parameters of $\text{Ag}_3\text{MoO}_3\text{F}_3$ owing to different V^{5+} and Mo^{6+} radii.

5.6 Conclusions

Crystal growth of $\text{Ag}_3\text{VO}_2\text{F}_4$ occurs from a hydrofluoric acid solution with an increase of temperature, from room temperature up to 100 °C. This phenomenon is known for materials that have, by definition, a negative temperature coefficient of solubility. Crystal quality is improved if the initial solution is unsaturated (yet near saturation) and the temperature is raised slowly. While precipitation will occur from a saturated solution that was not completely dissolved, a

solution that is too unsaturated will not yield a product. When the solution is cooled, the higher crystalline product dissolves much more slowly than a product that was precipitated very rapidly.

Chapter Six

Room Temperature Synthesis of $\text{Ag}_4\text{V}_2\text{O}_6\text{F}_2$

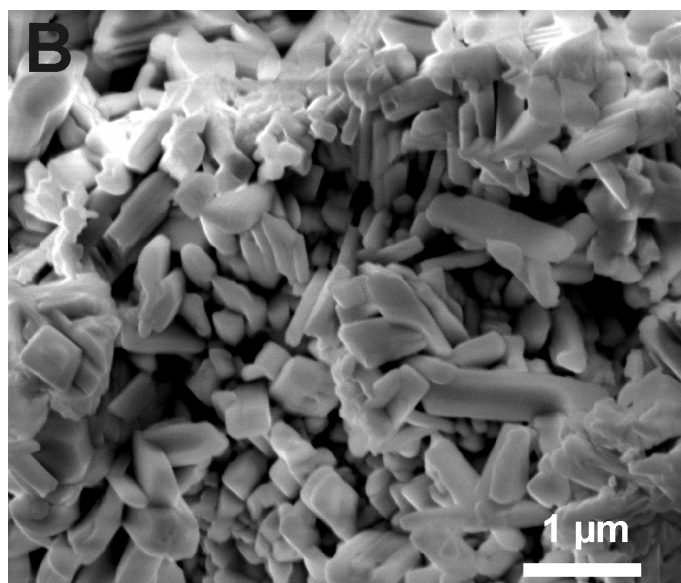
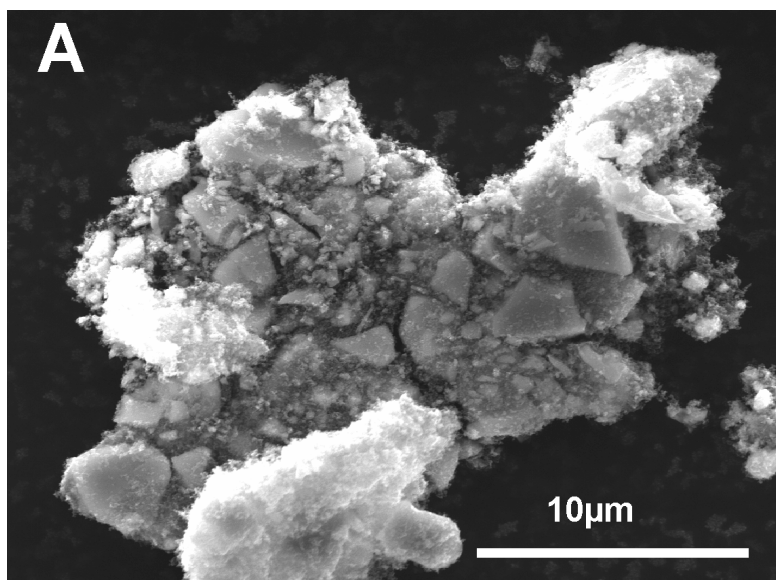
6.1 Introduction

Implantable biomedical devices address a variety of needs including nerve/neuron stimulation, drug delivery or cardiac management. The energy source, provided by an implanted battery which converts chemical energy to electrical energy, requires specific characteristics in accordance with the application targeted. Depending on power requirements, a variety of lithium-based primary batteries can be implemented, such as Li-I₂, Li-SOCl₂ or Li-Ag₂V₄O₁₁ (SVO) for pacemakers, neuro-stimulators or Implantable Cardioverter Defibrillators (ICDs), respectively.¹ An ICD is a device implanted in a patient's chest who is at risk of tachycardia. The device, which continuously monitors the cardiac beat, can serve similarly to a pacemaker by delivering low-energy stimuli (50-100 μ W), or addresses ventricular fibrillation by administering a vigorous electrical shock of as high as 30-40 J at 700 – 800 V to the right ventricle.^{2,3} The SVO cathode became the choice material for the ICD battery market since the original proposal from Keister et al. in 1984.⁴ Ever since, the importance of SVO as the foremost cathode has grown because it fulfills the stringent requirements of high chemical/electrochemical stability and high electrochemical behavior predictability together with exhibiting high discharge rate capability owing to its great electronic / ionic conduction ($\sigma_e \sim 10^{-2}$ - 10^{-3} S/cm and $D_{(Li+)} \sim 10^{-8}$ cm²/s).⁵⁻⁸

Many advances have brought the ICD Li-SVO system to its present maturity, including improved separator thinness, synthetic procedures, and particle/electrolyte interface.⁹⁻¹⁴ Further progress in this area would stem from the design of a new cathode material which would (i) uptake lithium/electrons at higher potential and (ii) display a greater phase density to decrease capacitor charge time and battery size, respectively, while maintaining the high

chemical/electrochemical cathode stability. With this in mind, our effort was concentrated on the exploration of dense silver oxide fluoride materials, most notably in the vanadium system. $\text{Ag}_4\text{V}_2\text{O}_6\text{F}_2$ (SVOF), the first silver vanadium oxide fluoride material was synthesized in the $\text{Ag}_2\text{O} / \text{V}_2\text{O}_5 / \text{HF}_{(\text{aq})}$ system and exhibits electrochemical activity vs. lithium. In particular, silver reduction occurs near 3.45 V (vs. Li^+/Li) and the higher crystal structure density ($\rho = 6.03 \text{ g/cm}^3$ vs. 4.80 g/cm^3 for SVO) gives rise to a larger energy density (i.e. volumetric capacity).¹⁵ Nevertheless, the large particle size resulting from the reported hydrothermal synthesis of SVOF ($> 1 \text{ mm}$ single crystals and $> 10 \text{ }\mu\text{m}$ after manually grinding, Figure 6.1a) hinders high discharge rate capability owing to ionic conduction limitations during the Ag^+/Li^+ displacement reaction.¹⁶ One approach for improvement, which is the focus of this chapter, is to drastically reduce the particle size to minimize the ion motion length in the solid.

Soft chemistry approaches have gained research interests for two reasons. Firstly, these methods allow material to be accurately tailored (with regards to particle size, texture and morphology, porosity, etc.) through different thermodynamic parameters such as pH, temperature or precursor concentration. The second driving force stems from an environmental aspect where a low temperature approach is synonymous with energy savings for large-scale chemical transformations. Among the different solvents and/or mineralizers used in solution chemistry, aqueous HF has received little attention while fluorides,^{17,18} oxyfluorides^{19,20} or fluorophosphates^{21,22} show promise as new cathode materials for Li-ion batteries. Moreover, what is presented here is the first room temperature synthesis of a cathode material, $\text{Ag}_4\text{V}_2\text{O}_6\text{F}_2$ (SVOF-RT), for lithium batteries, in addition to a new silver vanadium oxide fluoride $\text{Ag}_3\text{VO}_2\text{F}_4$.



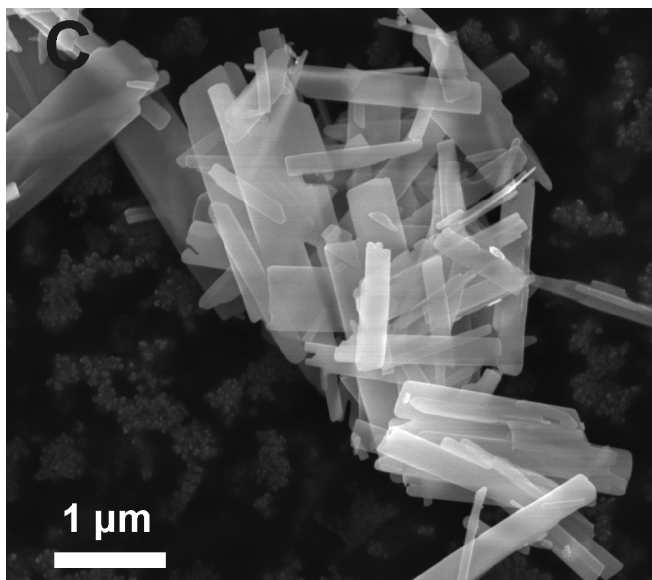


Figure 6.1 Scanning Electron Microscopy micrographs of particles used as cathode in lithium batteries (a) $\text{Ag}_4\text{V}_2\text{O}_6\text{F}_2$ synthesized by hydrothermal method (SVOF-Hyd), (b) $\text{Ag}_4\text{V}_2\text{O}_6\text{F}_2$ precipitated at room temperature (SVOF-RT) and (c) $\text{Ag}_2\text{V}_4\text{O}_{11}$ synthesized under hydrothermal conditions (ϵ -SVO).

6.2 Synthesis and Characterization

6.2.1 Materials

Caution. Hydrofluoric acid is toxic and corrosive and must be handled with extreme caution and the appropriate protective gear! If contact with the liquid or vapor occurs, proper treatment procedures should be followed immediately.²³⁻²⁵

Materials. Ag_2O (99.9%, Fisher), V_2O_5 (99.6%, Alfa-Aesar), and aqueous hydrofluoric acid (48-50% HF by weight, Fisher) were used as received.

6.2.2 Synthesis

$\text{Ag}_4\text{V}_2\text{O}_6\text{F}_2$ was prepared from a reaction of 0.3972 g (1.713×10^{-3} mol) of Ag_2O , 0.0777 g (4.272×10^{-4} mol) of V_2O_5 , 0.2561 g of $\text{HF}_{(\text{aq})}$ (6.274×10^{-3} mol HF), and 1.5 g H_2O . Reactants were loaded into Teflon containers – first the oxides followed by the water and finally the $\text{HF}_{(\text{aq})}$

– and allowed to react for as long as 72 hours. The pouch was manually agitated to encourage thorough mixing. The pouch was opened in air and the contents were vacuum filtered to retrieve orange polycrystalline $\text{Ag}_4\text{V}_2\text{O}_6\text{F}_2$.

6.2.3 Characterization

Single phase $\text{Ag}_4\text{V}_2\text{O}_6\text{F}_2$ was recovered as determined by the XRD full pattern matching refinement (Figure 6.2). The refined lattice cell parameters ($a = 5.601(1) \text{ \AA}$, $b = 10.551(2) \text{ \AA}$, $c = 12.511(3) \text{ \AA}$, $\beta = 90.36(3)^\circ$ and $V = 739.4 \text{ \AA}^3$) are comparative to those determined for the single crystal X-ray structure ($a = 5.596(1) \text{ \AA}$, $b = 10.554(3) \text{ \AA}$, $c = 12.516(3) \text{ \AA}$, $\beta = 90.46(5)^\circ$ and $V = 739.2 \text{ \AA}^3$) considering the former was collected at room temperature and the latter at 153 K. TEM investigation also validated the single phase of the product in that the as-precipitated material did not contain any supplementary amorphous phase undetectable by powder X-ray diffraction.

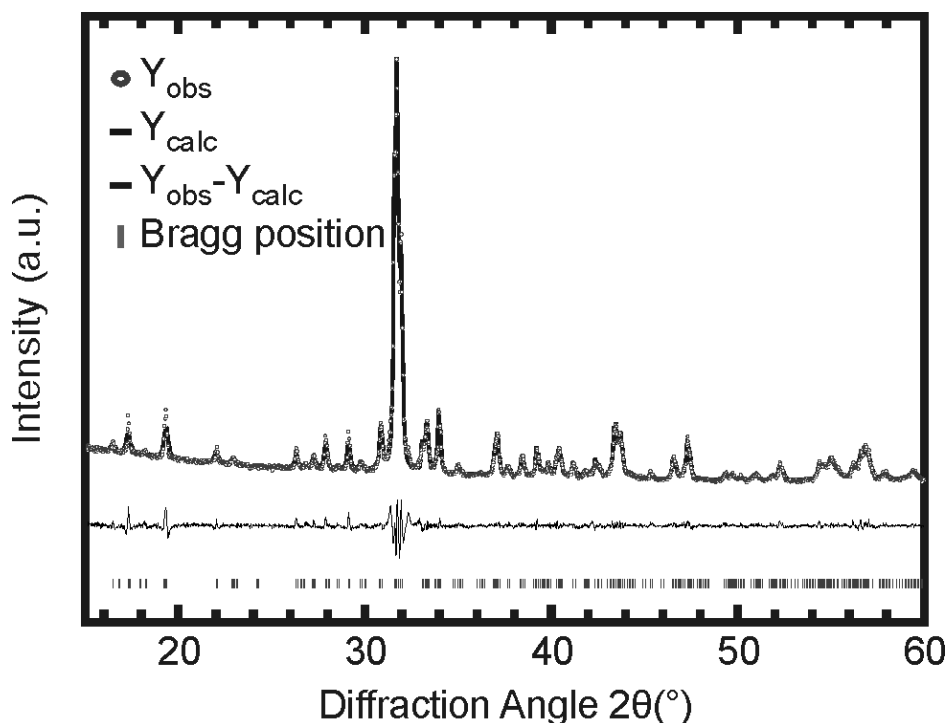


Figure 6.2 Full-pattern matching refinement of the powder X-ray diffraction pattern of ground $\text{Ag}_4\text{V}_2\text{O}_6\text{F}_2$ (SVOF). Scanning Electron Microscopy pictures of SVOF as prepared at room temperature in inset.

6.3 Results and Discussion

6.3.1 Synthesis

Solution-phase synthesis of silver vanadates has been studied for over a century at both elevated and room temperatures.²⁶⁻²⁹ The appeal of such low-temperature ($< 100\text{ }^\circ\text{C}$) approaches and draw for continued development of SVOF led to the exploration of the $\text{Ag}_2\text{O} / \text{V}_2\text{O}_5$ system in various concentrations of $\text{HF}_{(\text{aq})}$. It was hypothesized that $\text{Ag}_4\text{V}_2\text{O}_6\text{F}_2$ would form from reactions with more dilute $\text{HF}_{(\text{aq})}$ owing to the nature of the system studied at hydrothermal conditions.^{15,30-33} Indeed, SVOF was one of the phases formed at room temperature from a molar reactant ratio of $4:1:15:x$ $\text{Ag}_2\text{O}:\text{V}_2\text{O}_5:\text{HF}:\text{H}_2\text{O}$, where $x = 180$ to form $\text{Ag}_4\text{V}_2\text{O}_6\text{F}_2$ and $x = 17$ to form the new $\text{Ag}_3\text{VO}_2\text{F}_4$. A $4:1$ $\text{Ag}_2\text{O}:\text{V}_2\text{O}_5$ ratio is needed owing to the higher relative

solubility of silver.^{34,35} The minimum value of x is 17 due to the concentration of the $\text{HF}_{(\text{aq})}$ stock solution of 48-50% HF by weight, and a value of $x = 180$ corresponds to a concentration of 7% $\text{HF}_{(\text{aq})}$. Figure 6.3 shows a series of powder X-ray diffractograms of the product from reactions with various acid concentrations. While using 48-50% $\text{HF}_{(\text{aq})}$ gives rise to the new silver dense oxide fluoride $\text{Ag}_3\text{VO}_2\text{F}_4$, a HF concentration decreased to 33% allows formation of $\text{Ag}_4\text{V}_2\text{O}_6\text{F}_2$ alongside $\text{Ag}_3\text{VO}_2\text{F}_4$. By a concentration of 7%, $\text{Ag}_4\text{V}_2\text{O}_6\text{F}_2$ is formed without $\text{Ag}_3\text{VO}_2\text{F}_4$ as a secondary phase. The particle sizes of SVOF-RT, as determined by SEM, were 0.5 to 1 μm (Figure 6.1b). Yield was affected by variations on the reaction time and $\text{HF}_{(\text{aq})}$ concentration (i.e. adjusting x). Specifically, a reaction time from 10 minutes to 72 hours increased the yield of SVOF-RT based on silver from 4% to 16%, where the longer reaction times encourage further nucleation rather than particle growth and the majority of the product was precipitated in about 1 hour.

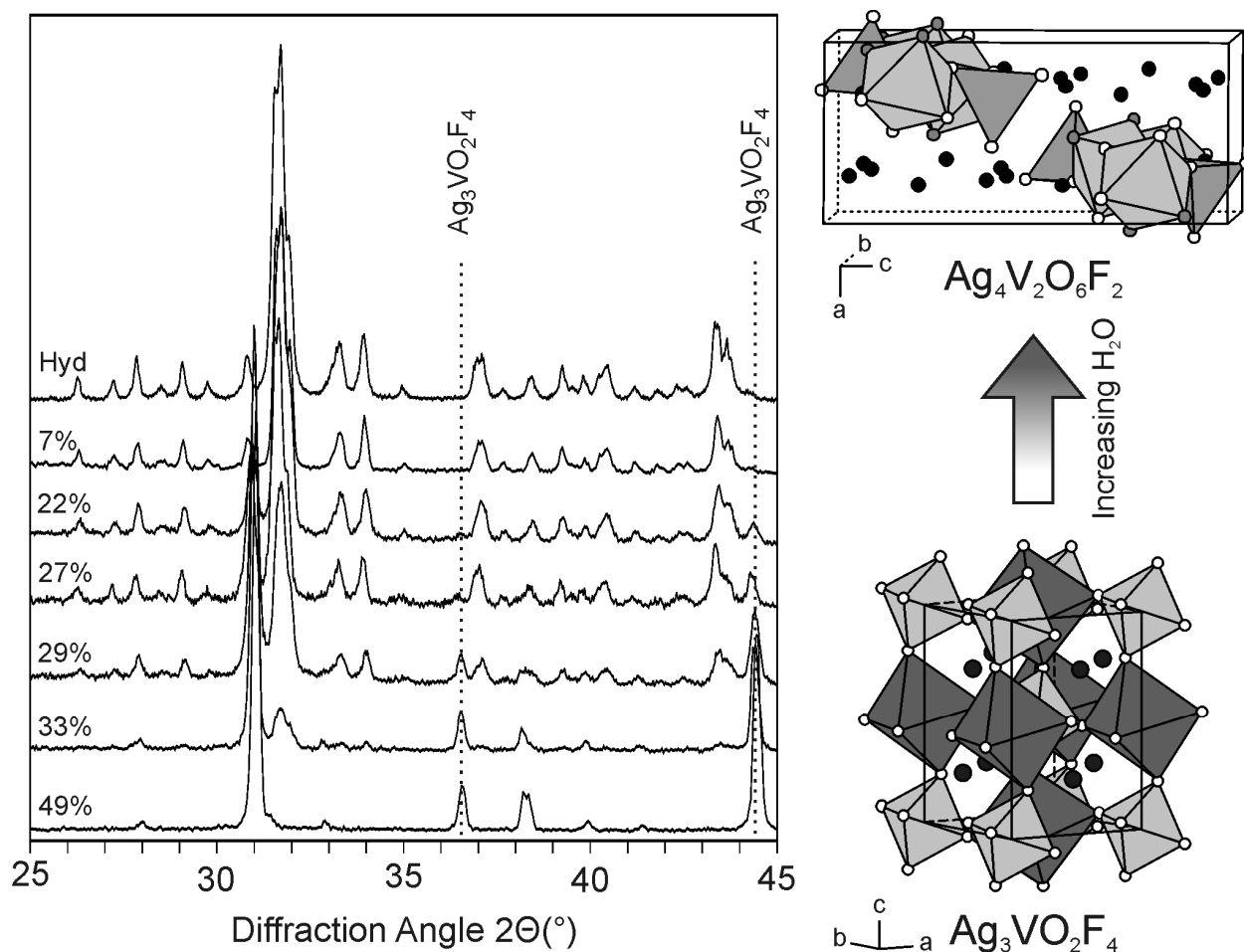


Figure 6.3 A series of powder X-ray diffractograms from reactions with a decreasing $\text{HF}_{(\text{aq})}$ concentration (from the bottom up). $\text{Ag}_3\text{VO}_2\text{F}_4$ is formed with concentrated $\text{HF}_{(\text{aq})}$, and phase pure $\text{Ag}_4\text{V}_2\text{O}_6\text{F}_2$ at 7% $\text{HF}_{(\text{aq})}$ concentration. Diffractogram from a hydrothermal reaction, which yielded $\text{Ag}_4\text{V}_2\text{O}_6\text{F}_2$, is shown at the top for comparison. Two dotted lines highlight the disappearance of $\text{Ag}_3\text{VO}_2\text{F}_4$ peaks.

6.3.2 ^{51}V NMR

The role of the extra water for the formation of $\text{Ag}_4\text{V}_2\text{O}_6\text{F}_2$ in lieu of $\text{Ag}_3\text{VO}_2\text{F}_4$ was investigated by ^{51}V NMR. As mentioned in chapter 5, a possible vanadium species in the hydrofluoric acid solution could be the *trans* $[\text{VO}_2\text{F}_4]^{3-}$ octahedra, which was evidenced by a quintet in the ^{51}V NMR spectra. These studies from 48-50% $\text{HF}_{(\text{aq})}$ solutions are relevant to the formation of $\text{Ag}_3\text{VO}_2\text{F}_4$, but there are no literature reports of ^{51}V NMR of V_2O_5 dissolved in

more dilute solutions which would pertain to where $\text{Ag}_4\text{V}_2\text{O}_6\text{F}_2$ is formed. It was, however, shown that the phases of $3\text{VO}_2\text{F}\cdot\text{HF}\cdot\text{H}_2\text{O}$ and $4\text{VOF}_3\cdot 3\text{HF}\cdot 3\text{H}_2\text{O}$ were precipitated from such solutions (see 5.4.1).³⁵ It could therefore be presumed that, by the addition of a fluoride to each vanadium phase, the species in solution could be VO_2F_2^- between 20-42% $\text{HF}_{(\text{aq})}$ and VOF_4^- at higher concentrations, respectively. This makes reasonable sense as the latter species, with either an oxide or water ligand in the sixth octahedral position, is one that was suggested as the species that gave rise to the NMR quintet.

Solutions of V_2O_5 dissolved in solutions of 48-50% $\text{HF}_{(\text{aq})}$ and 7% $\text{HF}_{(\text{aq})}$ were made with the same amount of vanadium oxide and hydrofluoric acid (and water to dilute for the latter concentration) as for any typical reaction. A proper amount of each solution was added to a Teflon NMR tube insert (PTFE-FEP NMR Tube Liner from Wilmad-Labglass) which were inserted into a standard glass NMR tube. A VOCl_3 standard was used in the 400 MHz NMR with variable temperature control. The hydrofluoric acid solutions were evaluated at 15, 10, and 2 °C. The concentrated 48-50% $\text{HF}_{(\text{aq})}$ solution gave singlet with a shift of -781 ppm that broadened from a FWHM of 210 to 344 Hz in cooler temperatures (Figure 6.4a). The dilute 7% $\text{HF}_{(\text{aq})}$ solution gave a quintet with a shift of -775 ppm and a $J_{\text{V-F}}$ split of 112 Hz (Figure 6.4b). These values are in agreement with the literature value of a singlet with a shift of -777 ppm.³⁶ However, at cooler temperatures of 7 and -10 °C, a quintet was reported with a $J_{\text{V-F}}$ split of 112 Hz.^{36,37} By comparison, the NMR for VO_2F_2^- was reported as a triplet at -595 ppm with a $J_{\text{V-F}}$ split of 272 Hz. Results are summarized in Table 6.1.

The significance of the ^{51}V NMR experiments was to show that the vanadium species in solution does not determine the formation of either Ag_3VOF_4 or $\text{Ag}_4\text{V}_2\text{O}_6\text{F}_2$. The NMR spectra

are a singlet and a quintet for 48% and 7% HF_(aq) respectively, which can be explained by the vanadium species in the more concentrated HF_(aq) solution undergoing rapid ligand-solution exchange, thereby removing any coupling between the vanadium and fluorine nuclei. Perhaps the coupling was reported in this concentration at lower temperatures was that their solution was saturated with V₂O₅, but no details were given on how the solution was prepared.

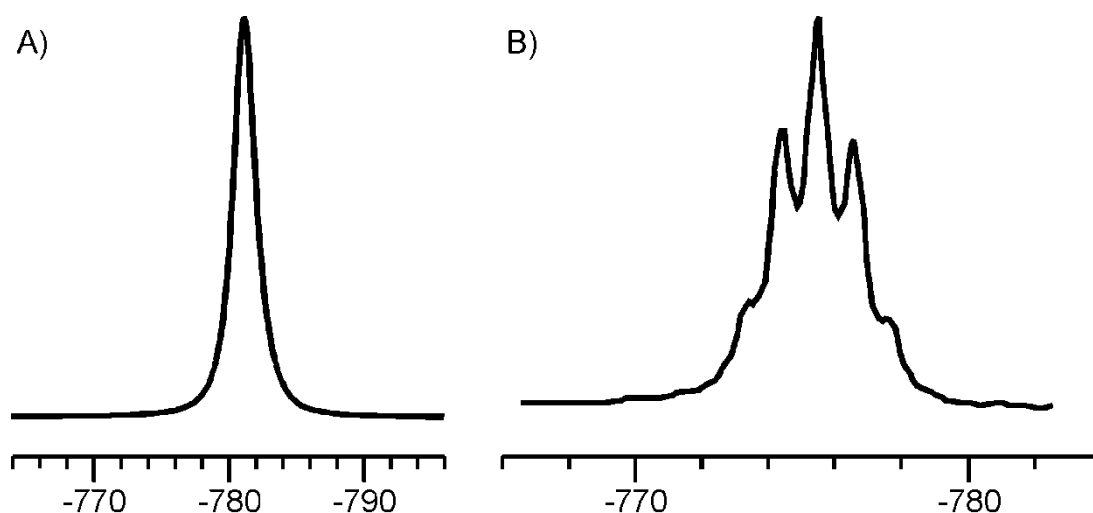


Figure 6.4 ^{51}V NMR of V₂O₅ dissolved in a) 48% and b) 7% hydrofluoric acid.

Table 6.1 Summary of experimental and literature values for ^{51}V NMR of V₂O₅ dissolved in HF_(aq).

	Experimental		Literature	
	7%	48%	48%	48%
HF Solution Concentration	7%	48%	48%	48%
Multiplicity	Quintet	Singlet	Quintet	Singlet
Shift (ppm)	-775	-781	-777	-777
$J_{\text{V-F}}$ (Hz)	112	n/a	112	n/a
Temperature (°C)	2, 10, 15	2, 10, 15	-10, 7	25

6.3.3 Electrochemistry

To evaluate the electrochemical performance of SVOF-RT, it was compared to hydrothermally-made SVO³⁰ and SVOF.^{15,32} This route for SVO preparation yields nano-sized flat needle-like particles of 150-400 nm wide, 1000 nm long and 50 nm thick (Figure 6.1c). Similarly sized particles were recently highlighted to react vs. lithium better than the standard product obtained by a solid state reaction, which gave an improved discharge rate capability.^{12,38} We also report the performance of hydrothermally-made Ag₄V₂O₆F₂ (SVOF-Hyd) particles to demonstrate the benefits of the reduced particle sizes of SVOF-RT.

The Galvanostatic Intermittent Titration Technique (GITT) was used to evaluate the polarization difference between the three materials. The polarization evolution is defined herein as being the potential difference between equilibrium and under current. Cells were discharged at a rate of D/10 (i.e. 1 lithium ion inserted in 10 hours) followed by relaxation for 2 hours. Figure 6.5a shows the thermodynamic discharge curves for SVOF and SVO, highlighting the higher potential for SVOF for the first 168 mAh/g. Also evaluated from this experiment was the difference in polarization during discharge between SVOF materials synthesized from hydrothermal and room temperature conditions (Figure 6.5b). SVOF-RT exhibits a relatively constant polarization of ~ 0.25 V for the first 3 Li inserted, and up to a maximum of 0.44 V at ~3.5 Li; whereas the polarization of SVOF-Hyd increases from 0.3 V to 0.63 V between 1.5 and 3.5 Li inserted. This decrease in polarization during the reduction of silver can be explained by the decreased particle sizes that provide a shorter ion diffusion length inward from the particle edge.¹⁶

Using a low cathodic current equivalent to a D/50 discharge rate (i.e. 1 lithium ion inserted in 50 hours), SVOF-RT is capable of an uptake of electrons and lithium at up to ~ 450

mV higher than the nano-sized SVO for the first 163 mAh/g delivered (Figure 6.5c). This is followed by a threshold at which the cell potential monotonously drops owing to the V^{5+} reduction.¹⁶ At this low discharge rate, SVOF-Hyd performs comparably to SVOF-RT in terms of capacity. Using a discharge rate of 2D (i.e. 1 lithium ion inserted in 30 minutes), the advantages of using SVOF-RT are maintained despite a closer potential gap between these this material and SVO (~ 200 mV for the first 113 mAh/g) (Figure 6.5d). This smaller gap in potentials is a result from the higher ionic limitations in the SVOF Ag^+/Li^+ displacement reaction caused by the less well defined ionic pathways for the silver ion to withdraw.¹⁶ Last, it should be reiterated that at low discharge rate, SVOF-RT performs comparably to SVOF-Hyd in terms of capacity while it is much favorable at a high rate, further emphasizing the importance of particle size.

Numerous electrochemical Swagelok-type cells composed of a similar cathode loading (~20 mg active material on a ~1.23 cm² electrode surface) were discharged at different rates between D/50 to 2D. The energy density vs. power density of each material is gathered in a plot similar to a Ragone plot with cutoff points of (a) 3 V and (b) 2.5 V, below which ICDs start to operate with less efficiency (Figure 6.6). The space domains in the figure were obtained by the repetition of multiple experiments. As a result, two features can be concluded: (i) the decrease of $Ag_4V_2O_6F_2$ particle size by one order of magnitude is beneficial for an increase of both power density and energy density (ii) SVOF-RT compares favorably with nano-sized SVO synthesized from hydrothermal conditions.

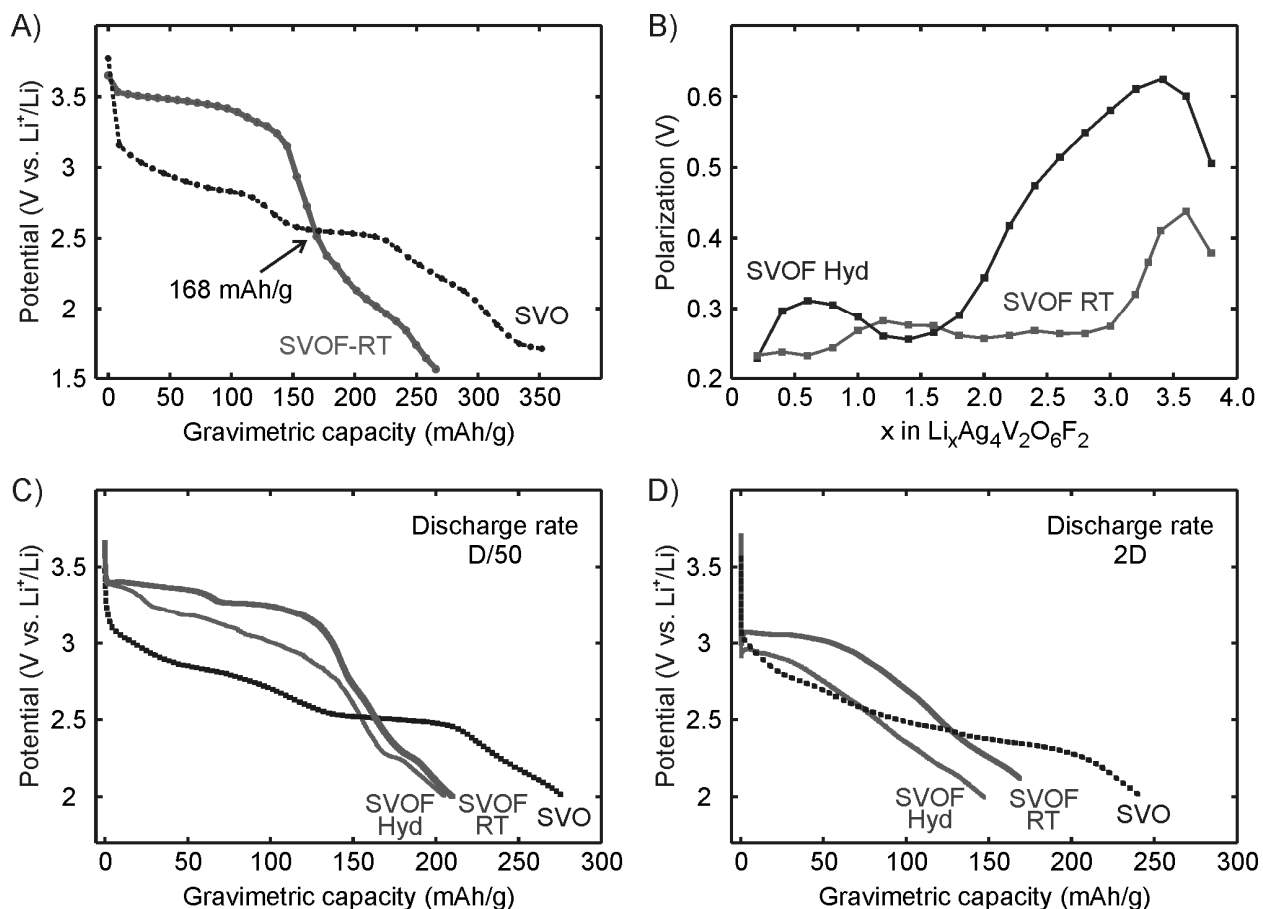


Figure 6.5 Potential vs. gravimetric capacity curves comparing the discharge of $\text{Ag}_4\text{V}_2\text{O}_6\text{F}_2$ material tailored at room temperature (SVOF-RT) and hydrothermal conditions (SVOF-Hyd) and $\text{Ag}_2\text{V}_4\text{O}_{11}$ (SVO) from hydrothermal conditions discharged using (a) Galvanostatic Intermittent Titration Technique (GITT), (b) cathode polarization comparison determined from GITT experiments on SVOF-Hyd and SVOF-RT (c) a discharge rate of D/50, and (d) a discharge rate of 2D.

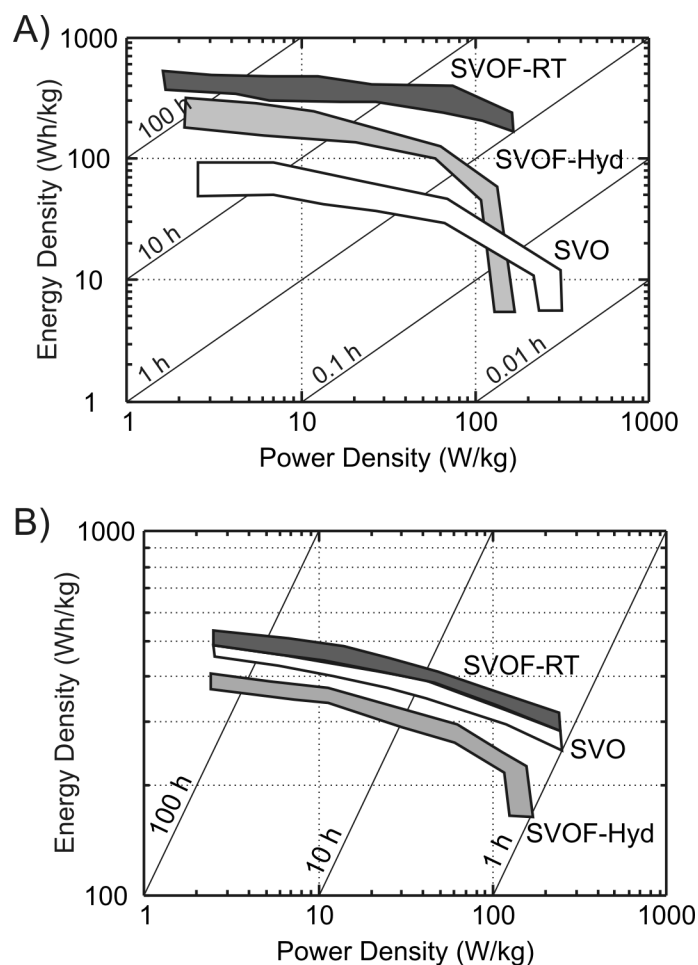


Figure 6.6 Plot comparing energy density vs. power density of cathodes consisting of $\text{Ag}_4\text{V}_2\text{O}_6\text{F}_2$ synthesized at room temperature (SVOF-RT) and at hydrothermal conditions (SVOF-Hyd) and $\text{Ag}_2\text{V}_4\text{O}_{11}$ at hydrothermal reactions, for potentials above 3 and 2.5 V.

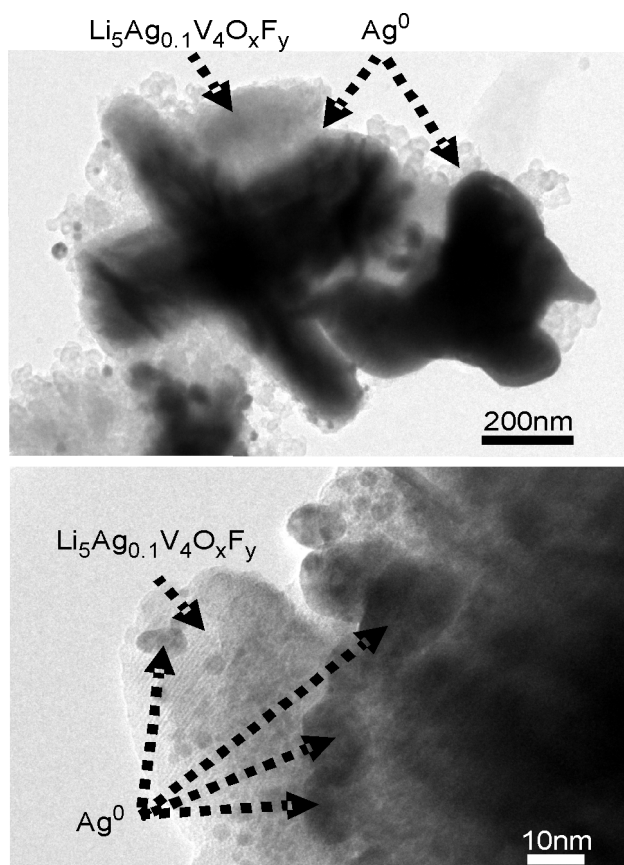


Figure 6.7 TEM micrographs of lithiated $\text{Ag}_4\text{V}_2\text{O}_6\text{F}_2$ showing regions of $\text{Li}_5\text{Ag}_{0.1}\text{V}_4\text{O}_x\text{F}_y$ (light) and Ag metal (dark). Silver metal is on the order of 10 nm in diameter along the particle edges.

Evidence of the silver/lithium displacement reaction arises from TEM investigations on electrochemically discharged samples down to a cut-off potential of *c.a.* 2V (vs. Li^+/Li), which corresponds to the insertion of around 5 Li^+ ion per formula unit. The bright field images in Figure 4 highlight two different contrasts within the particle. The bright parts of the particles are lithiated SVOF. EDAX measurements on this location reveal almost no silver remaining (Ag/V ratio of 0.1/4). The dark zones of the particles correspond to large silver metal regions. Additional HRTEM investigations also clearly emphasize (*i*) the loss of particles crystallinity

making the discharged material amorphous to powder X-ray diffraction (ii) occasional occurrences of a nano-crystallized region of $\text{Li}_5\text{Ag}_{0.1}\text{V}_4\text{O}_x\text{F}_y$ between entire amorphous regions (as pointed by the arrow Figure 6.7) (iii) the presence of nano-clusters of metallic silver around the particle edge (from 3 nm to 15 nm in size).

6.4 Conclusions

In conclusion, the investigation the Ag_2O - V_2O_5 - HF - H_2O system with a Ag:V molar reactant ratio of 4:1 at room temperature has led to the realization of new strategies on low temperature synthesis. Notably unique are the new silver vanadium oxide fluoride, $\text{Ag}_3\text{VO}_2\text{F}_4$, and preparation of the cathode material $\text{Ag}_4\text{V}_2\text{O}_6\text{F}_2$ that shows enhanced electrochemical behavior owing to the smaller particle sizes. This room temperature synthetic route has multiple advantages: a straightforward experimental procedure, a rapid synthesis (~ 1 hour) without complex apparatuses, and it represents a step toward a more environmentally-friendly chemistry. Ongoing efforts are underway to transfer such diverse room-temperature chemistry toward HF-free solution, pursuing a further decrease of particle size and specific shape control, and finding an alternative to vanadium-based cathode materials.

Chapter Seven

Formation of SVOF from 3DOM structure

7.1 Introduction

The morphology of a battery material can affect its discharge properties and thus the design and optimization of the material is a necessity for its commercialization. While the formula / composition and crystal structure of a cathode fundamentally define the maximum energy that can be recovered via reduction in a Li battery, particle size and morphology can play a significant role in determining the recoverable energy. In chapter 3, it was shown that $\text{Ag}_4\text{V}_2\text{O}_6\text{F}_2$ has a significant amount of polarization during the reduction of silver over the insertion of the first four Li. Therefore, it was necessary to synthesize smaller particles to reduce this polarization and improve the discharge profiles. Hence, in chapter 5 we studied room temperature synthesis of SVOF and indeed the smaller particles exhibited beneficial discharge properties at both low and high rates. However, further improvements are desired and the rational design of smaller particles is warranted.

Three dimensionally ordered macroporous materials (3DOM) are an example of a designed material that incorporates high porosity and high surface area. 3DOM materials are synthesized by first infiltrating an ordered template with precursors, which are then reacted together to crystallize a target compound within the voids, and finally followed by removal of the template. An example of the template consists of a cubic close packed array of polymer or silica spheres that provide small interstices for the formation of the desired phase. When this template is removed, a skeleton that resembles a honeycomb is left behind that has theoretical void density of 26% (owing to the packing efficiency of the spheres). The structural stability of the template during the synthesis of 3DOM materials for batteries is not highly important because the end goal is to recover small particles that formed the skeletal walls rather than maintain the honeycomb-like structure.

Materials that have been synthesized to have the 3DOM structure and electrochemically tested as anodes in rechargeable Li-ion batteries include V_2O_5 , SnO_2 , and $Li_4Ti_5O_{12}$.¹⁻³ 3DOM V_2O_5 showed a better rate capability and cycleability compared to its nonporous counterpart; however, the uptake of Li^+ by SnO_2 , which results in a lithium tin alloy, changes the volume of the material by up to 300% and thus leads to the rapid degradation of the 3DOM structure. The volume change for $Li_4Ti_5O_{12}$ upon lithium insertion is around 0.3% and the interaction between the material and the electrolyte is minimal. General advantages of 3DOM architecture are the high surface area (gives an increased contact with the electrolyte and more surface sites for lithium diffusion), a continuous network of fused particles (minimizes overall particle isolation yet maintains the reduced dimensionality), and well defined channels (improves long distance transport and reduces polarization).

The requirements for 3DOM synthesis are *i*) a close packed template, *ii*) the precursors in a solution state that can be reacted into the desired phase, and *iii*) the ability to remove the template without decomposing the product (Figure 7.1). The method used for the synthesis of 3DOM $Li_4Ti_5O_{12}$ will be described as an example of each of these steps. To form the template, surfactant-free emulsion polymerization was used to create non-crosslinked poly(methyl methacrylate) (PMMA) spheres of circa 300 nm. A cubic-close packed arrangement was achieved by centrifuging the spheres after washing them with dilute methanol to remove any unreacted starting materials and impurities. The precursors for the lithium titanate were 1 M solutions of titanium oxalate $H_2TiO(C_2O_4)_2$ and lithium acetate $Li(CH_3COO)$ mixed in a 5:4 ratio by volume, respectively, with no precipitation. The solution was introduced into the 3DOM template and allowed to evaporate to dryness. The left-behind precursors were reacted to form

$\text{Li}_4\text{Ti}_5\text{O}_{12}$ and the polymer spheres were calcined simultaneously in a furnace heated to 675°C for 6 hours. In the photonics community, a template of silica spheres was etched by a weak hydrofluoric acid solution.^{4,5} The importance of this concept will be realized later.

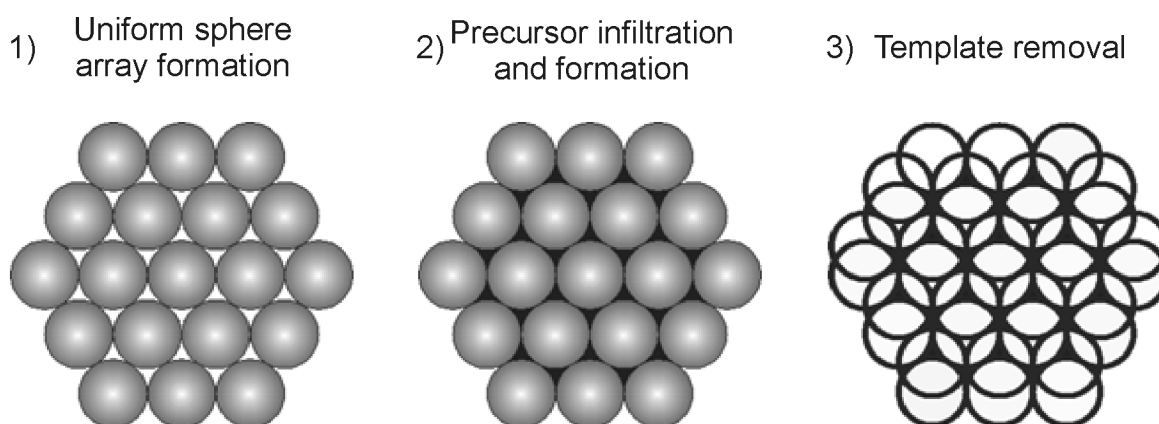


Figure 7.1 Schematic diagram of the synthesis of a material from a 3DOM template.

Before 3DOM $\text{Ag}_4\text{V}_2\text{O}_6\text{F}_2$ could be synthesized, a few obstacles needed to be overcome. The first obstacle was to find a precursor solution that would form SVOF. $\text{Ag}_4\text{V}_2\text{O}_6\text{F}_2$ was possibly present in the solution phase during the exploration of the $\text{Ag}_2\text{O}-\text{V}_2\text{O}_5-\text{HF}_{(\text{aq})}$ composition space, but was not observed as the reactions were performed in a steel autoclave. However, SVOF could be formed by the reaction of water with $\text{Ag}_3\text{VO}_2\text{F}_4$, a phase that can be formed from a mixed solution of silver and vanadium. The second obstacle to overcome was the removal of the template. Obviously, in the reactions studied, a concentrated $\text{HF}_{(\text{aq})}$ solution is used and silica spheres would not be acceptable. PMMA spheres could be used, but their removal by calcination would not be appropriate as the high temperatures needed would decompose the desired silver vanadium oxide fluoride phase. Therefore, the aforementioned method of etching/dissolving the template could thus be utilized by dissolving the template with an organic solvent that would also leave the target compound intact.

7.2 Synthesis and Characterization

7.2.1 Materials

Caution. Hydrofluoric acid is toxic and corrosive and must be handled with extreme caution and the appropriate protective gear! If contact with the liquid or vapor occurs, proper treatment procedures should be followed immediately.⁶⁻⁸

Materials. Ag_2O (99.9%, Fisher), V_2O_5 (99.6%, Alfa-Aesar), and aqueous hydrofluoric acid (48-50% HF by weight, Fisher) were used as received. PMMA spheres were used as received from a prior synthesis.

7.2.2 Synthesis

Precursor Synthesis. The silver- and vanadium-containing solution was synthesized from 0.3970 g (1.713×10^{-3} mol) of Ag_2O , 0.1039 g (5.713×10^{-4} mol) of V_2O_5 , and 0.5470 g of $\text{HF}_{(\text{aq})}$ (1.340×10^{-2} mol HF) placed into a Teflon [fluoro(ethylene-propylene)] pouch. This pouch was manually agitated to fully dissolve the oxides to eventually yield a clear yellow solution at room temperature. The ratio of Ag:V in this reaction is 3:1 for the desired $\text{Ag}_3\text{VO}_2\text{F}_4$. The difference between this reaction and the one discussed in chapter 5 (with a 4:1 ratio) to form the same phase will be discussed later.

3DOM Formation. To the pouch that contained the precursor solution, around 1.5 g of PMMA spheres were added, or enough to “soak up” the solution. The initially white spheres were turned yellow by the solution, and in some areas a reddish color could be observed. The reaction pouch was then heat sealed and placed into a hot water bath of 100 °C to fully precipitate the red $\text{Ag}_3\text{VO}_2\text{F}_4$ phase. After 5 minutes, the pouch was removed from the hot water and immediately cut open and filtered to dry any remaining hydrofluoric acid solvent. The

3DOM $\text{Ag}_3\text{VO}_2\text{F}_4$ and PMMA template were then placed in a beaker with 50 mL chloroform, or enough to sufficiently dissolve the template, and stirred for at least two hours. The solution was allowed to settle and then decanted. The remaining solution and precipitate were then washed with water in the same beaker to react $\text{Ag}_3\text{VO}_2\text{F}_4$ to make the target $\text{Ag}_4\text{V}_2\text{O}_6\text{F}_2$.

7.2.3 Characterization

Powder X-ray Diffraction. Powder X-ray diffraction patterns were collected on a Rigaku XDS 2000 with Ni filtered Cu $K\alpha$ radiation ($\lambda = 1.5418 \text{ \AA}$) and compared with patterns recorded in the JCPDS (Joint Committee of Powder Diffraction Standards) database and with patterns collected from previous room-temperature and hydrothermal syntheses of silver vanadium oxide fluorides.

Electron Microscopy. Transmission electron microscopy was performed on a Hitachi H-8100 TEM with an accelerating voltage of 200 kV and an emission current of 30 mA. TEM samples were sonicated in acetone for 5 minutes and dispersed on a holey carbon grid.

7.3 Discussion

The motivation for synthesis of SVOF from the 3DOM template arose from the desire to synthesize even smaller particles to reduce further the polarization discussed in previous chapters. It was shown that a significant amount of polarization, between 400 and 600 mV, exists during the reduction of silver in $\text{Ag}_4\text{V}_2\text{O}_6\text{F}_2$ by lithium metal. Attempts to make particles smaller than the ones first studied, which were 10 μm after manually grinding, led to the room temperature synthetic route that formed particles with dimensions decreased by an order of magnitude. Consequently, the polarization decreased by up to 300 mV over the course of silver reduction. However, there was a constant polarization present throughout the discharge of at

least 200 mV. Therefore a further decrease of particle dimensions by an order of magnitude could lead to a reduction of this “base” polarization as well as prevent the increased polarization between 3 and 4 Li inserted. Hence, ~300 nm 3DOM spheres were chosen owing to the dimensions of the voids. In two dimensions, a close packed lattice of circles with a diameter of 300 nm would have a maximum void width of about 120 nm. This is ideal for this study as it would provide the order of magnitude difference compared to particles synthesized from room temperature.

The process for the formation of 3DOM-templated SVOF involves five steps: synthesis of a precursor solution, infiltration of the 3DOM structure, formation of $\text{Ag}_3\text{VO}_2\text{F}_4$, removal of the template, and reaction of $\text{Ag}_3\text{VO}_2\text{F}_4$ to $\text{Ag}_4\text{V}_2\text{O}_6\text{F}_2$. While the first, third, and last steps have been discussed in previous chapters, the reaction set up was different, which altered the method for synthesis of SVOF. In addition, the third step of template removal was realized from a similar system with silica spheres but adapted to the present system with PMMA spheres.

7.3.1 Precursor Solution.

The initial discovery and optimal synthesis of $\text{Ag}_3\text{VO}_2\text{F}_4$ was made from a reaction between a 4:1 ratio of Ag_2O and V_2O_5 dissolved in $\text{HF}_{(\text{aq})}$. The excess of silver was needed due to its higher relative solubility and was thus more likely to remain in solution instead of precipitate as the silver vanadium oxide fluoride. Therefore, the initial precursor solution was prepared with a 4:1 Ag:V ratio. As the reaction steps were processed, it appeared that the $\text{HF}_{(\text{aq})}$ solution was absorbed by the PMMA spheres to a point where it appeared the spheres could be called damp rather than in solution. After removal of the template (without the fourth step of a water wash) the sample that remained was characterized by powder X-ray diffraction. The

phases present were the desired $\text{Ag}_3\text{VO}_2\text{F}_4$ with a significant amount of AgF. Therefore, it followed that a reaction with less silver should reduce the amount of AgF observed as the excess silver from the 4:1 Ag:V reaction precipitated as silver fluoride. A reaction with a stoichiometric 3:1 ratio yielded $\text{Ag}_3\text{VO}_2\text{F}_4$ without a trace of AgF. While the amount of silver was reduced for this reaction, the quantity of $\text{HF}_{(\text{aq})}$ was not lowered in conjunction. Less hydrofluoric acid would make the precursor solution more difficult to dissolve, but still be possible. However, as it appears the hydrofluoric acid is absorbed during the infiltration step, the excess over what is necessary to create a slightly unsaturated solution is probably not a factor.

7.3.2 Template infiltration.

The next step is to infiltrate the template with the precursor solution. For this, an amount of 3DOM PMMA spheres was added to the precursor solution to absorb it. The spheres initially were centimeter-sized chunks, but were broken up manually in the reaction pouch to increase its surface area to absorb more rapidly and also that it would conform better in the pouch. This method appeared to work well in that the solution turned the majority of the white PMMA to yellow and left only a marginal amount of spheres unchanged. Also during this step, some of the yellow areas turned red, which indicates that the $\text{Ag}_3\text{VO}_2\text{F}_4$ phase started to form. The amount of template that is actually filled was very low, as estimated from SVOF yield. Future work should concentrate on the development of this step as there are more elaborate and efficient methods to template infiltration. For instance, if the spheres were placed under vacuum first, then the introduced precursor solution would not need to displace the volume of air within the voids. This has been performed for the infiltration of V_2O_5 into PMMA.¹ In a similar manner, the template could be placed in a Buchner funnel and the precursor solution could be pulled into the template

by vacuum. Yet another effective method is to wet the spheres with methanol as in the process to synthesize template $\text{Li}_4\text{Ti}_5\text{O}_{12}$.² A completely different approach is to change the spheres either by a different preparation or even use a different material. Many of these factors could be investigated to improve the formation of 3DOM-templated SVOF.

7.3.3 $\text{Ag}_3\text{VO}_2\text{F}_4$ formation within the template

The third step toward the formation of $\text{Ag}_4\text{V}_2\text{O}_6\text{F}_2$ from a 3DOM template is to precipitate $\text{Ag}_3\text{VO}_2\text{F}_4$ within the voids between PMMA spheres. As mention above, this process started in the slightest upon introduction of the PMMA to the precursor solution. To complete this process, the reaction pouch was placed into a water bath already at a boil. The PMMA that was yellow from the precursor solution changed to a strong red-orange color nearly throughout the reaction pouch. While the pouch could also be placed in the bath and then slowly heated, the faster precipitation was utilized to try to grow the smallest crystallites possible. Additionally, it could be interesting to observe the reversibility of the formation of $\text{Ag}_3\text{VO}_2\text{F}_4$ as discussed in chapter 5 upon cooling.

7.3.4 Template removal

The fourth step of template removal was accomplished by dissolving the polymer in chloroform. The solution that forms is more viscous than water but not too viscous that it could not be stirred well. The red $\text{Ag}_3\text{VO}_2\text{F}_4$ fell to the bottom of the beaker rapidly after stirring stopped. When trying to filter this solution, the dissolved polymer stopped up the filter paper quickly. Therefore, the solution was allowed to settle so that it could be decanted. While some of the dispersed $\text{Ag}_3\text{VO}_2\text{F}_4$ was lost during this process, the majority of it was recovered as not all the chloroform was removed. For some procedures, this final solution was filtered, albeit slowly,

to recover the product for analysis. It was at this step that powder X-ray diffraction showed that AgF was present from reactions that started with a 4:1 Ag:V ratio and led to the revised reactant ratio of 3:1.

Two other solvents that were selected to try to dissolve the PMMA were acetone and a 7:3 by volume mixture of acetonitrile and water. The latter was successful but slower than the chloroform solvent. Acetone as the solvent dissolved PMMA much more slowly than either of the other two solvent systems and thus needed to be stirred for 24 hours. Neither of these two systems yielded a solution that was easier to filter. Therefore, chloroform was the solvent of choice, but better solvent systems should be investigated in the near future as well. With any solvent system, vigorous stirring was imperative as the PMMA preferred to stick to the bottom and sides of the glass beaker.

7.3.5 $\text{Ag}_4\text{V}_2\text{O}_6\text{F}_2$ formation

Once it was confirmed that $\text{Ag}_3\text{VO}_2\text{F}_4$ was formed phase pure up to this point, its reaction with water would yield $\text{Ag}_4\text{V}_2\text{O}_6\text{F}_2$. Two methods for this were attempted. The first method was attempted before the template was dissolved. That is, water was added to the PMMA / $\text{Ag}_3\text{VO}_2\text{F}_4$ mixture in an effort to transform the oxide fluoride into SVOF. However, powder X-ray diffraction of this PMMA/oxide fluoride mixture showed the presence of both $\text{Ag}_3\text{VO}_2\text{F}_4$ and $\text{Ag}_4\text{V}_2\text{O}_6\text{F}_2$. The second method worked better: a two-step process of first decanting the chloroform solution and then adding water to the remaining precipitate / chloroform solution. This solution was more easily filtered and provided a resulting orange precipitate that was indicative of $\text{Ag}_4\text{V}_2\text{O}_6\text{F}_2$ formation, but needed to be characterized.

7.3.6 Characterization

Grinding the sample for powder X-ray diffraction was greatly different from grinding SVOF formed from hydrothermal conditions, however. Where the large crystals from the latter synthesis were large and felt course to grind, the former was very smooth and little change was observed between the as-made and post-grinding sample. Despite the favorable appearance of the material, it was amorphous to X-ray diffraction.

To investigate the particle size, TEM studies were undertaken. The majority of the particles were around 100 - 200 nm in diameter (Figure 7.2). The particles were also mostly amorphous to electron diffraction. It was hoped that the particles would exhibit a honeycomb-like structure – if not in the long range then in the short range. But, it was very encouraging to see that the particle sizes were an order of magnitude less than what was achieved from room temperature synthesis of $\text{Ag}_4\text{V}_2\text{O}_6\text{F}_2$.

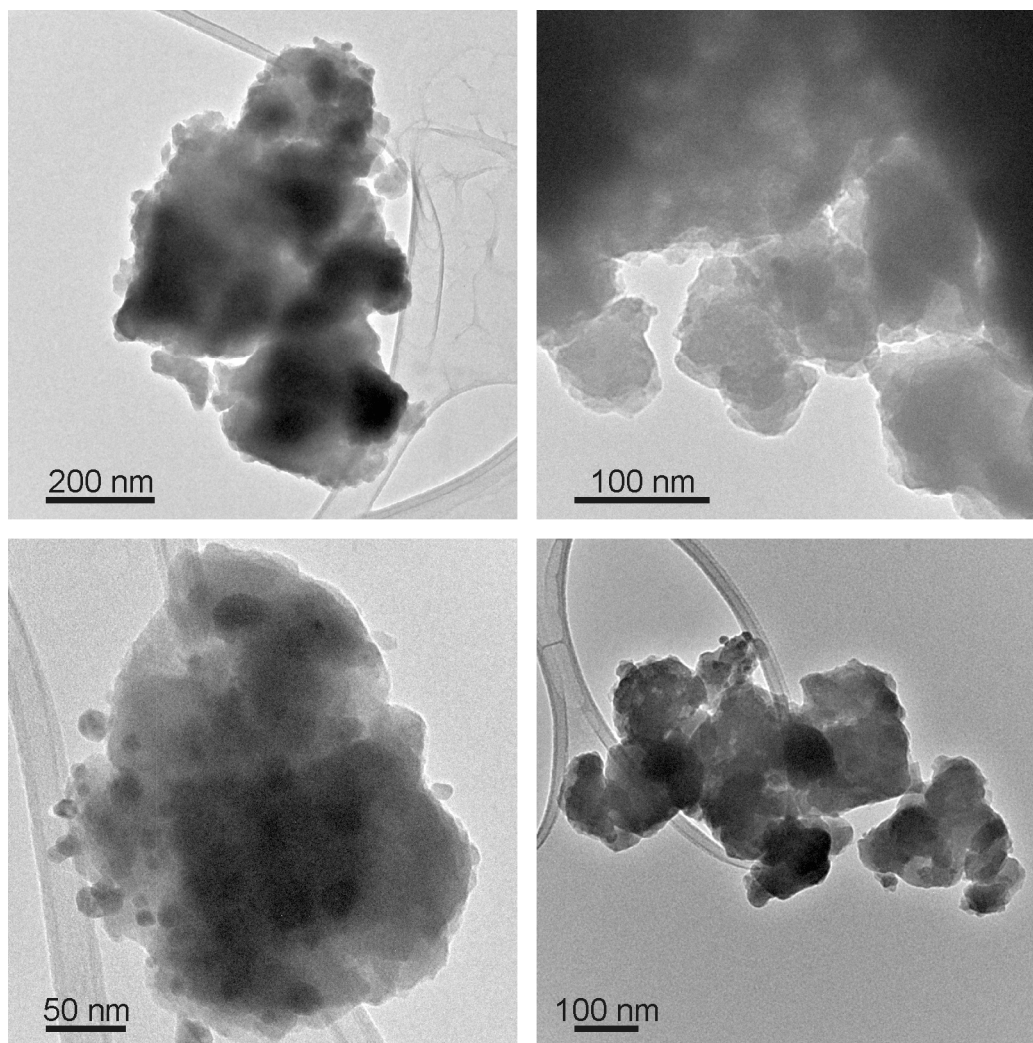


Figure 7.2 TEM micrographs of as recovered product from $\text{Ag}_3\text{VO}_2\text{F}_4$ formed in 3DOM template washed with water.

7.4 Conclusions

The synthetic process to form three dimensionally ordered $\text{Ag}_4\text{V}_2\text{O}_6\text{F}_2$ has been outlined and begun to be implemented. The preliminary work shows promising results of much smaller particles than those made at room temperature. Of the multi-step process, it has been shown that $\text{Ag}_3\text{VO}_2\text{F}_4$ can be prepared within the 3DOM PMMA structure. A plethora of future work can be done with this project and areas to investigate have been discussed above. Eventually, enough

material should be synthesized to be evaluated within a lithium battery. What is hoped to be seen in such a battery with this material is a greater decrease of polarization owing to the smaller particle sizes.

Chapter Eight

Conclusions

8.1 Conclusions

8.1.1 Exploration of Ag_2O - V_2O_5 - $\text{HF}_{(\text{aq})}$ composition space

The discovery of the first silver vanadium oxide fluoride $\text{Ag}_4\text{V}_2\text{O}_6\text{F}_2$ warranted the exploration of the composition space between Ag_2O and V_2O_5 in hydrofluoric acid. The formation of $\text{Ag}_2\text{V}_4\text{O}_{11}$, $\beta\text{-AgVO}_3$, $\text{Ag}_4\text{V}_2\text{O}_7$, $\text{Ag}_4\text{V}_2\text{OF}_2$, and $\alpha\text{-Ag}_3\text{VO}_4$ was outlined under hydrothermal conditions between 150 and 200 °C. Trends observed were the relationship between relative Ag and V solubilities and the phases formed, and the role of hydrofluoric acid. While no other silver vanadium oxide fluoride was discovered under these conditions, the groundwork was laid for further discoveries and developments within this system. That is, the relationship between $\text{Ag}_4\text{V}_2\text{O}_7$ and $\text{Ag}_4\text{V}_2\text{O}_6\text{F}_2$ would later lead to the realization of a new silver vanadium oxide fluoride.

8.1.2 In-depth electrochemical study of $\text{Ag}_4\text{V}_2\text{O}_6\text{F}_2$

Initial electrochemical characterization of $\text{Ag}_4\text{V}_2\text{O}_6\text{F}_2$ as a cathode in a primary lithium battery was very encouraging. To study the discharge curve more closely, in situ X-ray diffraction, TEM, and EPR were performed on the cathode during various states of discharge. The first region of the material to be reduced was almost all four equivalents of silver, followed by reduction of V^{5+} . The reduced silver metal formed long dendritic structures and nanoparticles. A significant polarization was observed during the reduction of silver owing to the poor insertion kinetics of the material. This encouraged a second branch of research to synthesize smaller particles that would exhibit better kinetics and lower polarization.

8.1.3 Discovery of $\text{Ag}_3\text{VO}_2\text{F}_4$

The previously observed relationship between $\text{Ag}_4\text{V}_2\text{O}_7$ and $\text{Ag}_4\text{V}_2\text{O}_6\text{F}_2$ led to the development of a synthesis of a new silver vanadium oxide fluoride $\text{Ag}_3\text{VO}_2\text{F}_4$. The hydrolysis of SVOF to form the pyrovanadate $\text{Ag}_4\text{V}_2\text{O}_7$ from 150 to 200 °C was not only minimized but eliminated. That is, the water that enters the reaction pouch under reaction conditions, which was hydrolyzing the new silver vanadium oxide fluoride phase $\text{Ag}_3\text{VO}_2\text{F}_4$, was circumvented and thus the latter phase was formed. In addition, it was realized that this phase was formed immediately upon addition of $\text{HF}_{(\text{aq})}$ to an appropriate mixture of Ag_2O and V_2O_5 . Unfortunately, this phase with a greater silver density and greater fluoride content when constructed into a cathode behaved like a salt in the electrolyte solution and ion exchanged; therefore, its electrochemistry was not favorable. The growth of a good quality crystal for single crystal X-ray diffraction was difficult and led to the next stage of investigation. In addition, the fact that this phase could be synthesized at room temperature also led to an important development.

8.1.4 Negative temperature coefficient of solubility of $\text{Ag}_3\text{VO}_2\text{F}_4$

A very unusual property of $\text{Ag}_3\text{VO}_2\text{F}_4$ was realized that allowed the growth of better quality crystals. When the Ag_2O and V_2O_5 reagents are fully dissolved in aqueous HF, yet the solution is near saturation, an increase in temperature will precipitate $\text{Ag}_3\text{VO}_2\text{F}_4$. This process was reversible whereby upon cooling the precipitate would dissolve. When the solution was slowly heated over the course of many hours, crystal growth was favored. This phenomena, a negative temperature coefficient of solubility, was explained in terms of the properties of HF changing with an increased temperature and the in terms of thermodynamics affecting the waters or hydrofluoride of crystallization by influencing the entropy term in Gibb's free energy.

8.1.5 Room temperature synthesis of $\text{Ag}_4\text{V}_2\text{O}_6\text{F}_2$

The combined desire to synthesize smaller particles of $\text{Ag}_4\text{V}_2\text{O}_6\text{F}_2$ and to expand knowledge of synthetic chemistry led to the success of making the first cathode material for a primary lithium battery at room temperature. From the combined ideas of the synthesis of $\text{Ag}_3\text{VO}_2\text{F}_4$ at room temperature and the hydrolysis of the latter phase to form $\text{Ag}_4\text{V}_2\text{O}_6\text{F}_2$, this accomplishment yielded particles an order of magnitude smaller than those achieved from hydrothermal synthesis and manual grinding (1 μm vs. 10 μm). Indeed, the smaller particles exhibited a lower cathode polarization throughout the duration of silver reduction. The straightforward rapid synthesis has opened the door toward more energy-efficient solid state chemistry of mixed metal oxide fluorides, in specific those with a high silver density.

8.1.6 Formation of 3DOM $\text{Ag}_4\text{V}_2\text{O}_6\text{F}_2$

The culmination of the chemistry of silver vanadium oxide fluorides from hydrofluoric acid solutions led toward the specific template synthesis of $\text{Ag}_4\text{V}_2\text{O}_6\text{F}_2$. Three dimensionally ordered macroporous PMMA was used to template the formation of SVOF. The precursor solution, which first exhibited the reversibility of $\text{Ag}_3\text{VO}_2\text{F}_4$ formation, was utilized for infiltration of the 3DOM template. Template removal was rather efficient and successful, however evaluation of the final phase recovered after washing with water could not confirm the phase $\text{Ag}_4\text{V}_2\text{O}_6\text{F}_2$, nor was the long range structure maintained. However, particle sizes were between 100 to 200 nm and therefore should exhibit less polarization as a cathode.

8.2 Future Directions

8.2.1 Exploration of other mixed metal oxide fluorides

Hydrothermal synthesis continues to be an attractive method for the formation of mixed metal oxide fluorides owing to the soft chemistry and ability to grow single crystals. While the $\text{Ag}_2\text{O-V}_2\text{O}_5$ system in aqueous HF has been expanded, ventures into systems between Ag_2O and other metal oxides such as TiO_2 , ZrO_2 , Nb_2O_5 , Ta_2O_5 , and WO_3 could lead toward similar systems, or reveal drastically different phases that can be formed in one system and not the other. Especially exciting is the prospect of room temperature synthesis and crystal growth techniques of silver metal oxide fluorides or alkali metal oxide fluorides or of mixtures thereof. Hydrofluoric acid concentration is imperative for the possibility of formation of higher fluoride species; it was very apparent from the $\text{Ag}_3\text{VO}_2\text{F}_4$ discovery that higher fluorides will easily hydrolyze in more dilute solutions. And finally, as the discovery of more oxide fluoride materials are made, electrochemical characterization should follow and perhaps trends can be found as to different reactivity of metals within similar structure-types.

8.2.2 Development of templated SVOF synthesis

Much groundwork has been laid for the processing of $\text{Ag}_4\text{V}_2\text{O}_6\text{F}_2$ into an ordered macroporous material. An important point to realize is that $\text{Ag}_3\text{VO}_2\text{F}_4$ is an intermediate phase for the synthesis of $\text{Ag}_4\text{V}_2\text{O}_6\text{F}_2$. Therefore, to target any specialized formation of SVOF, the synthesis should be tailored toward first the formation of $\text{Ag}_3\text{VO}_2\text{F}_4$ and flexible enough to allow a reaction of the resultant material with water. Other templates or particle control techniques should be attempted to form smaller particles to evaluate the polarization and electrochemical capacity of such materials.

References

Chapter 1

1. Keister, P.; Mead, R. T.; Ebel, S. J.; Fairchild, W. R., *Proc. Power Sources Symp.* **1984**, 31st, 331-8.
2. Takeuchi, E. S.; Quattrini, P. J.; Greatbatch, W., *Pacing Clin Electrophysiol* **1988**, 11, (11 Pt 2), 2035-9.
3. Takeuchi, E. S.; Thiebolt, W. C., III, *J. Electrochem. Soc.* **1988**, 135, (11), 2691-4.
4. Leising, R. A.; Takeuchi, E. S., *Chem. Mater.* **1993**, 5, (5), 738-42.
5. Crespi, A. M. US Patent 5,221,453, June 22, 1993.
6. Takeuchi, K. J.; Marschilok, A. C.; Davis, S. M.; Leising, R. A.; Takeuchi, E. S., *Coord. Chem. Rev.* **2001**, 219, 283-310.
7. Brodd, R. J.; Bullock, K. R.; Leising, R. A.; Middaugh, R. L.; Miller, J. R.; Takeuchi, E., *J. Electrochem. Soc.* **2004**, 151, (3), K1-K11.
8. Izumi, H. K.; Sorensen, E. M.; Vaughey, J. T.; Poeppelmeier, K. R. US Provisional Patent 60/606,475, September 1, 2004.
9. Sorensen, E. M.; Izumi, H. K.; Vaughey, J. T.; Stern, C. L.; Poeppelmeier, K. R., *J. Am. Chem. Soc.* **2005**, 127, (17), 6347-6352.
10. Harrison, W. T. A.; Nenoff, T. M.; Gier, T. E.; Stucky, G. D., *Inorg. Chem.* **1993**, 32, (11), 2437-2441.

Chapter 2

1. Norquist, A. J.; Heier, K. R.; Stern, C. L.; Poeppelmeier, K. R., *Inorg. Chem.* **1998**, 37, (25), 6495-6501.
2. Norquist, A. J.; Heier, K. R.; Halasyamani, P. S.; Stern, C. L.; Poeppelmeier, K. R., *Inorg. Chem.* **2001**, 40, (9), 2015-2019.

3. Maggard, P. A.; Nault, T. S.; Stern, C. L.; Poeppelmeier, K. R., *J. Solid State Chem.* **2003**, 175, (1), 27-33.
4. Sorensen, E. M.; Izumi, H. K.; Vaughey, J. T.; Stern, C. L.; Poeppelmeier, K. R., *J. Am. Chem. Soc.* **2005**, 127, (17), 6347-6352.
5. Izumi, H. K.; Sorensen, E. M.; Vaughey, J. T.; Poeppelmeier, K. R. US Provisional Patent 60/606,475, September 1, 2004.
6. Liang, C. C.; Bolster, M. E.; Murphy, R. M. US Patent 4,310,609, January 12, 1982.
7. Liang, C. C.; Bolster, M. E.; Murphy, R. M. US Patent 4,391,729, July 5, 1983.
8. Takeuchi, K. J.; Marschilok, A. C.; Davis, S. M.; Leising, R. A.; Takeuchi, E. S., *Coord. Chem. Rev.* **2001**, 219, 283-310.
9. Mao, C.; Wu, X.; Pan, H.; Zhu, J.; Chen, H., *Nanotechnology* **2005**, 16, (12), 2892-2896.
10. Liu, Y.; Zhang, Y.; Hu, Y.; Qian, Y., *Chem. Lett.* **2005**, 34, (2), 146-147.
11. Britton, H. T. S.; Robinson, R. A., *J. Chem. Soc., Abstr.* **1930**, 2328-43.
12. Konta, R.; Kato, H.; Kobayashi, H.; Kudo, A., *Phys. Chem. Chem. Phys.* **2003**, 5, 3061-3065.
13. Fleury, P.; Kohlmuller, R., *C. R. Acad. Sci. Ser. C* **1966**, 262, (6), 475-7.
14. Kittaka, S.; Matsuno, K.; Akashi, H., *J. Solid State Chem.* **1999**, 142, 360-367.
15. Rozier, P.; Savariault, J.-M.; Galy, J., *J. Solid State Chem.* **1996**, 122, (2), 303-8.
16. Masse, R.; Averbuch-Pouchot, M. T.; Durif, A.; Guitel, C., *Acta Cryst. C* **1983**, 39, 1608-1610.
17. Onoda, M.; Kanbe, K., *J. Phys.: Condens. Matter* **2001**, 13, (31), 6675-6685.
18. Raveau, B., *Rev. Chim. Miner.* **1967**, 4, (3), 729-58.
19. Dinnebier, R. E.; Kowalevsky, A.; Reichert, H.; Jansen, M., *Z. Kristallogr.* **2007**, 222, (8), 420-426.

20. Kittaka, S.; Nishida, S.; Ohtani, T., *J. Solid State Chem.* **2002**, 169, 139-142.
21. Takeuchi, E. S.; Leising, R. A.; Hong, G.; Rubino, R. US Patent Application 2004185346, September 23, 2004.
22. Bertolini, J. C., *J. Emerg. Med.* **1992**, 10, (2), 163-168.
23. Segal, E. B., *Chem. Health Saf.* **2000**, 7, (1), 18-23.
24. Peters, D.; Miethchen, R., *J. Fluorine Chem.* **1996**, 79, (2), 161-165.
25. Harrison, W. T. A.; Nenoff, T. M.; Gier, T. E.; Stucky, G. D., *Inorg. Chem.* **1993**, 32, (11), 2437-2441.
26. *SAINT-Plus*, version 6.02A; Bruker Analytical X-ray Instruments, Inc.: Madison, WI, 2000.
27. Sheldrick, G. M. *SHELXTL*, version 5.10; Bruker Analytical X-Ray Instruments, Inc.: Madison, WI, 1997.
28. Kristallov, L. V.; Volkov, V. L.; Perelyaeva, L. A., *Russ. J. Inorg. Chem.* **1990**, 35, (7), 1031-1034.
29. Jansen, M., *Angew. Chem.* **1987**, 99, (11), 1136-49.
30. Viswanathan, A.; Suthanthiraraj, S. A. In *Preparation and transport properties of the fast ionic system CuI-Ag₃VO₄*, Solid State Ionics: New Developments, [Proceedings of the Asian Conference], 5th, Kandy, Sri Lanka, Dec. 2-7, 1996, 1996; Chowdari, B. V. R.; Dissanayake, M. A. K. L.; Careem, M. A., Eds. World Scientific: Singapore: Kandy, Sri Lanka, 1996; pp 447-452.
31. Mishchenko, A. V.; Krasnova, T. M.; Yaufman, A. P., *J. Electroceram.* **1979**, 3, 92-3.
32. Olazcuaga, R.; Reau, J. M.; LeFlem, G.; Hagenmuller, P., *Z. Anorg. Allg. Chem.* **1975**, 412, (3), 271-80.
33. Stomberg, R., *Acta Chem. Scand.* **1963**, 17, (6), 1563-6.
34. Kittaka, S.; Nishida, S.; Iwashita, T.; Ohtani, T., *J. Solid State Chem.* **2002**, 164, (1), 144-149.

35. Barthelet, K.; Riou, D.; Ferey, G., *Solid State Sci.* **2001**, 3, (1-2), 203-209.
36. Hu, J. Q.; Deng, B.; Zhang, W. X.; Tang, K. B.; Qian, Y. T., *Int. J. Inorg. Mater.* **2001**, 3, (7), 639-642.
37. Sheets, W. C.; Mugnier, E.; Barnabe, A.; Marks, T. J.; Poeppelmeier, K. R., *Chem. Mater.* **2006**, 18, (1), 7-20.
38. Bertoni, M. I.; Kidner, N. J.; Mason, T. O.; Albrecht, T. A.; Sorensen, E. M.; Poeppelmeier, K. R., *J. Electroceram.* **2007**, 18, (3-4), 189-195.

Chapter 3

1. Crespi, A. M.; Somdahl, S. K.; Schmidt, C. L.; Skarstad, P. M., *J. Power Sources* **2001**, 96, (1), 33-38.
2. Gomadam, P. M.; Brown, J.; Scott, E. R.; Schmidt, C. L., Abstract #383. In *211th ECS meeting*, Chicago (USA), May 2006.
3. Takeuchi, K. J.; Marschilok, A. C.; Davis, S. M.; Leising, R. A.; Takeuchi, E. S., *Coord. Chem. Rev.* **2001**, 219, 283-310.
4. Onoda, M.; Kanbe, K., *J. Phys.: Condens. Matter* **2001**, 13, (31), 6675-6685.
5. Lee, J.-W.; Popov, B. N., *J. Power Sources* **2006**, 161, (1), 565-572.
6. Sorensen, E. M.; Izumi, H. K.; Vaughey, J. T.; Stern, C. L.; Poeppelmeier, K. R., *J. Am. Chem. Soc.* **2005**, 127, (17), 6347-6352.
7. Albrecht, T. A.; Stern, C. L.; Poeppelmeier, K. R., *Inorg. Chem.* **2007**, 46, (5), 1704-1708.
8. Izumi, H. K.; Sorensen, E. M.; Vaughey, J. T.; Poeppelmeier, K. R. US Provisional Patent 60/606,475, September 1, 2004.
9. Bertolini, J. C., *J. Emerg. Med.* **1992**, 10, (2), 163-168.
10. Segal, E. B., *Chem. Health Saf.* **2000**, 7, (1), 18-23.
11. Peters, D.; Miethchen, R., *J. Fluorine Chem.* **1996**, 79, (2), 161-165.

12. Harrison, W. T. A.; Nenoff, T. M.; Gier, T. E.; Stucky, G. D., *Inorg. Chem.* **1993**, 32, (11), 2437-2441.
13. Roisnel, T.; Rodriguez-Carjaval, J. *Fullprof*, version Dec 2005; France, 2005.
14. Garcia-Alvarado, F.; Tarascon, J. M., *Solid State Ionics* **1994**, 73, (3,4), 247-54.
15. Kawakita, J.; Makino, K.; Katayama, Y.; Miura, T.; Kishi, T., *J. Power Sources* **1998**, 75, (2), 244-250.
16. West, K.; Crespi, A. M., *J. Power Sources* **1995**, 54, (2), 334-7.
17. Beninati, S.; Fantuzzi, M.; Mastragostino, M.; Soavi, F., *J. Power Sources* **2006**, 157, (1), 483-487.
18. Crespi, A. M.; Skarstad, P. M.; Zandbergen, H. W., *J. Power Sources* **1995**, 54, (1), 68-71.
19. Ramasamy, R. P.; Feger, C.; Strange, T.; Popov, B. N., *J. Appl. Electrochem.* **2006**, 36, (4), 487-497.
20. Shannon, R. D., *Acta Crystallogr. Sect. A* **1976**, A32, (5), 751-67.
21. Morcrette, M.; Rozier, P.; Dupont, L.; Mugnier, E.; Sannier, L.; Galy, J.; Tarascon, J. M., *Nat. Mater.* **2003**, 2, (11), 755-761.
22. Taillades, G.; Sarradin, J., *J. Power Sources* **2004**, 125, (2), 199-205.
23. Bharathi Mohan, D.; Sunandana, C. S., *J. Phys. Chem. B* **2006**, 110, (10), 4569-75.
24. Whittingham, M. S.; Zavalij, P. Y., *Int. J. Inorg. Mater.* **2001**, 3, (8), 1231-1236.
25. Johnson, C. S.; Kim, J.-S.; Kropf, A. J.; Kahaian, A. J.; Vaughey, J. T.; Fransson, L. M. L.; Edstroem, K.; Thackeray, M. M., *Chem. Mater.* **2003**, 15, (12), 2313-2322.
26. Bleaney, B.; Bowers, K. D., *Proc. R. Soc. London, A* **1952**, 214, 451-65.
27. Bodenez, V.; Dupont, L.; Laffont, L.; Armstrong, A. R.; Shaju, K. M.; Bruce, P. G.; Tarascon, J. M., *J. Mater. Chem.* **2007**, 17, (30), 3238-3247.

Chapter 4

1. Sorensen, E. M.; Izumi, H. K.; Vaughey, J. T.; Stern, C. L.; Poeppelmeier, K. R., *J. Am. Chem. Soc.* **2005**, 127, (17), 6347-6352.
2. Albrecht, T. A.; Stern, C. L.; Poeppelmeier, K. R., *Inorg. Chem.* **2007**, 46, (5), 1704-1708.
3. Bertolini, J. C., *J. Emerg. Med.* **1992**, 10, (2), 163-168.
4. Segal, E. B., *Chem. Health Saf.* **2000**, 7, (1), 18-23.
5. Peters, D.; Miethchen, R., *J. Fluorine Chem.* **1996**, 79, (2), 161-165.
6. Harrison, W. T. A.; Nenoff, T. M.; Gier, T. E.; Stucky, G. D., *Inorg. Chem.* **1993**, 32, (11), 2437-2441.
7. Bruker *APEX2 and SAINT*, Bruker Analytical X-ray Instruments, Inc.: Madison, WI, 2006.
8. Sheldrick, G. M. *SHELXTL*, version 5.10; Bruker Analytical X-Ray Instruments, Inc.: Madison, WI, 1997.
9. Kunz, M.; Brown, I. D., *J. Solid State Chem.* **1995**, 115, (2), 395-406.
10. Halasyamani, P.; Heier, K. R.; Willis, M. J.; Stern, C. L.; Poeppelmeier, K. R., *Z. Anorg. Allg. Chem.* **1996**, 622, (3), 479-85.
11. Halasyamani, P.; Willis, M. J.; Heier, K. R.; Stern, C. L.; Poeppelmeier, K. R., *Acta Crystallogr., Sect. C: Cryst. Struct. Commun.* **1996**, C52, (10), 2491-2493.
12. Halasyamani, P.; Willis, M. J.; Stern, C. L.; Poeppelmeier, K. R., *Inorg. Chem.* **1996**, 35, (5), 1367-71.
13. Heier, K. R.; Norquist, A. J.; Wilson, C. G.; Stern, C. L.; Poeppelmeier, K. R., *Inorg. Chem.* **1998**, 37, (1), 76-80.
14. Leimkuehler, M.; Mattes, R., *J. Solid State Chem.* **1986**, 65, (2), 260-264.

15. Welk, M. E.; Norquist, A. J.; Stern, C. L.; Poeppelmeier, K. R., *Inorg. Chem.* **2001**, 40, (22), 5479-5480.
16. Kirsch, J. E.; Izumi, H. K.; Stern, C. L.; Poeppelmeier, K. R., *Inorg. Chem.* **2005**, 44, (13), 4586-4593.
17. Maggard, P. A.; Nault, T. S.; Stern, C. L.; Poeppelmeier, K. R., *J. Solid State Chem.* **2003**, 175, (1), 27-33.

Chapter 5

1. Bateman, L. A.; Fernelius, W. C., *J. Chem. Educ.* **1937**, 14, 315.
2. Jones, J. H.; Thomas, J. S., *J. Chem. Soc., Trans.* **1923**, 123, 3285-94.
3. Lumsden, J. S., *J. Chem. Soc., Trans.* **1902**, 81, 350.
4. Kolb, E. D.; Barns, R. L.; Grenier, J. C.; Laudise, R. A., *Proc. Annu. Freq. Control Symp.* **1979**, 33rd, 88-97.
5. Tremaine, P. R.; Leblanc, J. C., *J. Chem. Thermodyn.* **1980**, 12, (6), 521-38.
6. Bertolini, J. C., *J. Emerg. Med.* **1992**, 10, (2), 163-168.
7. Segal, E. B., *Chem. Health Saf.* **2000**, 7, (1), 18-23.
8. Peters, D.; Miethchen, R., *J. Fluorine Chem.* **1996**, 79, (2), 161-165.
9. Harrison, W. T. A.; Nenoff, T. M.; Gier, T. E.; Stucky, G. D., *Inorg. Chem.* **1993**, 32, (11), 2437-2441.
10. Ellis, A. J., *J. Chem. Soc.* **1963**, (Sept.), 4300-4.
11. Ayotte, P.; Hebert, M.; Marchand, P., *J. Chem. Phys.* **2005**, 123, (18), 184501/1-184501/8.
12. McTigue, P.; O'Donnell, T. A.; Verity, B., *Aust. J. Chem.* **1985**, 38, (12), 1797-807.
13. McCaulay, D. A.; Lien, A. P., *J. Am. Chem. Soc.* **1957**, 79, 2495-7.

14. Klatt, W., *Z. physik. Chem.* **1939**, A185, 306-12.
15. Hatton, J. V.; Saito, Y.; Schneider, W. G., *Can. J. Chem.* **1965**, 43, (1), 47-56.
16. Gillespie, R. J.; Rao, U. R. K., *J. Chem. Soc., Chem. Commun.* **1983**, (8), 422-3.
17. Rao, U. R. K.; Venkateswarlu, K. S.; Wani, B. R.; Sastry, M. D.; Dalvi, A. G. I.; Joshi, B. D., *Mol. Phys.* **1982**, 47, (3), 637-45.
18. Leimkuehler, M.; Mattes, R., *J. Solid State Chem.* **1986**, 65, (2), 260-264.
19. Findlay, A., *The Phase Rule and its Applications*. 9 ed.; Dover Publications, Inc.: 1951.
20. Blasdale, W. C., *J. Ind. Eng. Chem. (Washington, D. C.)* **1918**, 10, 344-7.
21. Wittjen, B.; Precht, H., *Ber. Dtsch. Chem. Ges.* **1881**, 14, 1667-75.
22. Chretien, A., *Caliche* **1926**, 8, 390-408.
23. Prutton, C. F.; Tower, O. F., *J. Am. Chem. Soc.* **1932**, 54, 3040-7.
24. von Zawidzki, J., *Zeit. physikal. Chem.* **1904**, 47, 721-8.
25. Occleshaw, V. J., *J. Chem. Soc., Trans.* **1925**, 127, 2598-602.
26. van Leeuwen, J. D., *Zeit. physikal. Chem.* **1897**, 23, 33-55.
27. Reicher, L. T., *Zeit. physikal. Chem.* **1887**, 1, 221-6.
28. Thomas, H. J.; Jache, A. W., *J. Inorg. Nucl. Chem.* **1960**, 13, 54-7.
29. Buslaev, Y. A.; Bochkareva, V. A., *Zh. Neorg. Khim.* **1967**, 12, (6), 1714-16.
30. Nikolaev, N. S.; Buslaev, Y. A., *Khim. Redkikh Elementov, Akad. Nauk S.S.S.R., Inst. Obshchei i Neorg. Khim.* **1955**, 2, 57-63.
31. Buslaev, Y. A.; Bochkareva, V. A.; Nikolaev, N. S., *Izv. Akad. Nauk SSSR, Ser. Khim.* **1962**, (No. 3), 388-92.

32. Tananaev, I. V.; Nikolaev, N. S.; Buslaev, Y. A., *Zh. Neorg. Khim.* **1956**, 1, 274-81.
33. Nikolaev, N. S.; Buslaev, Y. A., *Zh. Neorg. Khim.* **1959**, 4, 205-12.
34. Buslaev, Y. A.; Nikolaev, N. S., *Zh. Neorg. Khim.* **1959**, 4, 465-71.
35. Nikolaev, N. S., *Khim. Redkikh Elementov, Akad. Nauk S.S.S.R., Inst. Obshchei i Neorg. Khim.* **1954**, 1, 45-51.
36. Shannon, R. D., *Acta Crystallogr. Sect. A* **1976**, A32, (5), 751-67.
37. Yacoubi, A.; Grannec, J.; Tressaud, A.; Linke, D., *Mater. Lett.* **1989**, 7, (11), 385-90.

Chapter 6

1. Brodd, R. J.; Bullock, K. R.; Leising, R. A.; Middaugh, R. L.; Miller, J. R.; Takeuchi, E., *J. Electrochem. Soc.* **2004**, 151, (3), K1-K11.
2. Skarstad, P. M., *J. Power Sources* **2004**, 136, (2), 263-267.
3. Crespi, A. M.; Somdahl, S. K.; Schmidt, C. L.; Skarstad, P. M., *J. Power Sources* **2001**, 96, (1), 33-38.
4. Keister, P.; Mead, R. T.; Ebel, S. J.; Fairchild, W. R., *Proc. Power Sources Symp.* **1984**, 31st, 331-8.
5. Onoda, M.; Kanbe, K., *J. Phys.: Condens. Matter* **2001**, 13, (31), 6675-6685.
6. Leising, R. A.; Thiebolt, W. C., III; Takeuchi, E. S., *Inorg. Chem.* **1994**, 33, (25), 5733-40.
7. Ramasamy, R. P.; Feger, C.; Strange, T.; Popov, B. N., *J. Appl. Electrochem.* **2006**, 36, (4), 487-497.
8. Lee, J.-W.; Popov, B. N., *J. Power Sources* **2006**, 161, (1), 565-572.
9. Leising, R. A.; Takeuchi, E. S., *Chem. Mater.* **1994**, 6, (4), 489-495.
10. Zhang, S.; Li, W.; Li, C.; Chen, J., *J. Phys. Chem. B* **2006**, 110, (49), 24855-24863.

11. Beninati, S.; Fantuzzi, M.; Mastragostino, M.; Soavi, F., *J. Power Sources* **2006**, 157, (1), 483-487.
12. Takeuchi, K. J.; Marschilok, A. C.; Leising, R. A.; Takeuchi, E. S., *Mater. Res. Soc. Symp. Proc.* **2007**, 972, (Solid-State Ionics--2006), 351-356.
13. Leising, R.; Takeuchi, E. S. US Patent 7211349, May 1, 2007.
14. Takeuchi, K. J.; Marschilok, A. C.; Davis, S. M.; Leising, R. A.; Takeuchi, E. S., *Coord. Chem. Rev.* **2001**, 219, 283-310.
15. Sorensen, E. M.; Izumi, H. K.; Vaughey, J. T.; Stern, C. L.; Poeppelmeier, K. R., *J. Am. Chem. Soc.* **2005**, 127, (17), 6347-6352.
16. Sauvage, F.; Bodenez, V.; Vezin, H.; Albrecht, T. A.; Tarascon, J.-M.; Poeppelmeier Kenneth, R., *Inorg. Chem.* **2008**, 47, (19), 8464-8472.
17. Bervas, M.; Mansour, A. N.; Yoon, W. S.; Al-Sharab, J. F.; Badway, F.; Cosandey, F.; Klein, L. C.; Amatucci, G. G., *J. Electrochem. Soc.* **2006**, 153, (4), A799-A808.
18. Badway, F.; Mansour, A. N.; Pereira, N.; Al-Sharab, J. F.; Cosandey, F.; Plitz, I.; Amatucci, G. G., *Chem. Mater.* **2007**, 19, (17), 4129-4141.
19. Palacin, M. R.; Amatucci, G. G.; Anne, M.; Chabre, Y.; Seguin, L.; Strobel, P.; Tarascon, J. M.; Vaughan, G., *J. Power Sources* **1999**, 81-82, 627-631.
20. Choi, W.; Manthiram, A., *J. Electrochem. Soc.* **2007**, 154, (7), A614-A618.
21. Barker, J.; Saidi, M. Y.; Swoyer, J. L., *J. Electrochem. Soc.* **2003**, 150, (10), A1394-A1398.
22. Ellis, B. L.; Makahnouk, W. R. M.; Makimura, Y.; Toghil, K.; Nazar, L. F., *Nat. Mater.* **2007**, 6, (10), 749-753.
23. Bertolini, J. C., *J. Emerg. Med.* **1992**, 10, (2), 163-168.
24. Segal, E. B., *Chem. Health Saf.* **2000**, 7, (1), 18-23.
25. Peters, D.; Miethchen, R., *J. Fluorine Chem.* **1996**, 79, (2), 161-165.

26. Britton, H. T. S.; Robinson, R. A., *J. Chem. Soc., Abstr.* **1930**, 2328-43.
27. Shivahare, G. C., *J. Inorg. Nucl. Chem.* **1966**, 28, (2), 657-8.
28. Souchay, P.; Carpeni, G., *Bull. soc. chim.* **1946**, 160-8.
29. Edgar, G., *Am. Chem. J.* **1911**, 44, 467-72.
30. Albrecht, T. A.; Stern, C. L.; Poeppelmeier, K. R., *Inorg. Chem.* **2007**, 46, (5), 1704-1708.
31. Harrison, W. T. A.; Nenoff, T. M.; Gier, T. E.; Stucky, G. D., *Inorg. Chem.* **1993**, 32, (11), 2437-2441.
32. Izumi, H. K.; Sorensen, E. M.; Vaughey, J. T.; Poeppelmeier, K. R. US Provisional Patent 60/606,475, September 1, 2004.
33. Sheets, W. C.; Mugnier, E.; Barnabe, A.; Marks, T. J.; Poeppelmeier, K. R., *Chem. Mater.* **2006**, 18, (1), 7-20.
34. Thomas, H. J.; Jache, A. W., *J. Inorg. Nucl. Chem.* **1960**, 13, 54-7.
35. Nikolaev, N. S.; Buslaev, Y. A., *Khim. Redkikh Elementov, Akad. Nauk S.S.S.R., Inst. Obshchei i Neorg. Khim.* **1955**, 2, 57-63.
36. Hatton, J. V.; Saito, Y.; Schneider, W. G., *Can. J. Chem.* **1965**, 43, (1), 47-56.
37. Gillespie, R. J.; Rao, U. R. K., *J. Chem. Soc., Chem. Commun.* **1983**, (8), 422-3.
38. Takeuchi, E. S.; Leising, R. A.; Hong, G.; Rubino, R. US Patent Application 2004185346, September 23, 2004.

Chapter 7

1. Dewan, C.; Teeters, D., *J. Power Sources* **2003**, 119-121, 310-315.
2. Sorensen, E. M.; Barry, S. J.; Jung, H.-K.; Rondinelli, J. M.; Vaughey, J. T.; Poeppelmeier Kenneth, R., *Chem. Mater.* **2006**, 18, 482-489.

3. Lytle, J. C.; Yan, H.; Ergang, N.; Smyrl, W. H.; Stein, A., *J. Mater. Chem.* **2004**, 14, (9), 1616-1622.
4. Schroden, R. C.; Al-Daous, M.; Stein, A., *Chem. Mater.* **2001**, 13, 2945-2950.
5. Stein, A.; Schroden, R. C., *Curr. Opin. Solid State Mater. Sci.* **2001**, 5, (6), 553-564.
6. Bertolini, J. C., *J. Emerg. Med.* **1992**, 10, (2), 163-168.
7. Segal, E. B., *Chem. Health Saf.* **2000**, 7, (1), 18-23.
8. Peters, D.; Miethchen, R., *J. Fluorine Chem.* **1996**, 79, (2), 161-165.

Electronic Appendix

Key to SHELX files

number	Pproject number
CIF	Crystallographic information file
FCF	SHELX file - structure factors
HKL	hkl file
INS/RES	SHELX file - ins = res files, atomic coordinates, occupancy
LST	SHELX file - bond distances, Fourier peaks
P4P	SHELX file - set up file
PCF	SHELX file - space group determination
PRP	SHELX file - includes absorption correction
RAW	SHELX file - raw data
IR	Infrared spectrum

Chapter 3

Ag₃VO₄

Number	s87q
CIF	s87q
FCF	s87q
HKL	s87qm
INS/RES	s87q
LST	s87q
P4P	s87qm
PCF	s87q
PRP	s87q
RAW	s87q

Chapter 6

Ag₃VO₂F₄

number	s64n
CIF	s64n1m
FCF	s64n1m
HKL	s64n1m
INS/RES	s64n1m.res
LST	s64n1m
P4P	s64n1m
PCF	s64n1m
PRP	s64n1m
RAW	s64n1m

Vita

Thomas Allen Albrecht

Work Address:

Department of Chemistry
2145 Sheridan Rd.
Evanston, IL 60208-3113

Home Address:

21292 Yarmouth Ln
Huntington Beach, CA 92646

Phone: (224) 628-6406

Email: talbrecht@northwestern.edu

EDUCATION**Northwestern University**

Ph.D. in Inorganic Chemistry, November 2008

Evanston, IL

University of California, Los Angeles

BS in Chemistry with Honors, June 2004

Los Angeles, CA

**RESEARCH
EXPERIENCE****Graduate Student, Northwestern University
Department of Chemistry**

Evanston, IL
2004-2008

Advisor: Professor Kenneth R. Poeppelmeier

- Synthesized new solid-state oxide fluorides using low temperature hydrothermal chemistry
- Patented (pending) a “greener” synthesis of a cathode material for primary lithium batteries
- Interacted with multiple companies to develop their interest in our patented material
- Determined crystal structures of known and discovered compounds
- Electrochemically characterized new high-density silver phases for use as a cathode

**Undergraduate Research, UCLA
Department of Chemistry**

Los Angeles, CA
2003-2004

Advisor: Professor Richard B. Kaner

- Synthesized and optimized yield of graphite encapsulated metal particles by solid state metathesis
- Analyzed results with powder X-ray diffraction, SEM, TEM

PUBLICATIONS

- T.A. Albrecht, F. Sauvage, K.R. Poeppelmeier, US Provisional Patent 60/934,148, June 11, 2007
- T.A. Albrecht, C.L. Stern, K.R. Poeppelmeier, “The $\text{Ag}_2\text{O} - \text{V}_2\text{O}_5 - \text{HF}_{(\text{aq})}$ System and Crystal Structure of $\alpha\text{-Ag}_3\text{VO}_4$ ”, *Inorg. Chem.*, **2007**, 46, 1704-1708
- M.I. Bertoni, N.J. Kinder, T.O. Mason, T.A. Albrecht, E.M. Sorensen, K.R. Poeppelmeier, “Electrical and Optical Characterization of $\text{Ag}_2\text{V}_4\text{O}_{11}$ and $\text{Ag}_4\text{V}_2\text{O}_6\text{F}_2$ ”, *J. Electroceram.*, **2007**, 18, 189-195
- F. Sauvage, V. Bodenez, H. Vezin, T.A. Albrecht, J.-M. Tarascon, K.R. Poeppelmeier, “Insights on the Lithium Insertion Mechanism into the High Silver Density Phase $\text{Ag}_4\text{V}_2\text{O}_6\text{F}_2$ (SVOF)”, *Inorg. Chem.*, **2008**, 47, 8464-8472
- T.A. Albrecht, F. Sauvage, V. Bodenez, J.-M. Tarascon, K.R. Poeppelmeier, “New Approach for the Synthesis of Silver Oxide Fluoride Cathode Materials for Implantable Cardioverter Defibrillators”, in preparation

PRESENTATIONS

- “Unique Cathodic High-Density Silver Materials for High Specific Energy, Long Life Power Sources” (poster), International Workshop on Synthesis of Functional Oxide Materials, August 19–23, 2007, UCSB, Santa Barbara, CA
- “Unique Cathodic High-Density Silver Materials for High Specific Energy, Long Life Power Sources” (poster), North American Solid State Chemistry Conference, May 17–19, 2007, Texas A&M University, College Station, TX
- “Electrochemical Characterization of $\text{Ag}_4\text{V}_2\text{O}_6\text{F}_2$ in Primary Lithium Batteries” (oral), 211th Electrochemical Society Meeting Medical Battery Symposium, May 9, 2007, Chicago, IL
- “GEMs (Graphite Encapsulated Metal particles)” (poster), 227th American Chemical Society National Meeting, March 28–April 1, 2004, Anaheim, CA